

# Wind Turbine Wakes in Active Yaw Control: Numerical and Theoretical Studies

Présentée le 14 septembre 2023

Faculté de l'environnement naturel, architectural et construit  
Laboratoire d'ingénierie éolienne et d'énergie renouvelable  
Programme doctoral en mécanique

pour l'obtention du grade de Docteur ès Sciences

par

**Mou LIN**

Acceptée sur proposition du jury

Prof. F. Gallaire, président du jury  
Prof. F. Porté Agel, directeur de thèse  
Prof. R. J. A. M. Stevens, rapporteur  
Prof. S. J. Andersen, rapporteur  
Prof. K. Mulleners, rapporteuse



To my parents.





# Acknowledgements

First of all, I would like to express my gratitude to my supervisor, Prof. Fernando Porté-Agel, for his guidance, patience, and support throughout my PhD journey. His insightful comments and feedbacks helped me to develop my research skills and expand my knowledge in the field. Without his expertise and dedication, this thesis would not have been possible. I also would like to thank the committee members of my defence, Prof. François Gallaire, Prof. Karen Mulleners, Prof. Richard J. A. M. Stevens, and Prof. Søren J. Andersen, for their suggestions and comments on this thesis.

I would like to thank my colleagues and friends at WiRE, Nicolas K. Bossi, Tristan Revaz, Dara Vahidi, Arslan S. Dar, Marwa Souaiby, Peter A. Brugger, Guiyue Duan, Majid Bastankhah, Sina Shamsoddin, Fernando C. Ferrero, Vincent Rolin, Jiannong Fang, Haohua Zong, Farshid Kardan. I cherish every minute I spent with you: the casual talks in the lab's kitchen, the inspiring discussions in front of the screen and the whiteboard, the happy hours in the Satellite, and the refreshing time in the Alps. All these moments will forever be my dearest memory. Without them, this PhD journey would be colourless.

I would like to especially thank Mrs Nicole Nicoud and Mr Pierre Nicoud, who is unfortunately no longer with us. They charmingly welcomed me to live in their house five years ago and offered me countless help throughout the years I stayed with them. I will forever be grateful for their kindness and generosity.

Lastly, I would like to express my deepest gratitude to the people I love the most: my parents, Hongwen Lin and Lihua Kang, and my girlfriend, Jianyu Zhao. Their unweaving love is the greatest support to me to go through the ups and downs of this journey. This PhD thesis is dedicated to you all with love.

*Lausanne, June 2023*

Mou Lin



# Abstract

Wind turbines operating in wind farms often suffer from the interference of the wakes from upwind turbines, causing significant power losses and fatigue. To address this issue, wind energy researchers have proposed active yaw control (AYC) to redirect the wakes of upwind turbines away from downwind turbines. However, since the wake behaviour of a yawed turbine is significantly different from that of a non-yawed turbine, theoretical and simulation models that yield satisfactory results for non-yawed turbine wakes usually fail to capture the unique features of yawed turbine wakes. In this thesis, we systematically explore the best practice of simulating the wakes of the turbines subjected to AYC using large-eddy simulation (LES) and evaluate the effects of AYC on the power production and fatigue of wind turbines.

In the first study, we validate the blade-element actuator disk model (ADM-BE) for LES of the wake of a yawed wind turbine. LES results using the ADM-BE are compared with wind-tunnel measurements and analytical model predictions of the wake of a stand-alone miniature wind turbine with different yaw angles. We find that the results using the ADM-BE in LES are in good agreement with both wind-tunnel measurements and analytical model predictions in terms of the mean velocity and turbulence intensity in the wake. We also find significant improvements in the power prediction of the ADM-BE over the standard actuator disk model (ADM-std).

In the second study, we compare the LES results of the flow through a three-turbine array in the non-yawed/yawed and full/partial-wake conditions with wind-tunnel measurements. The turbine forces are parametrised by three models: the ADM-std, the ADM-BE, and the actuator line model (ALM). The turbine power outputs and wake flow statistics obtained from the simulations are compared with experimental results. We find that the results of LES using the ADM-BE and ALM are in good agreement with wind-tunnel measurements. In contrast, the results of LES with the ADM-std show discrepancies with the measurements in the yawed and partial-wake conditions. These discrepancies are caused by the uniform force assumption of the ADM-std, which fails to reproduce the inherently inhomogeneous distribution of the turbine forces. We also find that LES using the ADM-BE yields better power predictions than the ADM-std and the ALM in the cases considered in this study.

---

In the third study, we investigate the power production and blade fatigue of a three-turbine array subjected to AYC in the full/partial-wake configurations. A two-way coupled framework of LES and aeroelastic simulation is applied to simulate the flow through the turbines and the structural responses of the blades. In the full-wake configuration, we find that the local power-optimal AYC strategy with positive yaw angles endures less flapwise blade fatigue and more edgewise blade fatigue than the global optimal strategy with negative yaw angles. In the partial-wake configuration, in certain inflow wind directions, applying positive AYC achieves higher optimal power gains than that in the full-wake scenario while reducing blade fatigue from the non-yawed benchmark. Using the blade-element momentum (BEM) theory, we show that the aforementioned differences in flapwise blade fatigue are caused by the differences in the azimuthal distributions of the local relative velocity on blade sections, resulting from the combine effects of vertical wind shear and blade rotation. Furthermore, the difference in the blade force between the positively and negatively yawed front-row turbine induces different wake velocity and turbulence distributions, which causes different fatigue loads on the downwind turbine exposed to the wake.

Finally, in the fourth study, we use LES to investigate the wake-meandering of a wind turbine array under dynamic yaw control (DYC) and the effects on turbine power and fatigue. The wind turbine array consists of eight NREL 5 MW reference turbines. The first turbine in the array is subjected to sinusoidal yaw control with different yaw frequencies. Based on spectral and dynamic mode decomposition (DMD) analyses of the flow fields, we find that the wake meandering of the turbine array is significantly amplified when the turbine yaw frequency coincides with the natural wake meandering frequency of the turbine array in the static zero-yaw condition. The resonance of wake meandering accelerates wake recovery and helps the turbine array achieve optimal power production. We also find that the fatigue of the turbine array increases overall with the yaw frequency of the first turbine, highlighting the necessity of jointly considering power production and fatigue when applying DYC.

Key words: Large-eddy simulation; Active yaw control; Wind turbine wakes; Power production; Fatigue loads; Dynamic yaw control.

# Résumé

Les éoliennes dans les parcs éoliens souffrent souvent des interférences des éoliennes amont, entraînant des pertes de puissance et de la fatigue significatives. Pour remédier à ce problème, les chercheurs en énergie éolienne ont proposé un contrôle actif de l'angle de lacet (CAL) pour dévier les sillages des éoliennes amont loin des éoliennes aval. Cependant, étant donné que la physique du sillage d'une éolienne en lacet est significativement différente de une éolienne sans lacet, les modèles de simulation qui produisent des résultats satisfaisants pour les éoliennes sans lacet échouent parfois à capturer les caractéristiques uniques des sillages d'éoliennes en lacet. Dans cette thèse, nous explorons systématiquement les meilleures pratiques de simulation des sillages d'éoliennes soumises au CAL utilisant une simulation des grandes échelles (SGE) et évaluons les effets du CAL sur la production d'énergie et la fatigue des éoliennes.

Dans la première étude, nous validons le modèle de disque actionneur basé sur l'élément de pale (ADM-BE) pour la SGE du sillage d'une éolienne en lacet. Les résultats SGE obtenus avec l'ADM-BE ont été comparés aux mesures en soufflerie et aux prévisions des modèles analytiques du sillage d'une éolienne miniature avec différents angles de lacet. Nous constatons que les résultats obtenus avec l'ADM-BE en SGE sont en bon accord avec les mesures en soufflerie et les prévisions des modèles analytiques de la vitesse moyenne et de l'intensité de turbulence dans le sillage. Nous avons également constaté une amélioration significative de la prédiction de puissance de l'ADM-BE par rapport à le disque actionneur standard (ADM-std).

Dans la deuxième étude, nous comparons la SGE de l'écoulement à travers des trois éoliennes dans les conditions de sillage complet/partiel et de lacet/non-lacet avec des mesures en soufflerie. Les forces des éoliennes sont paramétrées par trois modèles : l'ADM-std, l'ADM-BE et le modèle de ligne actionneur (ALM). La puissance des éoliennes et les profils des statistiques d'écoulement dans le sillage obtenus à partir des simulations sont également comparés aux résultats expérimentaux. Nous constatons que les résultats de simulation de SGE utilisant l'ADM-BE et l'ALM sont en bon accord avec les mesures en soufflerie. En revanche, les résultats de LES avec l'ADM-std montrent des écarts avec les mesures dans les conditions de lacet et/ou de sillage partiel. Ces écarts sont causés par l'hypothèse de force uniforme de l'ADM-std, qui ne parvient pas à reproduire la distribution intrinsèquement

---

non-homogène des forces. Nous constatons également que la simulation utilisant l'ADM-BE fournit de meilleures prédictions de puissance que l'ADM-std et l'ALM dans les cas étudiés.

Dans la troisième étude, nous étudions la production d'énergie et la fatigue des trois éoliennes soumises à des angles de lacet actif dans des configurations de sillage complet/partiel. Un cadre de la simulation couplée de la SGE et la simulation aéroélastique est utilisé pour simuler l'écoulement à travers les éoliennes et les réponses structurales des pales. Dans la configuration de sillage complet, nous constatons que la stratégie CAL locale optimale pour la puissance utilisant des angles de lacet positifs subit moins de fatigue transversale des pales et plus de fatigue latérale des pales que la stratégie globale optimale pour la puissance avec des angles de lacet négatifs. Dans la configuration de sillage partiel avec certaines directions de vent entrant, l'application d'un CAL positif permet d'obtenir des gains de puissance optimaux plus élevés que dans le scénario de sillage complet tout en réduisant la fatigue des pales par rapport à la référence sans lacet. Utilisant la théorie de l'élément de pale (BEM), nous montrons que les différences de fatigue de flexion de pale susmentionnées sont causées par les différences de distributions azimutales de la vitesse relative locale sur les sections de pale, résultant du cisaillement vertical du vent et de la rotation de la pale. De plus, la différence de force de pale entre l'éolienne de première rangée à lacet positif et négatif induit des distributions de vitesse et de turbulence de sillage différentes, ce qui entraîne des charges de fatigue différentes sur l'éolienne exposée au sillage.

Enfin, dans la quatrième étude, nous utilisons la SGE pour étudier le phénomène des méandres des sillages dans un parc éolien sous un contrôle dynamique de lacet (CDL) et ses effets sur la puissance et la fatigue des éoliennes. Le parc éolien se compose de huit éoliennes de référence NREL de 5 MW. La première éolienne du parc est soumise à un contrôle de lacet sinusoïdal avec différentes fréquences de lacet. En se basant sur l'analyse spectrale et de décomposition de mode dynamique (DMD) des champs de flux, nous constatons que le méandrage de sillage dans le parc éolien est significativement amplifié lorsque la fréquence de lacet de l'éolienne coïncide avec la fréquence de méandrage de sillage naturelle du parc dans des conditions sans lacet. La résonance du méandrage de sillage accélère la récupération du sillage et permet au parc d'atteindre une production optimale de puissance. Nous constatons également que la fatigue globale des éoliennes augmente avec la fréquence de lacet de la première éolienne, soulignant la nécessité de prendre en compte conjointement la production d'énergie et la fatigue lors de l'application d'un contrôle dynamique de lacet.

Mots clefs : Simulation à grandes échelles; Contrôle de lacet actif; Le sillage d'une éolienne; Production d'énergie; Charges de fatigue; Contrôle dynamique de lacet.

# Contents

<b>Acknowledgements</b>	<b>i</b>
<b>Abstract (English/Français)</b>	<b>iii</b>
<b>List of figures</b>	<b>ix</b>
<b>List of tables</b>	<b>xv</b>
<b>1 Introduction</b>	<b>1</b>
<b>2 LES of a yawed stand-alone wind turbine</b>	<b>5</b>
2.1 Introduction . . . . .	6
2.2 Large-eddy simulation framework . . . . .	8
2.2.1 Governing equations . . . . .	8
2.2.2 Wind turbine parametrisation . . . . .	9
2.2.3 Numerical setup . . . . .	10
2.3 Results . . . . .	13
2.3.1 Inflow conditions . . . . .	13
2.3.2 Velocity deficit and turbulence intensity contours . . . . .	13
2.3.3 Spanwise Velocity Deficit and Turbulence Intensity Profiles . . . . .	15
2.3.4 Mechanical power predictions . . . . .	19
2.4 Summary . . . . .	21
<b>3 LES of a wind-turbine array subjected to active yaw control</b>	<b>23</b>
3.1 Introduction . . . . .	24
3.2 Methodology . . . . .	26
3.2.1 Governing equations . . . . .	26
3.2.2 Wind turbine parametrisation . . . . .	27
3.2.3 Case configuration . . . . .	29
3.2.4 Numerical configuration . . . . .	29
3.3 Results . . . . .	31
3.3.1 Mean velocity . . . . .	31
3.3.2 Turbulence statistics . . . . .	34
3.3.3 Power prediction . . . . .	42
3.4 Summary . . . . .	50

## Contents

---

3.5	Appendix . . . . .	51
<b>4</b>	<b>Power and fatigue of a wind-turbine array under active yaw control</b>	<b>53</b>
4.1	Introduction . . . . .	54
4.2	Methodology . . . . .	55
4.2.1	Governing equations . . . . .	55
4.2.2	Simulation setup . . . . .	56
4.2.3	Fatigue evaluation . . . . .	57
4.3	Results . . . . .	59
4.3.1	Velocity deficits . . . . .	59
4.3.2	Power production . . . . .	62
4.3.3	Blade fatigue loading . . . . .	62
4.4	Theoretical analysis on flapwise blade fatigue . . . . .	65
4.5	Summary . . . . .	69
<b>5</b>	<b>Wake meandering of a wind-turbine array under dynamic yaw control</b>	<b>73</b>
5.1	Introduction . . . . .	74
5.2	Methodology . . . . .	75
5.2.1	Governing equations and simulation framework . . . . .	75
5.2.2	Simulation case setup . . . . .	76
5.3	Simulation results . . . . .	77
5.3.1	Wake meandering in the turbine array . . . . .	77
5.3.2	Space-time dynamics of the maximum wake deficit trajectory . . . . .	78
5.3.3	Power spectrum analysis of the velocity signals . . . . .	78
5.3.4	Dynamic mode decomposition (DMD) analysis . . . . .	80
5.3.5	Streamwise profiles of the wake flow statistics . . . . .	83
5.3.6	Impacts on wind turbine power and fatigue . . . . .	86
5.4	Summary and conclusions . . . . .	89
5.5	Appendix . . . . .	92
<b>6</b>	<b>Overall summary and future research perspectives</b>	<b>93</b>
6.1	Overall summary . . . . .	93
6.2	Future perspectives . . . . .	94
	<b>Bibliography</b>	<b>106</b>
	<b>Curriculum Vitae</b>	<b>107</b>



# List of Figures

2.1	Reference-frame transformation from mesh-aligned $x$ - $y$ - $z$ to rotor-normal $x'$ - $y'$ - $z'$ for a wind turbine of a yaw angle $\gamma$ . The positive yaw angle is defined as the clockwise direction viewing from the top. . . . .	11
2.2	Force smearing from blade elements to neighbouring computational cells. . . .	11
2.3	Schematic plots of (a) the simulation domain; (b) the WiRE-01 miniature wind turbine. . . . .	12
2.4	(a) Vertical profiles of the normalised mean streamwise velocity component $\bar{u}/\bar{u}_h$ ; (b) Vertical profiles of the streamwise turbulence intensity $I_u$ ; (c) Log-law velocity profiles plotted against the vertical profiles of the mean streamwise velocity component normalised by the friction velocity $u_*$ . . . . .	14
2.5	Contours of the normalised streamwise mean velocity deficit $\Delta\bar{u}/\bar{u}_h$ in the $x$ - $y$ cross-section plane at the hub height obtained from (a) the wind-tunnel experiments and (b) the LES using the ADM-BE. White circles represent the wake-centre trajectories for the experiment results and white solid lines for the simulation results. . . . .	15
2.6	Contours of the normalised streamwise velocity deficit $\Delta\bar{u}/\bar{u}_h$ for different yaw angles $\gamma$ , overlapped with vector fields of the inplane velocity in the $y$ - $z$ cross-section plane at $x/d = 6$ : (a) wind-tunnel measurements; (b) LES using the ADM-BE; (c) LES using the ADM-std. White circles outline the edges of the non-yawed turbine rotor. . . . .	16
2.7	Contours of the added streamwise turbulence intensity $I_{u,add}$ for different yaw angles $\gamma$ , overlapped with vector fields of the inplane velocity in the vertical $y$ - $z$ cross-section plane at $x/d = 6$ : (a) wind-tunnel measurements; (b) LES using the ADM-BE; (c) LES using the ADM-std. White circles outline the edges of the non-yawed turbine rotor. . . . .	17
2.8	Spanwise profiles of the normalised mean streamwise velocity deficit $\Delta\bar{u}/\bar{u}_h$ : (a) $\gamma = 10^\circ$ ; (b) $\gamma = 20^\circ$ ; (c) $\gamma = 30^\circ$ . . . . .	18
2.9	Comparisons of LES results and analytical wake model predictions with respect to wind-tunnel measurements: (a) maximum velocity deficit; (b) wake-centre location. . . . .	19
2.10	Spanwise profiles of the streamwise turbulence intensity $I_u$ : (a) $\gamma = 10^\circ$ ; (b) $\gamma = 20^\circ$ ; (c) $\gamma = 30^\circ$ . . . . .	20

## List of Figures

---

2.11	Spanwise profiles of the normalised mean streamwise velocity deficit $\Delta\bar{u}/\bar{u}_h$ of the wake behind a wind turbine with a yaw angle $\gamma = 20^\circ$ , obtained from the LES using the ADM-BE using different mesh resolutions. . . . .	20
2.12	(a) Conversion of power in the miniature wind turbine model: Mechanical power $P_{Mech}$ , Shaft friction loss $P_f$ , Electrical loss $P_j$ and Electrical power $P_e$ . (b) Mechanical power coefficient $C_p$ for yaw angles $0^\circ$ - $30^\circ$ obtained from the LES results and the wind-tunnel experiments. . . . .	22
3.1	Schematic representation of the three wind turbine parametrisations used in WiRE-LES: (a) the ADM-std; (b) the ADM-BE; (c) the ALM. To illustrate the differences in the distribution of the forces computed using the three models, the normalised contours of the instantaneous force distribution (normalised by the respective maximum value) induced by each model are plotted. . . . .	28
3.2	Schematic plots of the simulation domain (not to scale): (a) top view; (b) side view.	30
3.3	Vertical profiles of the inflow streamwise mean velocity $\bar{u}_{in}$ (m/s) (a) and the streamwise turbulence intensity $I_u$ (b). Blue solid lines represent the LES results, and red dots represent the corresponding measurement data at the hub height.	31
3.4	Contours of the normalised streamwise mean velocity $\bar{u}/\bar{u}_{hub}$ in the $x$ - $y$ plane at hub height obtained from the wind-tunnel experiments and LES in Cases 1. (a) Experiment; (b) ADM-std; (c) ADM-BE; (d) ALM. . . . .	32
3.5	Contours of the normalised streamwise mean velocity $\bar{u}/\bar{u}_{hub}$ in the $x$ - $y$ plane at hub height obtained from the wind-tunnel experiments and LES in Cases 2. (a) Experiment; (b) ADM-std; (c) ADM-BE; (d) ALM. . . . .	33
3.6	Spanwise profiles of the normalised streamwise mean velocity $\bar{u}/\bar{u}_{hub}$ in the $x$ - $y$ plane at hub height obtained from the wind-tunnel experiments and LES in Case 1. (a) WT 1; (b) WT 2; (c) WT 3. . . . .	35
3.7	Spanwise profiles of the normalised streamwise mean velocity $\bar{u}/\bar{u}_{hub}$ in the $x$ - $y$ plane at hub height obtained from the wind-tunnel experiments and LES in Case 2. (a) WT 1; (b) WT 2; (c) WT 3. . . . .	36
3.8	Contours of the normalised streamwise mean velocity $\bar{u}/\bar{u}_{hub}$ in the $x$ - $y$ plane at hub height obtained from the wind-tunnel experiments and LES in Cases 3: (a) Experiment; (b) ADM-std; (c) ADM-BE; (d) ALM. . . . .	37
3.9	Contours of the normalised streamwise mean velocity $\bar{u}/\bar{u}_{hub}$ in the $x$ - $y$ plane at hub height obtained from the wind-tunnel experiments and LES in Cases 4: (a) Experiment; (b) ADM-std; (c) ADM-BE; (d) ALM. . . . .	38
3.10	Spanwise profiles of the normalised streamwise mean velocity $\bar{u}/\bar{u}_{hub}$ in the $x$ - $y$ plane at hub height obtained from the wind-tunnel experiments and LES in Case 3. (a) WT 1; (b) WT 2; (c) WT 3. . . . .	39
3.11	Spanwise profiles of the normalised streamwise mean velocity $\bar{u}/\bar{u}_{hub}$ in the $x$ - $y$ plane at hub height obtained from the wind-tunnel experiments and LES in Case 4. (a) WT 1; (b) WT 2; (c) WT 3. . . . .	40

3.12 Trajectories of maximum velocity deficit location obtained from the wind-tunnel experiments, LES using the ADM-std, ADM-BE and ALM. (a) Case 1: $\gamma = (0^\circ, 0^\circ, 0^\circ)$ , zero offset; (b) Case 2: $\gamma = (-25^\circ, -15^\circ, 0^\circ)$ , zero offset; (c) Case 3: $\gamma = (0^\circ, 0^\circ, 0^\circ)$ , $d/3$ offset; (d) Case 4: $\gamma = (-20^\circ, -20^\circ, 0^\circ)$ , $d/3$ offset. . . . .	41
3.13 Back-view contours of the time-averaged normal force per unit area on the rotor disk of WT 3 in Case 2. The turbine forces are parametrised by (a) the ADM-std; (b) the ADM-BE; (c) the ALM. . . . .	42
3.14 Contours of the turbulence intensity $I_u$ in the $x$ - $y$ plane at hub height obtained from the wind-tunnel experiments and LES in Case 1: (a) Experiment; (b) ADM-std; (c) ADM-BE; (d) ALM. . . . .	43
3.15 Contours of the turbulence intensity $I_u$ in the $x$ - $y$ plane at hub height obtained from the wind-tunnel experiments and LES in Case 2: (a) Experiment; (b) ADM-std; (c) ADM-BE; (d) ALM. . . . .	44
3.16 Spanwise profiles of the turbulence intensity $I_u$ in the $x$ - $y$ plane at hub height obtained from the wind-tunnel experiments and LES in Case 1. (a) WT 1; (b) WT 2; (c) WT 3. . . . .	45
3.17 Spanwise profiles of the turbulence intensity $I_u$ in the $x$ - $y$ plane at hub height obtained from the wind-tunnel experiments and LES in Case 2. (a) WT 1; (b) WT 2; (c) WT 3. . . . .	46
3.18 Contours of the normalised turbulence flux $\overline{u'v'}/\overline{u}_{hub}$ in the $x$ - $y$ plane at hub height obtained from LES using the (a) ADM-std, (b) ADM-BE and (c) ALM in the yawed Case 2 ( $\gamma = (-25^\circ, -15^\circ, 0^\circ)$ ). . . . .	47
3.19 (a) Power coefficients of the first turbine in the turbine array in zero yaw. The black solid line marks the measured power coefficient. (b) Relative errors of the power coefficient compared to the power measurement. The black dashed line marks the uncertainty bound of the power measurement. . . . .	48
3.20 Normalised power outputs in (a) Case 1: $\gamma = (0^\circ, 0^\circ, 0^\circ)$ , zero offset; (b) Case 2: $\gamma = (-25^\circ, -15^\circ, 0^\circ)$ , zero offset; (c) Case 3: $\gamma = (0^\circ, 0^\circ, 0^\circ)$ , $d/3$ offset; (d) Case 4: $\gamma = (-20^\circ, -20^\circ, 0^\circ)$ , $d/3$ offset. The power outputs are normalised by the measured power of the zero-yawed first turbine of the turbine array. . . . .	49
3.21 Normalised power errors in (a) Case 1: $\gamma = (0^\circ, 0^\circ, 0^\circ)$ , zero offset; (b) Case 2: $\gamma = (-25^\circ, -15^\circ, 0^\circ)$ , zero offset; (c) Case 3: $\gamma = (0^\circ, 0^\circ, 0^\circ)$ , $d/3$ offset; (d) Case 4: $\gamma = (-20^\circ, -20^\circ, 0^\circ)$ , $d/3$ offset. The power outputs are normalised by the measured power of the zero-yawed first turbine of the turbine array. . . . .	49
3.22 Normalised total power errors of the three-turbine array. The errors are normalised by the total measured power of the wind turbine array in each case. Case 1: $\gamma = (0^\circ, 0^\circ, 0^\circ)$ , zero offset; Case 2: $\gamma = (-25^\circ, -15^\circ, 0^\circ)$ , zero offset; Case 3: $\gamma = (0^\circ, 0^\circ, 0^\circ)$ , $d/3$ offset; Case 4: $\gamma = (-20^\circ, -20^\circ, 0^\circ)$ , $d/3$ offset. . . . .	50

3.23	Profiles of the normalised streamwise mean velocity (left column) and turbulence intensity (right column) in the $x - y$ plane at the hub height, obtained from the wind-tunnel experiments and the LES at different grid resolutions. (a) and (b): the ADM-std; (c) and (d): the ADM-BE; (e) and (f): the ALM. The yaw angle of the wind turbine is $-25^\circ$ . . . . .	51
4.1	The ground-fixed coordinate system $x - y - z$ for solving the filtered Navier-Stokes equations and the blade-following coordinate system $x'_n - y'_n - z'_n$ for solving the Euler-Bernoulli beam equations for the $n$ th blade: (a) top view; (b) front view. $\psi$ is the phase angle of the blade. $\gamma$ is the yaw angle of the turbine. The positive directions of $\psi$ and $\gamma$ follow the right-hand rule. . . . .	57
4.2	The coupling procedure between the flow solver and the structural solver in the EALM. The arrows in the flowchart represent the variable passing between different modules of the solver. . . . .	58
4.3	Schematic plots (not to scale) of (a) the simulation domain; (b) NREL 5MW reference wind turbine. . . . .	58
4.4	Top-view $x - y$ cross-section contours of normalised streamwise mean velocity deficits $\Delta\bar{u}/\bar{u}_{hub}$ at the hub height. Full-wake configuration ( $\alpha = 0^\circ$ ): (a) $\gamma = (0^\circ, 0^\circ, 0^\circ)$ ; (b) $\gamma = (25^\circ, 20^\circ, 0^\circ)$ ; (c) $\gamma = (-25^\circ, -20^\circ, 0^\circ)$ . Partial-wake configuration ( $\alpha = 3^\circ$ ): (d) $\gamma = (0^\circ, 0^\circ, 0^\circ)$ ; (e) $\gamma = (25^\circ, 20^\circ, 0^\circ)$ ; (f) $\gamma = (-25^\circ, -20^\circ, 0^\circ)$ . . . . .	60
4.5	Front-view $y - z$ cross-section contours of normalised streamwise velocity deficits $\Delta\bar{u}/\bar{u}_{hub}$ at the location $6d$ downwind of WT 1, overlapped with vector fields of in-plane velocity components: (a) $\gamma_1 = 0^\circ$ ; (b) $\gamma_1 = 25^\circ$ ; (c) $\gamma_1 = -25^\circ$ . . . . .	61
4.6	Normalised power outputs of different AYC configurations, normalised by the power of WT 1 in zero yaw (a) in the full-wake configuration $\alpha = 0^\circ$ (b) in partial-wake configuration $\alpha = 3^\circ$ . . . . .	63
4.7	Normalised power gain contours in the AYC decision space $\Gamma$ for different inflow angles. Black dots show the AYC configurations with the largest power gains. . . . .	64
4.8	Time series segments of blade-root bending moments of WT 1: (a) flapwise bending moment; (b) edgewise bending moment. Empty cycles show the load reversal points extracted by the rainflow counting algorithm. . . . .	65
4.9	Normalised DELs of blade-root bending moments in different AYC configurations and inflow angles, normalised by the DELs of WT 1 in the zero-yaw condition: (a)-(b) flapwise bending moment; (c)-(d) edgewise bending moment. . . . .	66
4.10	Normalised DEL variation contours in the AYC decision space $\Gamma$ for different inflow angles for (a)-(e) flapwise bending moment; (f)-(j) edgewise bending moment. Black dots show the power-optimal AYC configurations and their corresponding DEL variations. . . . .	67
4.11	Schematic plot of the velocity and force triangles on a rotating wind turbine blade based on the BEM theory (replotted from Burton et al. (2011)). . . . .	68
4.12	Freestream inflow velocity to the turbine blade section $r = 0.7R$ : (a) at different vertical heights; (b) at different blade phase angles. . . . .	70

4.13	Azimuthal variations of $V_n V_t$ at $r = 0.7R$ with respect to the blade phase angle $\psi$ predicted by the BEM theory in (a) a uniform inflow $u(z) = 11$ m/s; (b) a vertically sheared inflow $u(z) = \frac{u_*}{\kappa} \log(z/z_0)$ , in which $u_* = 0.45$ m/s, $\kappa = 0.4$ , and $z_0 = 0.005$ m. . . . .	70
4.14	Front-view $y - z$ cross-section contours of normalised streamwise mean velocity and turbulence intensity $I_u$ at the location $6d$ downwind of WT 1: (a) $\bar{u}/\bar{u}_{hub}$ , $\gamma_1 = -25^\circ$ ; (b) $\bar{u}/\bar{u}_{hub}$ , $\gamma_1 = 25^\circ$ ; (c) $I_u$ , $\gamma_1 = -25^\circ$ ; (d) $I_u$ , $\gamma_1 = 25^\circ$ . Black and red circles represent the trajectories of the blade sections $r = 1.0R$ and $r = 0.7R$ of the rotating blade, respectively. . . . .	71
5.1	Top-view of the simulation domain and the wind turbine array (not to scale). . . . .	76
5.2	Schematic plot of the mechanisms of wake meandering behind a wind turbine. The blue line represents the trajectory of the maximum velocity deficit in the wake. . . . .	78
5.3	Instantaneous (a) and time-averaged (b) contours of the streamwise velocity at the hub height $z = 90$ m in the static zero-yaw baseline case. The black dotted lines represent trajectories of the maximum $u$ deficit in the wakes. The black dashed line represents the centre-line of the turbine array. . . . .	79
5.4	Space-time plots of the lateral displacement of maximum velocity deficit locations normalised by the turbine diameter $\Delta_{wake}/d$ : (a) Zero-yaw baseline case $\gamma_{max} = 0^\circ$ , $f_{yaw} = 0$ Hz; (b) DYC case $\gamma_{max} = 10^\circ$ , $f_{yaw} = 0.01$ Hz. . . . .	79
5.5	Normalised power spectrum density (PSD) plots of lateral velocity component $v$ sampled at $6D$ downstream of each turbine. The red dashed lines mark the yaw frequency in different cases: (a1) - (a8) Static zero-yaw baseline $f_{yaw} = 0$ Hz; (b1) - (b8) Slow yaw $f_{yaw} = 0.004$ Hz; (c1) - (c8) moderate yaw $f_{yaw} = 0.01$ Hz; (d1) - (d8) fast yaw $f_{yaw} = 0.016$ Hz. . . . .	81
5.6	First 15 DMD components (redundant conjugated components removed) of the lateral velocity $v$ in the static zero-yaw baseline case: (a) spatial modes; (b) associated time dynamics. . . . .	82
5.7	Mode amplitude coefficients vs mode frequencies extracted from the DMD of the hub-height lateral velocity $v$ : (a) static zero-yaw baseline; (b) $f_{yaw} = 0.004$ Hz; (c) $f_{yaw} = 0.01$ Hz; (d) $f_{yaw} = 0.016$ Hz. Red dashed lines represent the yaw frequency. . . . .	84
5.8	Contours of the selected DMD spatial modes of the hub-height lateral velocity $v$ in difference cases: (a) static zero-yaw baseline $f_{yaw} = 0$ Hz (b) slow yaw $f_{yaw} = 0.004$ Hz (c) moderate yaw $f_{yaw} = 0.01$ Hz (d) fast yaw $f_{yaw} = 0.016$ Hz. The associated mode frequency in (a) is $0.01$ Hz. In (b) - (d), the associated frequencies are the same as the yaw frequencies. . . . .	84
5.9	Profiles of the flow statistics averaged within the projections of turbine rotors at different streamwise locations: (a) normalised streamwise mean velocity; (b) streamwise turbulence intensity. . . . .	85

## List of Figures

---

5.10	Normalised power outputs of each turbine in the array: (a) normalised by the power of the first turbine in the baseline case $P_{1,baseline}$ ; (b) normalised by the power of each turbine in the baseline case $P_{i,baseline}$ , respectively. . . . .	87
5.11	Total power outputs of the wind turbine array vs WT 1 yaw frequency $f_{yaw}$ . The power outputs are normalised by the total power of the static zero-yaw baseline case. . . . .	88
5.12	Fatigue evaluation using the time series of the flapwise blade-root bending moment of WT 1 in the baseline case: (a) identify the load reversal points; (b) use the rainflow counting algorithm to extract the load cycles and assemble the rainflow matrix; (c) obtain the cumulative distribution of the ranges of load cycles and calculate the DEL using the Miner's rule. . . . .	88
5.13	Normalised DELs of the blade-root flapwise bending moment for each turbine in the array: (a) normalised by the DEL of the first turbine in the baseline case; (b) normalised by the DEL of each turbine in the baseline case. . . . .	90
5.14	Normalised DELs of the nacelle yaw moment for each turbine in the array: (a) normalised by the DEL of the first turbine in the baseline case; (b) normalised by the DEL of each turbine in the baseline case. . . . .	91

## List of Tables

2.1	Main characteristics of the incoming boundary-layer flow. . . . .	12
2.2	Mesh resolutions of different simulation cases. $N_{d,y}$ and $N_{d,z}$ represent the number of cells covering the turbine rotor in the $y$ and $z$ directions, respectively, in the non-yawed case. . . . .	13
3.1	Case configurations of the wind tunnel experiments, with the specifications of the lateral offset $S_y$ , the yaw angles $\gamma = (\gamma_1, \gamma_2, \gamma_3)$ and the rotational speeds $\omega = (\omega_1, \omega_2, \omega_3)$ . . . . .	29
4.1	Configurations of the six representative cases in the full-wake and partial-wake configurations. . . . .	61
4.2	Power gains and DEL variations for the configurations with opposite yaw angles. . . . .	64
5.1	Configurations of the four simulation cases. . . . .	80





# 1 Introduction

*Only the refreshing wind on the water ..... is an exception.  
It never ends and is never exhausted.  
It is the infinite treasure granted to us by our Creator.*

— Su Dongpo, *Ode to the Red Cliff*, 1082.

Su Dongpo, a Chinese poet in the 11th century, was among many people in history who realised the abundance of wind energy in nature. For centuries, people have tried replacing human labour with wind power in various industries (Shepherd, 1990; Zhang, 2009). In the late 19th century, the first efforts of harnessing wind energy to generate electricity were made almost simultaneously in Scotland, Denmark and the United States (Kaldellis & Zafirakis, 2011). During the oil crisis in the 1970s, wind energy started to receive significant amounts of investment due to the demand for energy independence and security (Şahin, 2004). Since then, wind energy has witnessed rapid growth in the global installed capacity. In the last two decades, driven by the need for energy decarbonisation to tackle climate change, the global installed capacity of wind energy grew from 24 GW in 2001 to 837 GW in 2021 (GWEC, 2022). Nowadays, wind energy is the largest renewable energy source, accounting for 6.6% of global electricity generation (GWEC, 2022).

Throughout the development of wind energy, various wind turbine designs have been proposed by researchers. The variations of design included different axis layouts (vertical and horizontal) and blade numbers (two-blade, three-blade and more) (Gipe & Möllerström, 2022). With the increasing size and capacity of wind turbines, turbine design has gradually standardised to the so-called “Danish concept”: a three-blade, variable-speed, horizontal-axis wind turbine with a yaw mechanism (Dykes, 2013). The Danish-concept turbine is found to be the one with the best performance-to-cost balance among other designs. Nowadays, most wind turbines are based on the Danish concept, particularly for large multi-MW turbines (Burton et al., 2011).

Besides wind turbine designs, the form of wind energy projects has also transformed. In

the early days of wind energy, most projects were developed in the form of distributed wind power, i.e., installing a stand-alone wind turbine to meet local electricity demands (Gipe & Möllerström, 2022). With the increasing size and capacity of wind turbines, wind power developers gradually found that it is more cost-efficient to install multiple wind turbines within a designated area and form a wind farm. The electricity generated by wind farms is transmitted to consumption centres through high-voltage or ultra-high-voltage long-distance power grids (Yuan, 2016). By doing so, wind farm developers can maximise the wind energy potentials of favourable sites, and it is also convenient to maintain the turbines within a designated area. For example, one of the largest wind farms in the world, Hornsea 2, currently reaches a total capacity of 1.4 GW with 165 turbines, occupying an area of 462 km<sup>2</sup> and providing clean electricity for 1.4 million households (Glasson et al., 2022).

While developing wind energy projects in wind farms can bring many advantages, there is an important caveat. When the incoming wind passes through a turbine, the kinetic energy is extracted from the wind and creates a low-speed wake behind the turbine. As the wake develops further downwind, the low-speed wake mixes with the unaffected outer flow and recovers the velocity. However, in a wind farm, since the turbines are installed within a limited area, the distance between turbines may not be sufficient for wakes to recover fully. Therefore, in certain wind directions, downwind turbines are exposed to the wake of upwind turbines, causing significant power losses and increases in fatigue. This phenomenon is known as wake interference (Archer et al., 2018; Barthelmie & Jensen, 2010; Porté-Agel et al., 2020).

To mitigate the adverse effect of wake interference in wind farms, wind energy researchers have conducted numerous studies seeking solutions to this problem. For example, many studies focused on searching for optimal wind farm layouts in the design phase of a wind farm (Chowdhury et al., 2012; Kirchner-Bossi & Porté-Agel, 2018; Kusiak & Song, 2010; Samorani, 2013). At the operational level, researchers have also proposed several active control strategies to optimise the total power output of a wind farm (Bartl & Sætran, 2016; Gebraad et al., 2017; Goit & Meyers, 2015; Meyers et al., 2022; Munters & Meyers, 2018a). Among those proposed strategies, active yaw control (AYC), or active wake steering, is proven to be a promising solution that can effectively mitigate the power loss caused by wake interference (B. Li et al., 2022). Modern wind turbines are equipped with a yaw mechanism to change the rotor's orientation. Several experimental and numerical studies have shown that the wake behind a yawed turbine is deflected from the incoming wind direction (Atkinson & Wilson, 1986; Grant et al., 1997; Jiménez et al., 2010). This phenomenon inspired researchers to propose AYC as a viable control strategy for power optimisation (Grant & Parkin, 2000; Medici & Alfredsson, 2006; Parkin et al., 2001). For a wind farm subjected to AYC, while the yawed turbines are operated at sub-optimal conditions, the wind farm could achieve significant power gains thanks to the mitigation of wake interference.

However, previous studies have also shown that the flow physics of the wake behind a yawed turbine is significantly different from its non-yawed counterpart (Bastankhah & Porté-Agel, 2016; Grant & Parkin, 2000; Grant et al., 1997; Howland et al., 2016; Medici & Alfredsson, 2006).

---

Therefore, the wake models and turbine parametrisations previously developed and validated for non-yawed turbines are not always suitable for yawed turbines (Bastankhah & Porté-Agel, 2016; Qian & Ishihara, 2021; Qian & Ishihara, 2018). Furthermore, compared to non-yawed turbines, yawed turbines endure different structural loads (Damiani et al., 2018; Fleming et al., 2015; Kragh & Hansen, 2014; Zalkind & Pao, 2016). When AYC is applied to wind farms, it is necessary to jointly consider the power production and fatigue loads of the turbines. These issues have not been comprehensively addressed by previous studies. This thesis aims to fill the aforementioned gaps and extend our understanding of the best practices for modelling wind farms subjected to AYC.

The rest of this thesis is structured as follows. In Chapter 2, we validate a wind-turbine parametrisation for large-eddy simulation (LES) of a yawed stand-alone wind turbine with wind tunnel measurements. In Chapter 3, we extend the validation of LES for predicting the flow through a miniature wind turbine array subjected to AYC with wind tunnel measurements. In Chapter 4, we investigate the power production and blade fatigue of a utility-scale wind-turbine array using a two-way coupled framework of LES and aeroelastic simulation. In Chapter 5, we study the wake meandering of a wind-turbine array under dynamic yaw control (DYC) and the effects on the power and fatigue of the turbines. In Chapter 6, we give an overall summary of this thesis and provide an outlook on possible future studies.



## 2 LES of a yawed stand-alone wind turbine

### Abstract

In this study, we validate a wind-turbine parametrisation for large-eddy simulation (LES) of yawed wind-turbine wakes. The presented parametrisation is modified from the blade-element actuator disk model (ADM-BE), which takes account of both thrust and tangential forces induced by a wind turbine based on the blade-element theory. LES results using the ADM-BE are validated with wind-tunnel measurements of the wakes behind a stand-alone miniature wind turbine model with different yaw angles. Comparisons are also made with the predictions of analytical wake models. In general, LES results using the ADM-BE are in good agreement with both wind-tunnel measurements and analytical wake models regarding wake deflections and spanwise profiles of the mean velocity deficit and turbulence intensity. Moreover, the power output of the yawed wind turbine is directly computed from the tangential forces resolved by the ADM-BE, in contrast with the indirect power estimation used in the standard actuator disk model. We find significant improvement in the power prediction from LES using the ADM-BE over the simulations using the standard actuator disk, suggesting a good potential for the ADM-BE to be applied in LES studies of active yaw control in wind farms.

---

The contents of this chapter were published in: Lin, M., & Porté-Agel, F. (2019). Large-eddy simulation of yawed wind-turbine wakes: comparisons with wind tunnel measurements and analytical wake models. *Energies*, 12(23), 4574.

### 2.1 Introduction

The potential of applying unconventional control strategies seeking globally optimal power production for an wind farm has recently drawn increasing interest among researchers. Active yaw control (AYC) is one of those strategies in which certain wind turbines in a wind farm are subjected to yaw control to redirect their wakes from downwind wind turbines. While the yawed wind turbines no longer operate at their locally optimal conditions, their power losses could be compensated by the gains in the total wind farm power production due to weaker wake losses in the wind farm. One of the main challenges for applying the AYC is that yawed wind turbine wakes are markedly different in their structure, dynamics and interactions compared to their more-studied non-yawed counterparts. Therefore, to further exploit the potential of the AYC in wind farm optimisation, it is crucial to establish and validate modelling approaches that are capable of capturing the wakes behind yawed wind turbines with high fidelity.

Among a broad spectrum of methods used to study wind turbine wakes (Porté-Agel et al., 2019; Stevens & Meneveau, 2017), large-eddy simulation (LES) is a widely-used approach among researchers as it delivers higher fidelity than the Reynolds-averaged Navier–Stokes (RANS) approach. Due to the significant difference in scale between the largest turbulent eddies ( $\sim 10^3$  m) in the atmospheric boundary layer (ABL) and the chord length of wind turbine blades ( $\sim 1$  m), it is still computationally too expensive to perform blade-resolved LES of ABL flows through wind turbines (Lavelly et al., 2014). Therefore, most of the LES studies on wind turbine wakes represent the forces induced by wind turbines in ABL flows with various parametrisations.

The standard actuator disk model (ADM-std) is the simplest wind turbine parametrisation, in which a wind turbine is modelled as a permeable disk with uniformly-distributed normal thrust forces applied on it (Jiménez et al., 2007). A thrust coefficient  $C_T$  is required by the ADM-std *a priori* to determine the magnitude of the thrust force. Wu and Porté-Agel (2011) later proposed the blade-element ADM parametrisation (ADM-BE), also referred to as the rotational actuator disk model (ADM-R), in which the wind turbine thrust and tangential forces are modelled by the blade-element theory. Using aerodynamic and geometric data of the blade as inputs, the ADM-BE accounts for the wake rotation and non-uniform force distribution on the wind turbine disk. Compared to the LES results using the ADM-std, Wu and Porté-Agel (2011) found that using the ADM-BE improves the prediction of the main wake flow statistics, such as the mean streamwise velocity and turbulence intensity.

The actuator line model (ALM) parametrisation, developed by Sørensen and Shen (2002), was also applied in previous LES studies of wind turbine wakes (Martínez-Tossas et al., 2015; Porté-Agel et al., 2011a; Sørensen et al., 2015; Stevens et al., 2018). The ALM represents each blade of a wind turbine as a rotating line source of body forces and computes the corresponding blade-induced forces along the actuator line dynamically in the simulation. As the ALM computes the forces induced by each wind turbine blade, it can resolve more flow structures in the wake,

such as tip vortices, than the ADM-std and the ADM-BE parametrisations. Using the ALM in LES also requires finer mesh resolutions and timesteps to capture the moving blades. Such requirements often lead to greater computational costs than using the ADM-BE to produce similar predictions of wake profiles and wind turbine power (Martínez-Tossas et al., 2015; Porté-Agel et al., 2011a).

The first effort to study yawed wind turbine wakes in LES was made by Jiménez et al. (2010). Using the velocity component normal to the rotor disk, they parameterised the thrust force of a yawed wind turbine in a similar fashion to the ADM-std. This parametrisation was further applied by Munters and Meyers (2018a) and Boersma et al. (2018) to investigate control strategies for yaw and axial induction in wind farms for power optimisation. In their studies, the wind turbine power was obtained indirectly from the turbine-induced thrust and the local velocity. Fleming et al. (2018) applied the ADM-BE to study the large-scale trailing vortices in the wake behind of yawed wind turbine. The ALM parametrisation has also been adopted by Fleming et al. (2014) and Wang et al. (2017) to model the wake redirection behind yawed wind turbines in LES. As the ALM resolves the local aerodynamic forces acting on the turbine blade sections, the power and thrust of a yawed wind turbine are extracted directly from the parametrisation. Wang et al. (2017) also indicated that the AYC is a more effective control method to mitigate wake-induced power losses in wind farms than other proposed approaches, such as down-rating through pitch control.

Besides high-fidelity LES, researchers in the wind energy community have also developed several reduced-order models for yawed wind turbine wakes for engineering applications requiring fast predictions, e.g., wind farm layout optimisation and real-time control. An analytical model of yawed wind turbine wakes was first derived by Jiménez et al. (2010), in a similar fashion to the classical Jensen wake model (Jensen, 1983), assuming top-hat distributions of the velocity deficit and the wake skew angle in the wake. Later, Bastankhah and Porté-Agel (2016) developed a Gaussian analytical model for predicting the wake behind a yawed wind turbine based on the self-similarities of the velocity deficits and the wake skew angles. Similar to its non-yawed counterpart (Bastankhah & Porté-Agel, 2014), the Gaussian model is derived from the conservation of mass and momentum in the wake. Shapiro et al. (2018) developed a lifting line approach to predict the skew angle of the wake in the near-wake region behind a yawed wind turbine and adopted the same Gaussian profile for the wake velocity deficit in the far wake as in Bastankhah and Porté-Agel (2016). Qian and Ishihara (2018) derived a different Gaussian model for the velocity deficit with the assumption of a top-hat distribution for the skew angle, in contrast with the Gaussian distribution for the same quantity in Bastankhah and Porté-Agel (2016). In the same work, Qian and Ishihara (2018) formulated a bimodal Gaussian parametric model for the added turbulence intensity in yawed wind turbine wakes. Recent efforts were also made by Martínez-Tossas et al. (2019) and Bay et al. (2019) to develop a reduced-order model that captures the presence of a counter-rotating vortex pair (CVP) in the vertical  $y$ - $z$  cross-section plane of yawed wind turbine wakes, which has been observed in previous wind tunnel studies (Bastankhah & Porté-Agel, 2016; Howland et al., 2016).

Through reviewing the existing literature, we conclude that the ADM-BE could potentially be a good option for AYC-oriented LES, as it combines the favourable properties of the ADM-std, which is computationally cheap, and the ALM, which explicitly calculates the turbine-rotor torque. Such an advantage of using the ADM-BE in LES has been previously shown in the studies of non-yawed turbines (Martínez-Tossas et al., 2015; Porté-Agel et al., 2011a), but has not been validated in the context of yawed wind turbines. In the following sections, we present the implementation of the yawed ADM-BE in LES and validate it through comparisons of contours and profiles of the main wake flow statistics (the mean velocity deficit and the turbulence intensity) obtained from LES results, wind-tunnel measurements and analytical models (Bastankhah & Porté-Agel, 2016; Jiménez et al., 2010; Qian & Ishihara, 2018). Furthermore, we evaluate the ability of the ADM-BE to predict the power output of yawed wind turbines.

The rest of the chapter is organised as follows. In Section 2.2, we first discuss the LES framework for simulating yawed wind turbine wakes, including the governing equations, numerical setup and wind turbine parametrisation. In Section 2.3, we present the simulation results of yawed wind turbine wakes from LES and compare them with wind-tunnel measurements and predictions obtained from analytical wake models. Finally, we summarise the conclusions drawn from this investigation and possible future work in Section 2.4.

## 2.2 Large-eddy simulation framework

### 2.2.1 Governing equations

The simulations in this study are carried out using the in-house LES code developed at the Wind Engineering and Renewable Energy Laboratory (WiRE) of the École Polytechnique Fédérale de Lausanne (EPFL). It solves the spatially-filtered incompressible Navier-Stokes equations:

$$\begin{aligned} \frac{\partial \tilde{u}_i}{\partial x_i} &= 0, \\ \frac{\partial \tilde{u}_i}{\partial t} + \tilde{u}_j \left( \frac{\partial \tilde{u}_i}{\partial x_j} - \frac{\partial \tilde{u}_j}{\partial x_i} \right) &= -\frac{\partial \tilde{p}^*}{\partial x_i} - \frac{\partial \tau_{ij}}{\partial x_j} - \frac{f_i}{\rho} + \frac{F_p}{\rho} \delta_{i1}, \end{aligned} \quad (2.1)$$

where  $\tilde{u}_i$  is the filtered velocity component in the  $i$  direction (with  $i = 1, 2, 3$  representing the streamwise, spanwise and vertical directions, respectively),  $\tilde{p}^* = \tilde{p}/\rho + \frac{1}{2}\tilde{u}_i\tilde{u}_i$  is the modified kinematic pressure, in which  $\tilde{p}$  is the filtered pressure and  $\rho$  is the constant air density,  $f_i$  are the body forces exerted by the wind turbine to the flow,  $F_p$  is a pressure gradient imposed to drive the flow, and  $\tau_{ij} = \widetilde{u_i u_j} - \tilde{u}_i \tilde{u}_j$  is the kinematic sub-grid scale (SGS) stress, which is parameterised using the scale-dependent dynamic model with Lagrangian averaging (Porté-Agel et al., 2000; Stoll & Porté-Agel, 2006).



### 2.2.2 Wind turbine parametrisation

To parametrise the body forces induced by a yawed wind turbine, we implement the ADM-BE for yawed wind turbines, which is a modified version of the non-yawed parametrisation proposed by Wu and Porté-Agel (2011). As in its non-yawed counterpart, the wind turbine rotor disk in the ADM-BE is subdivided into axisymmetrically-arranged blade elements. The local flow velocity  $\mathbf{U}$  at a given blade element with respect to a mesh-aligned reference frame  $x$ - $y$ - $z$  is interpolated in 3D from the velocity of the adjacent computational cells. The wind turbine-induced force is then computed on each blade element with the infinite blade number assumption.

In the next step, the local velocity  $\mathbf{U}$  is transformed from the mesh-aligned reference frame  $x$ - $y$ - $z$  to the rotor-normal reference frame  $x'$ - $y'$ - $z'$  (Figure 2.1). With the transformed local velocity, the rotor-normal force  $F'_x$  and tangential force  $F'_\theta$  induced by a yawed wind turbine can be computed in a similar manner as in the non-yawed ADM-BE discussed by Wu and Porté-Agel (2011):

$$F'_x = \frac{1}{2} \rho |\mathbf{U}'_{\text{ref}}|^2 \frac{Bc}{2\pi r} \Phi(C_L \cos(\phi) + C_D \sin(\phi)), \quad (2.2)$$

$$F'_\theta = \frac{1}{2} \rho |\mathbf{U}'_{\text{ref}}|^2 \frac{Bc}{2\pi r} \Phi(C_D \cos(\phi) - C_L \sin(\phi)), \quad (2.3)$$

where  $B$  is the number of blades,  $c$  is the blade chord length at the location of the blade element centre, and  $r$  is the distance of the blade element centre to the rotor hub.  $\mathbf{U}'_{\text{ref}}$  is the resultant velocity that the blade element experiences with respect to a non-inertial reference frame fixed to a blade rotating at angular velocity  $\Omega$  in the flow:

$$\mathbf{U}'_{\text{ref}} = u'_x \mathbf{e}_i + (\Omega r - u'_\theta) \mathbf{e}_j, \quad (2.4)$$

where  $u'_x$  and  $u'_\theta$  are the axial and tangential components of the transformed flow velocity at the blade element.  $\phi$  is the angle between the axial and the relative tangential velocity components at the blade element:

$$\phi = \arctan\left(\frac{u'_x}{\Omega r - u'_\theta}\right). \quad (2.5)$$

$\Phi$  is Prandtl's tip loss factor introduced to correct the assumption of an infinite number of blades in the ADM:

$$\Phi = \frac{2}{\pi} \arccos\left(\exp\left(-\frac{B}{2} \frac{R-r}{r \sin \phi}\right)\right). \quad (2.6)$$

The angle of attack  $\alpha$  of the blade element is calculated from  $\phi$  and the local pitch angle  $\beta$ :

$$\alpha = \phi - \beta. \quad (2.7)$$

Given  $|\mathbf{U}'_{\text{ref}}|$  and  $\alpha$ , the lift coefficient  $C_L$  and drag coefficient  $C_D$  at the blade element are

interpolated from the tabular aerodynamic data of the WiRE-01 blade profile (Revaz et al., 2020).

Finally, the turbine-induced forces  $\mathbf{F}'$  computed in the rotor-normal reference frame are projected back to the original mesh-aligned reference frame  $x$ - $y$ - $z$ . Then, the projected forces  $\mathbf{F}$  are distributed to the neighbouring Cartesian computational nodes using a 3D radial Gaussian smoothing kernel (shown in Figure 2.2), as proposed by Sørensen et al. (1998) and Mikkelsen (2003):

$$g(r) = \frac{1}{\epsilon^3 \pi^{3/2}} \exp\left(-\frac{r^2}{\epsilon^2}\right), \quad (2.8)$$

where  $r$  is the distance from the Cartesian nodes to the blade element centre and  $\epsilon$  is the smearing parameter. Therefore, the actual forcing applied on the computational nodes is:

$$\mathbf{f} = \frac{\mathbf{F} * g(r)}{M_{cell}}, \quad (2.9)$$

where  $*$  denotes the convolution operation, and  $M_{cell}$  is the volume of the cell.

The forces induced by the wind turbine tower and nacelle are parametrised as drag forces with the same formulation of the thrust in the ADM-std:

$$f_{tower} = \frac{1}{2} \rho A_{tower} \bar{u}_{in}^2 C_{D,tower}, \quad f_{nac} = \frac{1}{2} \rho A_{nac} \bar{u}_h^2 C_{D,nac}. \quad (2.10)$$

$\bar{u}_{in}$  is the mean incoming streamwise velocity at different heights, and  $\bar{u}_h$  is the mean incoming streamwise velocity at the hub.  $A_{tower}$  is the frontal area of the turbine tower section at different heights and  $A_{nac}$  is the total frontal area of the nacelle and the accessories on the nacelle. The drag coefficient of the tower is chosen as  $C_{D,tower} = 1.2$ , modelled as a cylinder perpendicular to the inflow. The nacelle is modelled as a front-facing yawed cylinder, and its drag coefficient  $C_{D,nac}$  is chosen as 0.81, 0.87 and 0.92 for yaw angles of  $10^\circ$ ,  $20^\circ$  and  $30^\circ$  respectively. Such choice of  $C_{D,nac}$  values is obtained by interpolating the results of previous experimental studies of the aerodynamic performance of a yawed cylinder (Smith et al., 1972; Willmarth & Wei, 2021).

### 2.2.3 Numerical setup

The filtered governing equations (Eq. 2.1) are solved numerically by the pseudospectral method in the horizontal directions and by a second-order finite difference scheme in the vertical direction. The grid points are staggered in the vertical direction, i.e., the horizontal velocity components  $\tilde{u}$ ,  $\tilde{v}$  and the modified pressure  $\tilde{p}^*$  are located at the cell centre, while the vertical velocity component  $\tilde{w}$  is located at the centre of the bottom of the cell. Such choice of numerical schemes is similar to the one used in classical studies of turbulent boundary layer flows (Moeng, 1984; Moin & Kim, 1982) and has also been applied in previous studies of wind turbine and wind farm flows using the same LES code (Porté-Agel et al., 2011a; Wu &

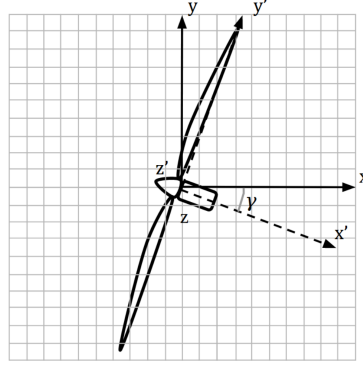


Figure 2.1: Reference-frame transformation from mesh-aligned  $x$ - $y$ - $z$  to rotor-normal  $x'$ - $y'$ - $z'$  for a wind turbine of a yaw angle  $\gamma$ . The positive yaw angle is defined as the clockwise direction viewing from the top.

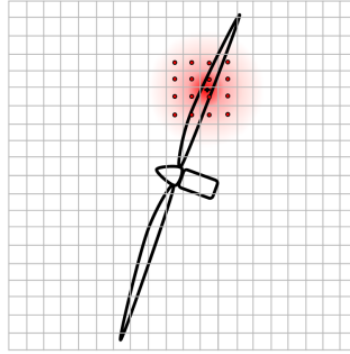


Figure 2.2: Force smearing from blade elements to neighbouring computational cells.

Porté-Agel, 2011, 2012; Wu & Porté-Agel, 2013).

The simulation configuration consists of a fully-developed neutral boundary-layer flow through a stand-alone miniature wind turbine on a flat surface, which matches the experimental conditions in the wind-tunnel study performed by Bastankhah and Porté-Agel (2016). The main characteristic quantities of the incoming boundary-layer flow measured in the wind tunnel are summarised in Table 2.1.

The geometric parameters of the miniature wind turbine, WiRE-01 (Bastankhah & Porté-Agel, 2017), used in the wind-tunnel experiments (Bastankhah & Porté-Agel, 2016) are shown in Figure 2.3b. The number of the computational cells in the streamwise ( $x$ ), spanwise ( $y$ ) and vertical ( $z$ ) directions for four cases with different mesh resolutions are summarised in Table 2.2. For all cases, the cells are equidistantly arranged in each direction, which results in 9 to 24 nodes along the diameter of the wind turbine rotor disk  $d$ . In the following sections, if not specified, the presented simulation results are obtained from Case 3 with an intermediate resolution.

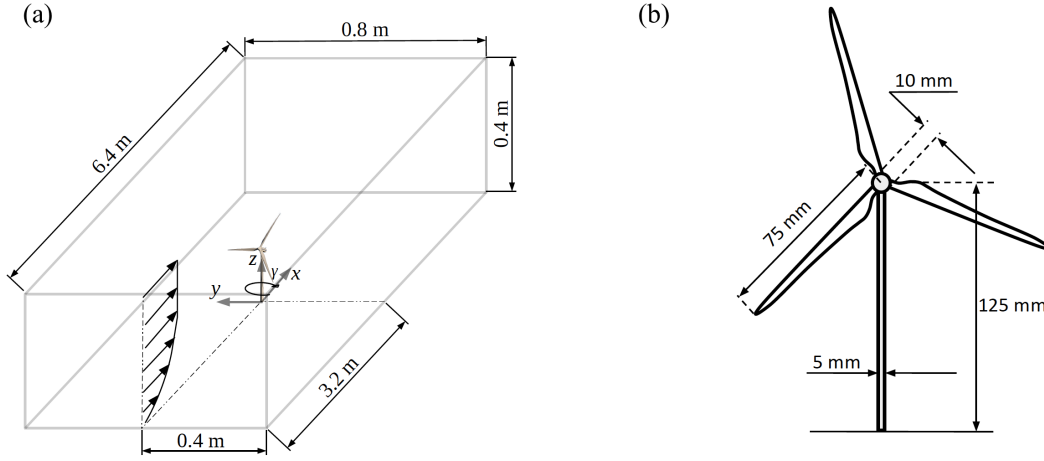


Figure 2.3: Schematic plots of (a) the simulation domain; (b) the WiRE-01 miniature wind turbine.

Periodic boundary conditions are imposed on the lateral boundaries in the  $x$  and  $y$  directions. On the upper surface of the domain, a frictionless slip-wall boundary condition is applied. On the lower surface, the wall shear stress is specified using the log law of the wall with local filtered variables, as commonly done in LES studies of ABL flows (Allaerts & Meyers, 2015; Chow et al., 2005; Moeng, 1984; Porté-Agel et al., 2000). Specifically, the wall shear stress is computed using the instantaneous filtered velocity at the first  $u$  node above the surface as follows:

$$\tau_{i3}|_w = -u_*^2 \left( \frac{\tilde{u}_i}{U_{avg}} \right) = - \left( \frac{U_{avg} \kappa}{\ln(z/z_0)} \right)^2 \left( \frac{\tilde{u}_i}{U_{avg}} \right), \quad i = 1, 2, \quad (2.11)$$

where  $\tau_{i3}|_w$  is the instantaneous spatially-filtered wall stress,  $u_*$  is the local friction velocity,  $U_{avg}$  is the plane-averaged spatially-filtered horizontal velocity,  $\kappa = 0.4$  is the von Kármán constant,  $z_0$  is the aerodynamic surface roughness length, and  $z = \Delta z/2$  is the vertical distance of the first level of  $u$  nodes from the lower surface.

A turbulent inflow condition is generated by a precursor simulation of a fully-developed pressure-driven neutral boundary-layer flow without any wind turbine. The velocity fields of

Table 2.1: Main characteristics of the incoming boundary-layer flow.

Inflow characteristic	Value
Boundary-layer height ( $H$ )	0.4 m
Hub-height incoming velocity ( $\bar{u}_h$ )	4.88 m/s
Hub-height turbulence intensity ( $I_u$ )	7%
Surface roughness length ( $z_0$ )	0.022 mm
Friction velocity ( $u_*$ )	0.22 m/s

the precursor simulation are enforced as the inflow condition of another simulation, referred to as the “main simulation”. The main simulation has the same numerical setup as the precursor one but with the wind turbine. A smooth transition function is applied in a buffer zone in front of the enforced inlet in the main simulation to prevent the numerical artefacts induced by abrupt changes in the flow. By doing so, the periodic boundary conditions in the horizontal directions can still be used in the main simulation while avoiding the re-entries of the wind turbine wake. This method for inflow turbulence generation has been successfully applied in previous LES studies of turbine wakes (Churchfield et al., 2012; Wu & Porté-Agel, 2011; Wu & Porté-Agel, 2013).

## 2.3 Results

### 2.3.1 Inflow conditions

In Figure 2.4, the vertical profiles of the normalised mean streamwise wind speed and stream-wise turbulence intensity obtained from the precursor LES are compared with the wind-tunnel measurements of Bastankhah and Porté-Agel (2016). A good agreement is found between the simulation results and the measurements, proving that inflow conditions similar to the wind-tunnel experiments in Bastankhah and Porté-Agel (2016) are created by the precursor simulation.

### 2.3.2 Velocity deficit and turbulence intensity contours

Contours of the normalized mean streamwise velocity deficit  $\Delta\bar{u}/\bar{u}_{hub}$  in the spanwise  $x$ - $y$  cross-section plane at the hub height are shown in Figure 2.5 for yaw angles of  $10^\circ$ ,  $20^\circ$  and  $30^\circ$ , respectively. In agreement with the wind-tunnel measurements (Figure 2.5a), the simulated wakes behind a yawed wind turbine parametrised by the ADM-BE (Figure 2.5b) are deflected towards the downwind-inclined side of the rotor disk, and the wake deflection increases with the wind turbine yaw angle. Good agreement is also found between the wake-centre trajectories (defined as the locations of the maximum velocity deficit) obtained from wind-tunnel measurements and those computed from LES results for all yaw angles considered

Table 2.2: Mesh resolutions of different simulation cases.  $N_{d,y}$  and  $N_{d,z}$  represent the number of cells covering the turbine rotor in the  $y$  and  $z$  directions, respectively, in the non-yawed case.

Case No.	$N_x$	$N_y$	$N_z$	$N_{d,y}$	$N_{d,z}$
1	256	128	64	24	24
2	128	64	64	12	24
3	128	64	32	12	12
4	96	48	24	9	9

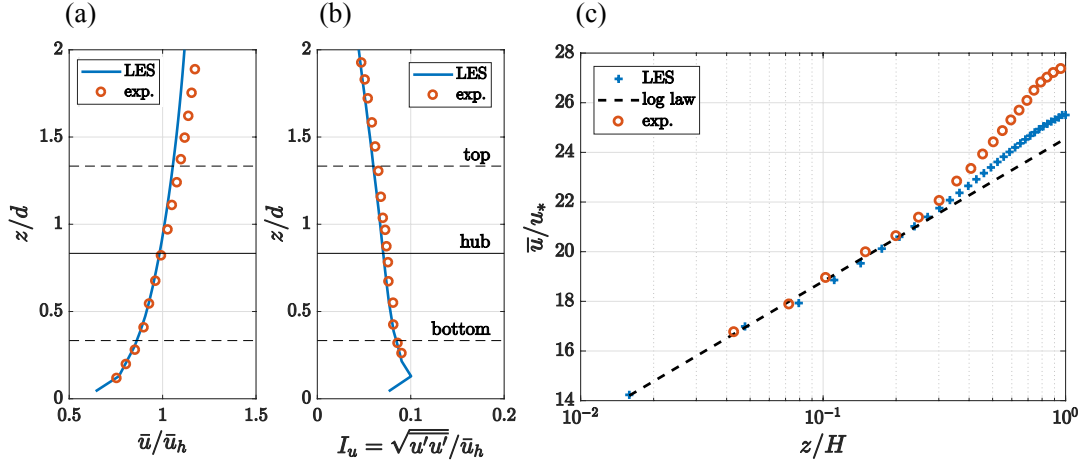


Figure 2.4: (a) Vertical profiles of the normalised mean streamwise velocity component  $\bar{u}/\bar{u}_h$ ; (b) Vertical profiles of the streamwise turbulence intensity  $I_u$ ; (c) Log-law velocity profiles plotted against the vertical profiles of the mean streamwise velocity component normalised by the friction velocity  $u_*$ .

here.

Figure 2.6 offers another view of the wakes behind the yawed wind turbine in the vertical  $y$ - $z$  cross-section plane at the downwind location  $x/d = 6$ , for the three yaw angles under consideration. The contours of the normalised streamwise mean velocity deficit  $\Delta\bar{u}/\bar{u}_h$  obtained from wind-tunnel measurements and LES using the ADM-BE and the ADM-std are shown in Figure 2.6. A kidney-shaped velocity deficit region is found in the wind tunnel measurements (Figure 2.6a), particularly in the cases of large yaw angles. For the small yaw angle case ( $\gamma = 10^\circ$ ), the experimental data show that the wake rotation dominates the flow. This pattern is well captured by the ADM-BE but not by the ADM-std, which produces a CVP largely symmetrical to the turbine hub. Such a discrepancy occurs because the ADM-std does not exert disk-tangential forces on the flow, thus inducing no wake rotation. For the cases of larger yaw angles ( $\gamma = 20^\circ$  or  $30^\circ$ ), the asymmetrical CVP becomes more identifiable in the experimental data. The ADM-BE also reproduces these features of the CVP. In contrast, the ADM-std produces an overly symmetrical CVP about the hub height. Such results are in agreement with the recent study of yawed turbine wakes performed by Zong and Porté-Agel (2020b), which highlights the role of wake rotation in the onset and the deformation of the CVP.

Figure 2.7 shows the added streamwise turbulence intensity  $I_{u,add}$  in the vertical  $y$ - $z$  cross-section plane at the downwind location  $x/d = 6$ , for the three yaw angles under consideration. We observe that, in contrast with the symmetrical horseshoe-shaped distribution of the added streamwise turbulence intensity  $I_{u,add}$  in non-yawed wind turbine wakes (Wu & Porté-Agel, 2011), the distribution of  $I_{u,add}$  in the yawed wind turbine wake is asymmetric, bending towards the side where the wake is deflected to. Compared with the ADM-std, the ADM-BE

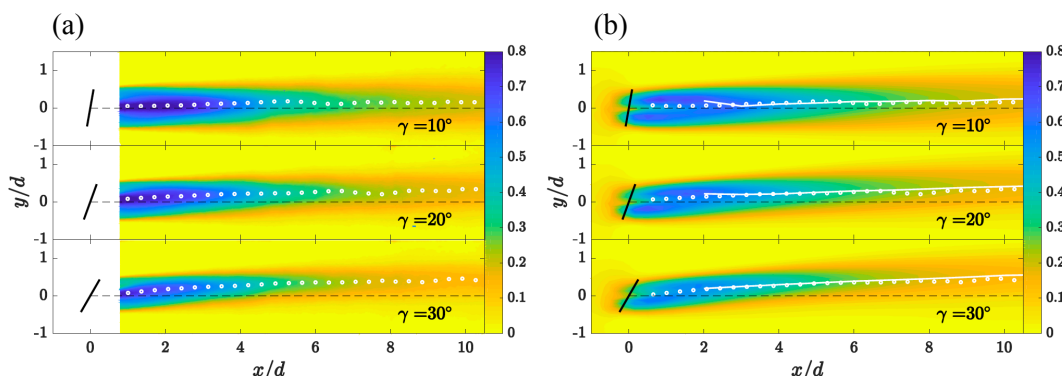


Figure 2.5: Contours of the normalised streamwise mean velocity deficit  $\Delta\bar{u}/\bar{u}_h$  in the  $x$ - $y$  cross-section plane at the hub height obtained from (a) the wind-tunnel experiments and (b) the LES using the ADM-BE. White circles represent the wake-centre trajectories for the experiment results and white solid lines for the simulation results.

in LES improves the prediction of the magnitude of the turbulence intensity in the wake, particularly in the upper part. However, the ADM-BE still underestimates the turbulence intensity in the lower part of the wake. A possible explanation for this discrepancy is that, compared to the upper part of the yawed rotor disk, the blade sections in the lower part encounter larger angles of attack. As a result, the actual aerodynamic lift and drag coefficients ( $C_L$  and  $C_D$ ) of the blade sections in the lower part of the rotor are likely to deviate more from the 2D tabular aerodynamic data used in the parametrisation, compared to those of the blade sections in the upper part.

### 2.3.3 Spanwise Velocity Deficit and Turbulence Intensity Profiles

The horizontal profiles of the normalised streamwise velocity deficit for different yaw angles are shown in Figure 2.8. LES results from the ADM-BE are compared with wind-tunnel measurements, predictions from the Gaussian-based analytical wake models (Bastankhah & Porté-Agel, 2016; Qian & Ishihara, 2018), as well as the LES results using the ADM-std. As shown in Figure 2.8, the LES results using the ADM-BE are in good agreement with the experimental data, despite a small bias towards larger wake deflection. From  $6d$  downwind, good consistency is found in the velocity deficit profiles between the measurements, the predictions of the Bastankhah–Porté-Agel model and the LES results using the two turbine parametrisations considered here. The Qian–Ishihara model underestimates the velocity deficits in the wakes for the cases of  $10^\circ$  and  $20^\circ$  yaw angles.

To further illustrate the differences between the LES results, analytical wake model predictions and wind-tunnel measurements, we compare the maximum velocity deficits and the wake-centre locations in Figure 2.9. We observe in Figure 2.9a that, for all yaw angles, the ADM-BE gives slightly better predictions of the maximum velocity deficit than the ADM-std,

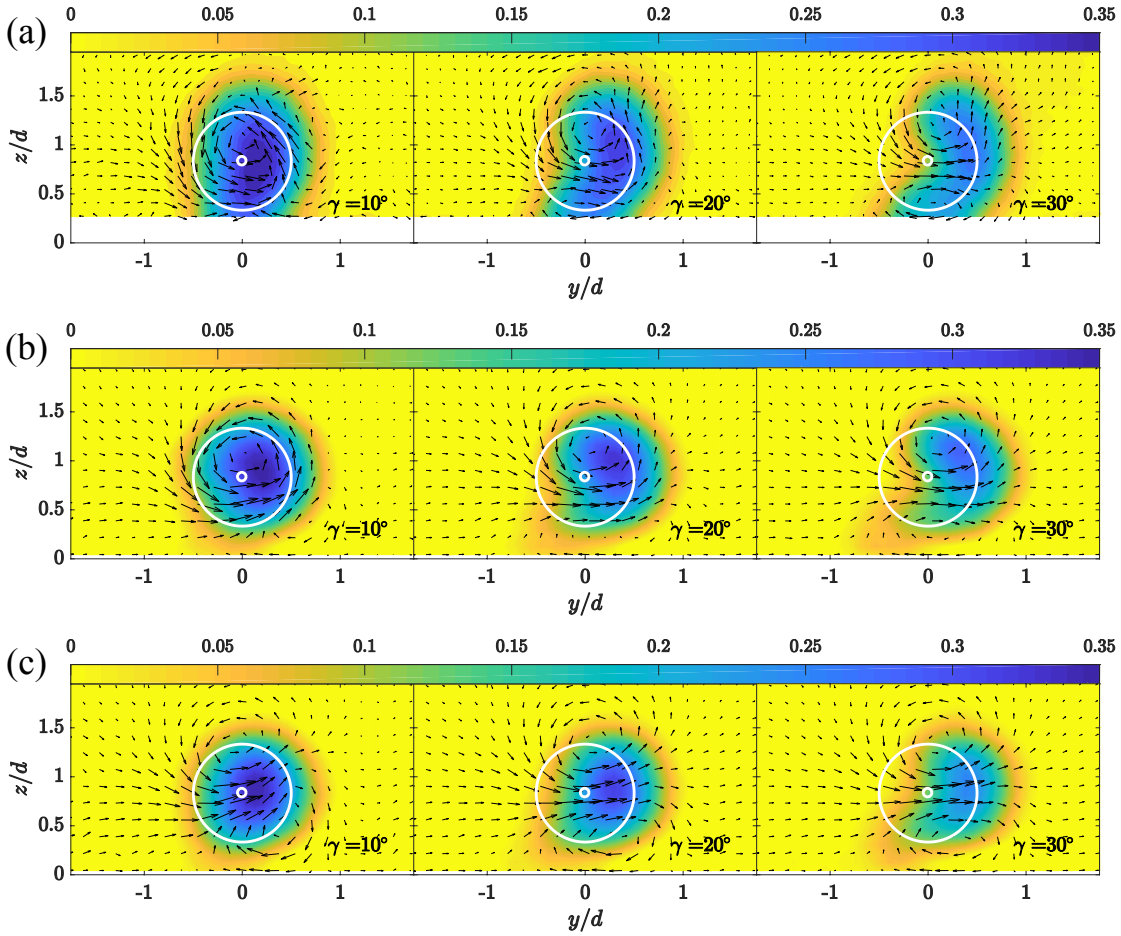


Figure 2.6: Contours of the normalised streamwise velocity deficit  $\Delta \bar{u} / \bar{u}_h$  for different yaw angles  $\gamma$ , overlapped with vector fields of the inplane velocity in the  $y$ - $z$  cross-section plane at  $x/d = 6$ : (a) wind-tunnel measurements; (b) LES using the ADM-BE; (c) LES using the ADM-std. White circles outline the edges of the non-yawed turbine rotor.

which under-predicts the velocity deficit more before  $x/d = 5$ . As the wakes develop further downwind, the LES results gradually converge to the wind-tunnel measurements. They are also in good agreement with the Bastankhah–Porté-Agel model, which is formulated to be applied in the far wake region. As we indicated previously, the Qian–Ishihara model under-predicts the maximum velocity deficit for the cases of  $10^\circ$  and  $20^\circ$  yaw angles. The Jiménez model (Jiménez et al., 2010) shows the largest deviation from the experiment results because it assumes a top-hat velocity deficit profile. Figure 2.9b indicates that the Jiménez model also significantly overestimates the wake deflection for all yaw angles considered here. The results from the LES and the other two Gaussian analytical models, in terms of predicting the wake deflection, are in much better agreement with the wind-tunnel measurements. LES using the ADM-BE exhibits small biases towards overestimating the wake deflections with respect to the measurements, while the ADM-std slightly underestimates the wake deflection in the case of the small yaw angle ( $\gamma = 10^\circ$ ). A bias similar to the ADM-BE towards over-predicting the



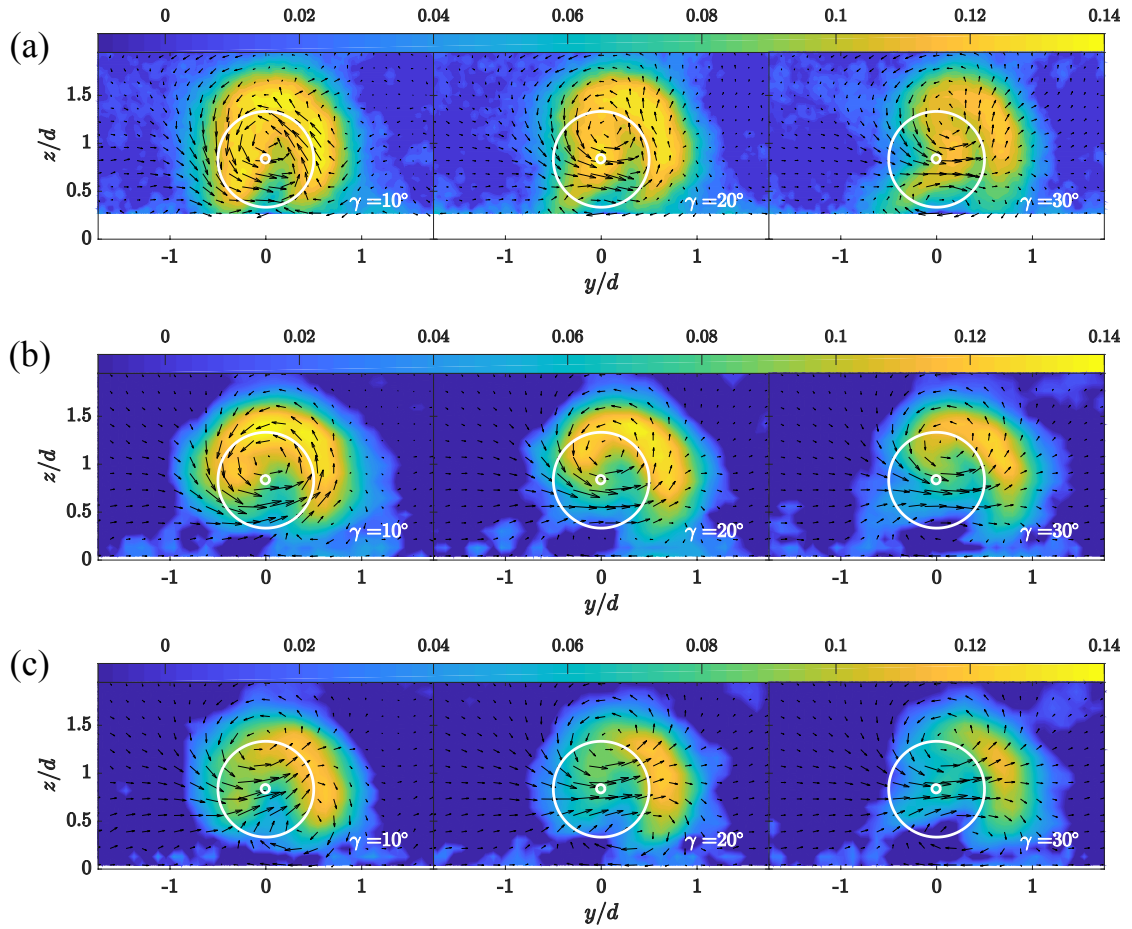


Figure 2.7: Contours of the added streamwise turbulence intensity  $I_{u,add}$  for different yaw angles  $\gamma$ , overlapped with vector fields of the inplane velocity in the vertical  $y$ - $z$  cross-section plane at  $x/d = 6$ : (a) wind-tunnel measurements; (b) LES using the ADM-BE; (c) LES using the ADM-std. White circles outline the edges of the non-yawed turbine rotor.

wake deflections is found in the Bastankhah-Porté-Agel model. In contrast, the Qian-Ishihara model yields slightly better wake deflection prediction in the cases of  $\gamma = 20^\circ$  and  $\gamma = 30^\circ$ .

The spanwise profiles of the normalised streamwise turbulence intensity are shown in Figure 2.10 for the three yaw angles under consideration. LES results using the ADM-BE and the ADM-std are compared with wind-tunnel measurements and the predictions from the Qian-Ishihara model. The Bastankhah-Porté-Agel model and the Jiménez model are not shown in this plot because they do not predict the turbulence intensity distribution in the wake. As shown in Figure 2.10, the ADM-BE outperforms the ADM-std in terms of the predictions of turbulence intensity in the wakes up to  $x/d = 6$ , particularly on the side opposite to the wake deflection. The Qian-Ishihara model provides acceptable predictions of the maximum turbulence intensity in the wake for cases with small yaw angles, but it overestimates the horizontal variance of the turbulence intensity distribution. Moreover, the Qian-Ishihara model for the wake turbulence is based on a bimodal Gaussian profile of equal amplitude,

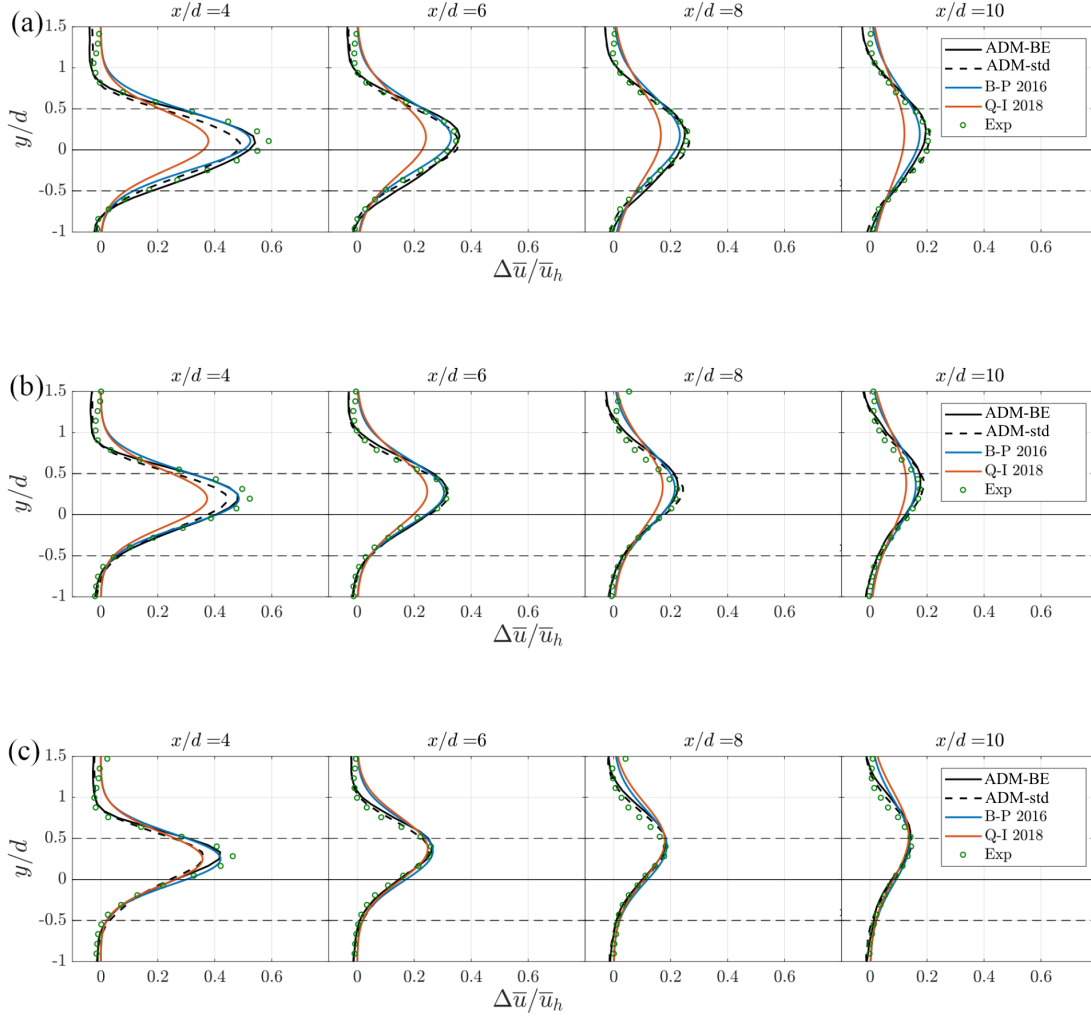


Figure 2.8: Spanwise profiles of the normalised mean streamwise velocity deficit  $\Delta\bar{u}/\bar{u}_h$ : (a)  $\gamma = 10^\circ$ ; (b)  $\gamma = 20^\circ$ ; (c)  $\gamma = 30^\circ$ .

which cannot capture the asymmetric nature of the turbulence in the wakes behind yawed wind turbines revealed by both LES results and wind-tunnel measurements.

Finally, to examine the mesh convergence of the LES results using the ADM-BE parametrisation, spanwise profiles of the mean streamwise velocity deficit at the hub-height from Cases 1 to 4 listed in Table 2.2 are shown in Figure 2.11. Good mesh convergence is observed for the resolution range considered in this study. This observation aligns with the conclusion of previous LES studies of non-yawed wind turbine wakes, which indicate that a resolution with more than seven grid points along the rotor diameter is sufficient for the ADM-BE parametrisation (Wu & Porté-Agel, 2011, 2012) to resolve the wind turbine forces. We also notice that the bias towards larger wake deflection is not eliminated by refining the mesh. We speculate that such a bias could be attributed to some missing phenomena in the near-wake region induced by the ADM-BE, e.g., tip vortices, that might affect the initial wake skew angle prediction.

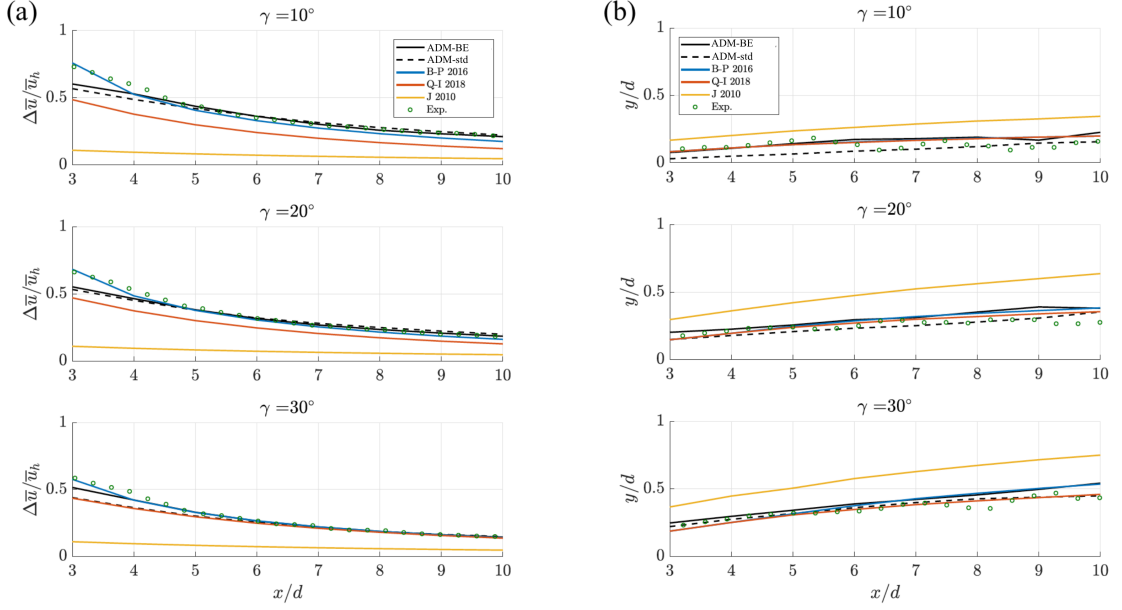


Figure 2.9: Comparisons of LES results and analytical wake model predictions with respect to wind-tunnel measurements: (a) maximum velocity deficit; (b) wake-centre location.

### 2.3.4 Mechanical power predictions

To evaluate the ability of the ADM-BE to predict the power of a yawed wind turbine, we compare the power outputs obtained from LES results using the ADM-BE and the ADM-std with the power measured in the wind-tunnel experiments. In the case of LES using the ADM-BE, the mechanical power of the wind turbine is directly obtained from the tangential forces  $F_\theta$  resolved by the ADM-BE parametrisation on the rotor disk:

$$P_{ADM-BE} = \omega \sum_{i=1}^N r_i F_{\theta i}, \quad (2.12)$$

in which  $\omega = 247$  rad/s is the rotor angular velocity.  $r_i$  and  $F_{\theta i}$  are the distance to the hub-centre and the resolved tangential force of the  $i$ th blade element, respectively. In contrast, in the case of LES using the ADM-std, the power extracted by the wind turbine from the incoming flow is estimated indirectly from the rotor-averaged thrust force  $F_x$  and the rotor-normal flow velocity  $u_d$  at the wind turbine (Hansen, 2015; Munters & Meyers, 2018a; Munters & Meyers, 2017):

$$P_{ADM} = F_x u_d. \quad (2.13)$$

It is worth noting that the mechanical power  $P_{Mech}$  extracted by the miniature wind turbine from the flow is not measured directly in the wind tunnel experiments carried out by Bas-tankhah and Porté-Agel (2016). Therefore, a conversion is needed to compare with the power

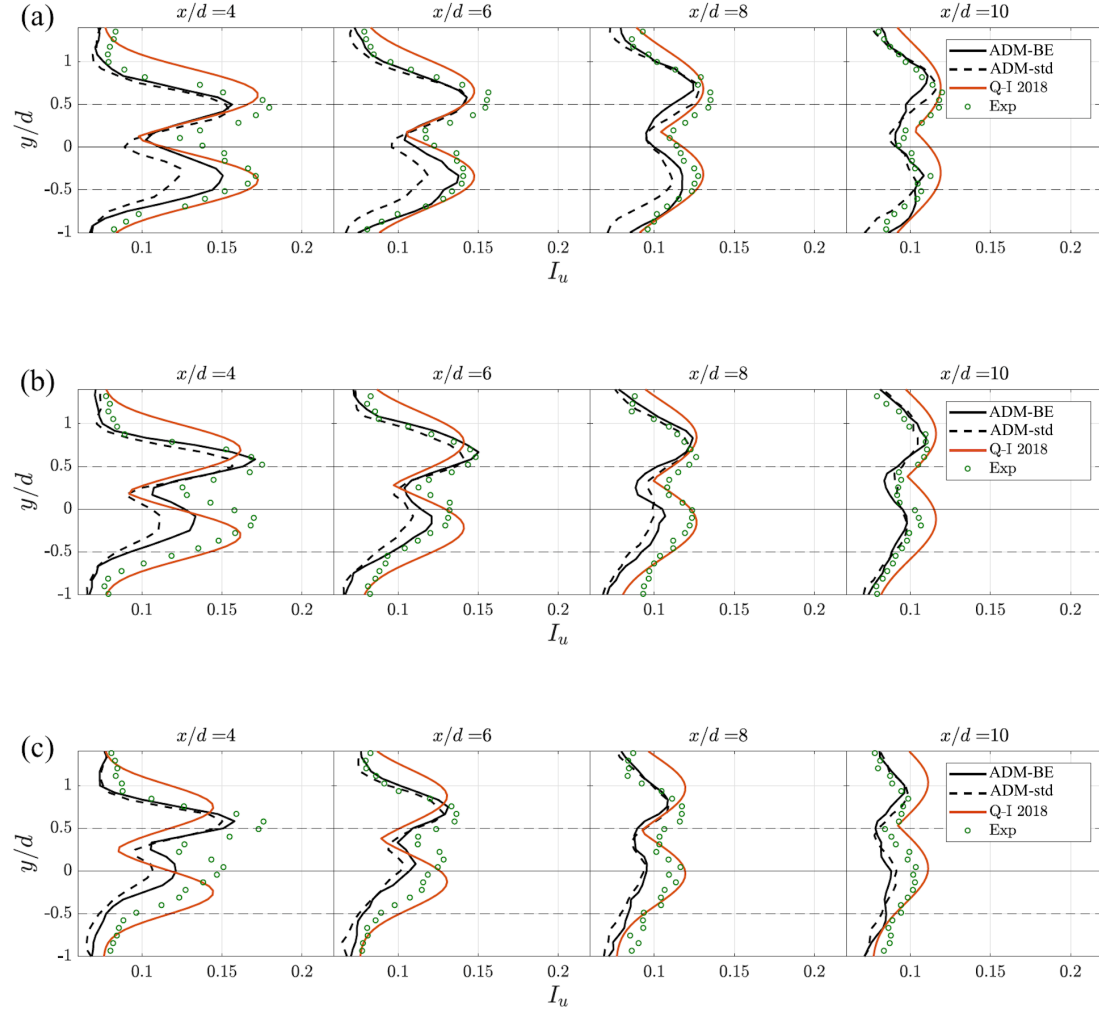


Figure 2.10: Spanwise profiles of the streamwise turbulence intensity  $I_u$ : (a)  $\gamma = 10^\circ$ ; (b)  $\gamma = 20^\circ$ ; (c)  $\gamma = 30^\circ$ .

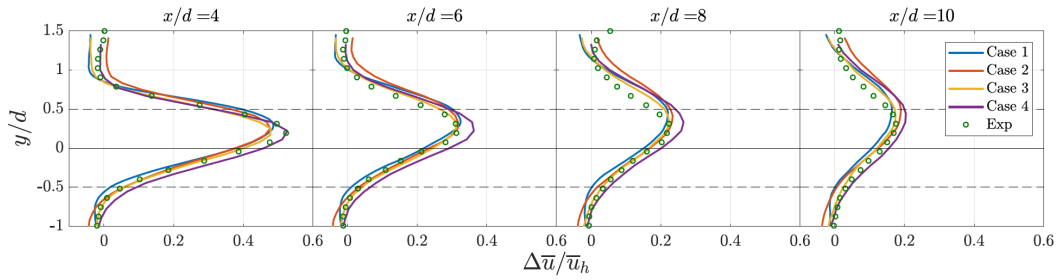


Figure 2.11: Spanwise profiles of the normalised mean streamwise velocity deficit  $\Delta \bar{u} / \bar{u}_h$  of the wake behind a wind turbine with a yaw angle  $\gamma = 20^\circ$ , obtained from the LES using the ADM-BE using different mesh resolutions.

output obtained from LES. In the miniature wind turbine under consideration, the mechanical power  $P_{Mech}$  is converted into the electrical power output  $P_e$  through a shaft and a generator as follows:

$$P_{Mech} = \underbrace{P_e + P_j}_{P_{conv}=KI} + P_f, \quad (2.14)$$

in which  $P_j$  is the electrical loss in the DC generator due to the electrical resistance and  $P_f$  is the shaft friction loss. The sum of  $P_e$  and  $P_j$  is the converted power  $P_{conv}$  and can be computed by the product of the electrical current output  $I$  and the torque constant of the generator  $K$  (Bastankhah & Porté-Agel, 2016). Bastankhah and Porté-Agel (2017) later found that, at the optimal tip speed ratio specified in this study ( $\lambda = 3.8$ ), the ratio between  $P_{conv}$  and  $P_{Mech}$  equals 0.92 for this specific miniature wind turbine model, WiRE-01.

The mechanical power extracted by the rotor using both the yawed ADM-BE parametrisation and the ADM-std is compared with the mechanical power obtained from the wind-tunnel experiments (Bastankhah & Porté-Agel, 2016) in Figure 2.12. The ADM-BE shows significant improvement in the power prediction with respect to the ADM-std for all yaw angles. The improvement can be explained by the fact that the ADM-BE explicitly computes the tangential force component that contributes directly to the torque and, thus, to the mechanical power extracted from the wind by the wind turbine rotor.

## 2.4 Summary

In this study, we present and validate a blade-element-actuator disk model to parameterise the forces induced by a yawed wind turbine on the flow. By comparing the wind-tunnel measurements, the analytical model predictions and the LES results, we find that the LES using the ADM-BE, in comparison with the ADM-std, can provide improved predictions of the mean streamwise velocity deficit and the streamwise turbulence intensity in the yawed turbine wakes. However, a small bias towards overestimating the wake deflection is also observed in the results using the ADM-BE. The origin of this bias should be the subject of future studies. LES using the ADM-BE can reproduce the interaction between the wake rotation and the CVP in the vertical  $y$ - $z$  cross-section plane of yawed wind turbine wakes, which has been observed in wind-tunnel experiments. The ADM-std, on the other hand, fails to capture such interaction, as it does not induce wake rotation.

We also find that using the ADM-BE in LES markedly improves the turbine power prediction compared to using the ADM-std, which significantly overestimates the turbine power compared to the wind tunnel measurements. Such validation of the ADM-BE on the power prediction is particularly valuable for LES applications in the optimisation-oriented AYC in wind farms. In practice, those applications often require accurate predictions of wind turbine power and wake characteristics, as well as affordable computational costs, allowing the iterative searching of the optimal AYC strategy to be performed. The ADM-BE validated

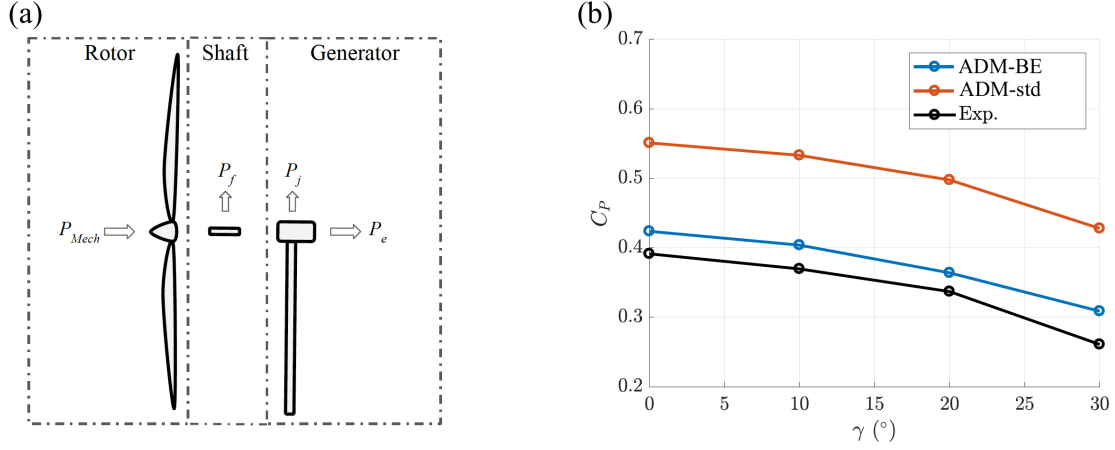


Figure 2.12: (a) Conversion of power in the miniature wind turbine model: Mechanical power  $P_{Mech}$ , Shaft friction loss  $P_f$ , Electrical loss  $P_j$  and Electrical power  $P_e$ . (b) Mechanical power coefficient  $C_p$  for yaw angles  $0^\circ$ - $30^\circ$  obtained from the LES results and the wind-tunnel experiments.

in this study provides a good option for those applications. Besides its ability to reproduce the main characteristics of yawed turbine wakes, the ADM-BE also computes more realistic wind turbine power than the ADM-std while avoiding incurring higher computational costs required by the ALM. To the best of our knowledge, this is the first time that such a validation of the ADM-BE for yawed wind turbines has been performed.

The wind turbine parametrisation validated in this study can be used to investigate optimal wind farm operation strategies based on the AYC. In the next step, we plan to further apply the LES framework established in this study in multi-wind turbine cases with the AYC. Furthermore, as the forces exerted by the flow on the wind turbine are explicitly computed, the validated turbine parametrisation can also be applied to the joint optimisation of the power and the structural loads in wind farms using the AYC.

### 3 LES of a wind-turbine array subjected to active yaw control

#### Abstract

This study validates the large-eddy simulation (LES) for predicting the flow through a wind turbine array subjected to active yaw control. The wind turbine array consists of three miniature wind turbines operated in the non-yawed and yawed configurations under full-wake and partial-wake conditions, for which wind tunnel flow measurements are available. The turbine-induced forces are parametrised by three different models: the standard actuator disk model (ADM-std), the blade element actuator disk model (ADM-BE), also referred to as the rotational actuator disk model (ADM-R), and the actuator line model (ALM). The time-averaged turbine power outputs and the profiles of the wake flow statistics (normalised streamwise mean velocity and streamwise turbulence intensity) obtained from the simulations using the ADM-std, the ADM-BE and the ALM are compared with experimental results. We find that simulations using the ADM-BE and ALM yield flow statistics that are in good agreement with the wind-tunnel measurements for all the studied configurations. In contrast, the results from LES with the ADM-std show discrepancies with the measurements under yawed and partial-wake conditions. These errors are due to the fact that the ADM-std assumes a uniform thrust force, thus failing to capture the inherently inhomogeneous distribution of the turbine-induced forces under partial wake conditions. In terms of power prediction, we find that LES using the ADM-BE yields better power predictions than the ADM-std and the ALM in the cases considered in this study. As a result, we conclude that LES using the ADM-BE provides a good balance of accuracy and computational cost for the simulations of the flow through wind farms subjected to AYC.

---

The contents of this chapter were published in: Lin, M., & Porté-Agel, F. (2022). Large-eddy simulation of a wind-turbine array subjected to active yaw control. *Wind Energ. Sci.*, 7, 2215–2230.

### 3.1 Introduction

As an indispensable part of the global transition to carbon neutrality, wind power has experienced a rapid growth worldwide in the past decades (GWEC, 2022). Most wind power projects are developed in the form of wind farms, i.e., a cluster of wind turbines installed within a designated area, outputting the generated electricity to centralised substations before transmitting it to the grid. Compared with distributed wind power, which consists of installing stand-alone turbines in different locations, developing wind energy in wind farms has many advantages, such as reducing the construction and maintenance overhead per turbine. On the other hand, wind turbines in wind farms often encounter wake interference, i.e., wind turbines are exposed to the wakes of upwind turbines. This phenomenon can cause significant power losses and increase fatigue loads, and it has become the subject of many studies of wind farm flows (Archer et al., 2018; Barthelmie & Jensen, 2010; Porté-Agel et al., 2020). Active yaw control (AYC), or active wake steering, is a wake-interference mitigation strategy that draws increasing interest in the research community. In this strategy, the upwind wind turbines are intentionally yawed to deflect their wakes away from downwind turbines. With a proper yawed configuration, the reduced power outputs in the yawed upwind turbines can be compensated by the increased power outputs in the downwind turbines. Therefore, a net power gain in the entire wind farm can be achieved.

Various early studies (Grant & Parkin, 2000; Grant et al., 1997) have revealed that the characteristics of the wake of a yawed turbine are significantly different from its non-yawed counterpart. Most notably, the yawed wake is deflected to the downwind-inclined side of the rotor. Medici and Alfredsson (2006) indicated the potential of exploiting this phenomenon to optimise wind farm power using active yaw control, and he validated this concept with wind tunnel experiments. Since then, there has been a push in the wind energy community towards understanding the wake characteristics of yawed turbines. Jiménez et al. (2010) first derived an analytical wake model based on the top-hat velocity profile as an extension to the well-known Jensen wake model (Jensen, 1983) for non-yawed turbines. Bastankhah and Porté-Agel (2016) performed a wind tunnel study of a yawed miniature wind turbine in a turbulent boundary layer flow. They found that the time-averaged velocity deficit and wake skew angle profiles are Gaussian and self-similar in the far wake region. Exploiting this phenomenon, they developed a closed-form analytical model for the velocity deficit profiles of yawed turbines. Comparing with the top-hat Jimenez model, they found that the Gaussian model results are in better agreement with the measurements. Zong and Porté-Agel (2020a) developed a momentum-conserving method to superpose the wake velocity deficits behind multiple yawed turbines. Qian and Ishihara (2018) developed a bi-Gaussian parametric model for the turbulence intensity distribution in the wake of a yawed turbine. In a follow-up study, Qian and Ishihara (2021) also proposed a superposition model for predicting turbulence intensity in the wakes of multiple yawed turbines. The Qian and Ishihara model is based on the principle of the linear sum of squares of the added turbulence intensity, and it introduces a parametric correction for partial-wake scenarios.



Another distinctive feature of the wake of a yawed turbine is the formation of a counter-rotating vortex pair (CVP), which is induced by the lateral forces applied by the yawed turbine. Howland et al. (2016) conducted wind tunnel experiments on a yawed permeable disk in laminar inflows. They found that the permeable disk's wake is significantly asymmetrical, or "curled", in the spanwise direction. The presence of the CVP deforms the curled wake. Bastankhah and Porté-Agel (2016) also observed the CVP in the wind tunnel study of a yawed miniature wind turbine immersed in a turbulent boundary-layer flow. The curled wake pattern can sustain itself beyond the near-wake region and can still be observed at the location where a downwind turbine can be installed. Motivated by these experimental results, researchers made several efforts to incorporate the physics of the CVP in yawed wake modelling. Shapiro et al. (2018) treated the yawed turbine as a surface with an elliptic vorticity distribution and used lifting line theory to model the CVP formation. Based on the vorticity distribution proposed by Shapiro et al. (2018), Martínez-Tossas et al. (2019) developed a curled-wake model by solving the linearised Euler equations. King et al. (2021) derived an analytical approximation of the model of Martínez-Tossas et al. (2019) and formulated a reduced-order curled wake model that is computationally efficient. Zong and Porté-Agel (2020b) investigated the physics of the CVP in wind tunnel experiments and developed a point-vortex transportation model that reproduces the formation mechanism of the top-down asymmetric kidney-shaped wake behind a yawed turbine.

Besides experimental and theoretical approaches, numerical modelling is also popular among researchers studying AYC. Large-eddy simulation (LES), due to its relatively high fidelity, is widely used to investigate wind turbine wakes. In LES, the turbine-induced forces can be represented by three main models. Jiménez et al. (2010) first used a standard actuator disk model (ADM-std), which assumes a uniform distribution of the thrust force on the rotor disk, to parametrise the yawed turbine-induced forces in LES. The ADM-std was also adopted by other researchers studying the wakes of multiple turbines (Boersma et al., 2019; Munters & Meyers, 2018a; Stevens et al., 2018). As an improvement to the ADM-std, the blade element actuator disk model (ADM-BE), also referred to as the rotational actuator disk model (ADM-R), is proposed by Wu and Porté-Agel (2011) and Porté-Agel et al. (2011b), which uses the blade element theory to parametrise the non-uniform thrust and tangential forces on the turbine rotor in LES. The ADM-BE was later applied by Fleming et al. (2018) to study the large-scale trailing vortices in yawed wind turbine wakes. The actuator line model (ALM), proposed by Sørensen and Shen (2002), is also a widely used in LES studies of yawed turbines (Archer & Vassel-Be-Hagh, 2019; Fleming et al., 2016; Stevens et al., 2018; Wang et al., 2017). The ALM parametrises the rotor-induced forces on the line elements distributed along each blade. Unlike LES using the ADM, LES using the ALM can produce the tip vortices in the near wake region. However, LES using the ALM also requires higher temporal and spatial resolution than the ADM counterpart (Martinez-Tossas et al., 2017), thus consuming substantially more computational resources.

Lin and Porté-Agel (2019) have previously validated an LES framework using the ADM-BE to simulate the wake of a stand-alone wind turbine subjected to AYC. Since the ultimate goal of

AYC is to be applied to wind farms, it is natural to extend the validation to multiple turbines. This study compares LES results using different turbine parametrisations (ADM-std, ADM-BE and ALM) with wind tunnel measurements of a three-turbine array (Zong & Porté-Agel, 2021) in different turbine layouts and yawed configurations.

The rest of the chapter is structured as follows. Section 3.2 discusses the numerical configurations used in the simulations and the methodology for evaluating the power output. Section 3.3 presents the simulation results obtained from LES using different turbine parametrisations and compares them with wind tunnel measurements. Section 3.4 shows the conclusions drawn from the results and discusses the possible extension of this work.

## 3.2 Methodology

### 3.2.1 Governing equations

A GPU-accelerated version of the WiRE-LES code is used in this study. The code has been developed at the Wind Engineering and Renewable Energy Laboratory (WiRE) of the École Polytechnique Fédérale de Lausanne (EPFL). It has been used and validated in previous studies of wind turbine wakes, e.g., in Wu and Porté-Agel (2011), Porté-Agel et al. (2011a), Abkar and Porté-Agel (2015) and Lin and Porté-Agel (2019).

The WiRE-LES solves the spatially filtered incompressible Navier-Stokes (N-S) equations:

$$\begin{aligned} \frac{\partial \tilde{u}_i}{\partial x_i} &= 0, \\ \frac{\partial \tilde{u}_i}{\partial t} + \tilde{u}_j \left( \frac{\partial \tilde{u}_i}{\partial x_j} - \frac{\partial \tilde{u}_j}{\partial x_i} \right) &= -\frac{\partial \tilde{p}^*}{\partial x_i} - \frac{\partial \tau_{ij}}{\partial x_j} - \frac{f_i}{\rho} + \frac{F_p}{\rho} \delta_{i1}, \end{aligned} \quad (3.1)$$

in which  $\tilde{u}_i$  is the spatially filtered velocity ( $i = 1, 2, 3$  representing the streamwise, spanwise and vertical directions, respectively);  $\tilde{p}^*$  is the modified kinematic pressure;  $f_i$  are the body forces exerted by the wind turbine on the flow;  $F_p$  is the pressure gradient imposed to drive the flow;  $\tau_{ij} = \widetilde{u_i u_j} - \tilde{u}_i \tilde{u}_j$  is the kinematic sub-grid scale (SGS) stress, which is parametrised using the modulated gradient model (MGM) proposed by Lu and Porté-Agel (2010):

$$\tau_{ij} = 2k_{sgs} \left( \frac{\tilde{G}_{ij}}{\tilde{G}_{kk}} \right), \quad (3.2)$$

in which  $\tilde{G}_{ij}$  is defined as follow:

$$\tilde{G}_{ij} = \frac{\tilde{\Delta}_x^2}{12} \frac{\partial \tilde{u}_i}{\partial x} \frac{\partial \tilde{u}_j}{\partial x} + \frac{\tilde{\Delta}_y^2}{12} \frac{\partial \tilde{u}_i}{\partial y} \frac{\partial \tilde{u}_j}{\partial y} + \frac{\tilde{\Delta}_z^2}{12} \frac{\partial \tilde{u}_i}{\partial z} \frac{\partial \tilde{u}_j}{\partial z}, \quad (3.3)$$

$k_{sgs}$  is the zero-clipped SGS kinetic energy:

$$k_{sgs} = \mathbf{1}_{\tilde{G}_{ij}\tilde{S}_{ij} < 0} (\tilde{G}_{ij}\tilde{S}_{ij}) \frac{4\tilde{\Delta}^2}{C_\epsilon^2} \left( -\frac{\tilde{G}_{ij}}{\tilde{G}_{kk}} \tilde{S}_{ij} \right)^2, \quad (3.4)$$

in which  $\mathbf{1}_{\tilde{G}_{ij}\tilde{S}_{ij} < 0}(\tilde{G}_{ij}\tilde{S}_{ij})$  is an indicator function taking the value of 1 if  $\tilde{G}_{ij}\tilde{S}_{ij} < 0$  and 0 if  $\tilde{G}_{ij}\tilde{S}_{ij} \geq 0$ ;  $\tilde{S}_{ij}$  is the filtered strain rate;  $\tilde{\Delta}$  is defined as  $\sqrt[3]{\tilde{\Delta}_x\tilde{\Delta}_y\tilde{\Delta}_z}$ , in which  $\tilde{\Delta}_x$ ,  $\tilde{\Delta}_y$  and  $\tilde{\Delta}_z$  are the filter widths in the streamwise, spanwise and vertical directions.  $C_\epsilon = 1.6$  is the model coefficient obtained from the simulations of the ABL flow using dynamic procedures (Lu & Porté-Agel, 2014).

### 3.2.2 Wind turbine parametrisation

In the WiRE-LES, three types of wind turbine parametrisation are implemented (Figure 3.1): the ADM-std, the ADM-BE and the ALM. In the ADM-std, a wind turbine is modelled as a permeable disk with thrust forces uniformly distributed within the rotor diameter. The magnitude of the thrust force is computed as follows:

$$F_x = \frac{1}{2} \rho A C_T U_{in}^2, \quad (3.5)$$

in which  $\rho$  is the air density;  $A$  is the sweeping area of the rotor disk;  $C_T$  is the thrust coefficient of the wind turbine, and  $U_{in}$  is the incoming wind speed. Since the turbines in wind farms often operate in the wakes of upwind turbines, their incoming velocities are retrieved as follows:

$$U_{in} = U_{loc} / (1 - a), \quad (3.6)$$

in which  $U_{loc}$  is the local disk-averaged velocity at the rotor, and  $a$  is the induction factor estimated from the thrust coefficient:

$$a = \frac{1}{2} (1 - \sqrt{1 - C_T}). \quad (3.7)$$

Using the reconstructed inflow velocity, we update the thrust coefficient and the power coefficient of the turbine by interpolating the thrust and power curves of the WiRE-01 miniature wind turbine (Bastankhah & Porté-Agel, 2016).

In the ADM-BE, the turbine-induced forces are parametrised using the blade element theory. In contrast with the ADM-std, the forces in the ADM-BE are computed from the local velocity information and the aerodynamic properties of each blade element. As a result, the forces are non-uniform across the rotor. Furthermore, the ADM-BE considers the thrust forces and models the tangential forces on the rotor. As a result, the ADM-BE introduces wake rotation in the wake of a turbine. After subdividing the rotor into an axisymmetric grid, the ADM-BE

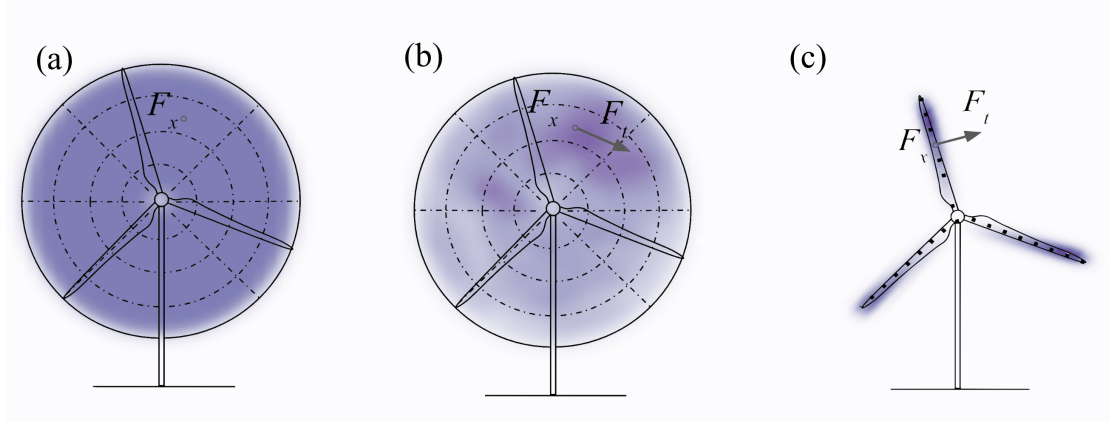


Figure 3.1: Schematic representation of the three wind turbine parametrisations used in WiRE-LES: (a) the ADM-std; (b) the ADM-BE; (c) the ALM. To illustrate the differences in the distribution of the forces computed using the three models, the normalised contours of the instantaneous force distribution (normalised by the respective maximum value) induced by each model are plotted.

computes the local thrust force  $F_x$  and the local tangential force  $F_t$  as follows:

$$\begin{aligned} F_x &= \frac{1}{2} \rho U_{ref}^2 \sigma \Phi (C_L \cos(\phi) + C_D \sin(\phi)), \\ F_t &= \frac{1}{2} \rho U_{ref}^2 \sigma \Phi (C_D \cos(\phi) - C_L \sin(\phi)), \end{aligned} \quad (3.8)$$

in which  $U_{ref}$  is the resultant inflow velocity at a given blade section;  $c$  is the chord length, and  $\sigma$  is the solidity of the blade section;  $\Phi$  is the Prantl tip-loss correction factor;  $\phi$  is the angle between the relative axial and the tangential velocity components at the blade element;  $C_L$  and  $C_D$  are the lift and drag coefficients interpolated from a 2D tabular dataset (Revaz et al., 2020) using the angle of attack (AoA) at a given blade element. A more detailed description of the ADM-BE and its application in yawed turbines can be found in Wu and Porté-Agel (2011) and Lin and Porté-Agel (2019).

The ALM computes the turbine-induced forces on line elements distributed on the moving turbine blades. The normal and the tangential forces on each source point are also computed from the blade element theory:

$$\begin{aligned} F_x &= \frac{1}{2} \rho U_{ref}^2 c \Phi (C_L \cos(\phi) + C_D \sin(\phi)), \\ F_t &= \frac{1}{2} \rho U_{ref}^2 c \Phi (C_D \cos(\phi) - C_L \sin(\phi)). \end{aligned} \quad (3.9)$$

### 3.2.3 Case configuration

In this study, four simulation cases are set up to reproduce the boundary-layer wind tunnel experiments of a wind turbine array subjected to active yaw control described by Zong and Porté-Agel (2021). The wind turbine array consists of three WiRE-01 miniature wind turbines. The diameter of the turbine  $d = 0.15$  m, and the hub height  $Z_{hub} = 0.125$  m. Each turbine is separated from the closest neighbouring turbines by a constant distance  $S_x = 5d$  in the streamwise direction.

The configurations of the cases are summarised in Table 3.1. In Cases 1 and 2, the turbine rotor locations are aligned in the streamwise direction (i.e., lateral offset  $S_y = 0$ ), while a lateral offset  $S_y = d/3$  is applied in Cases 3 and 4. In Cases 1 and 3, no active yaw control is applied (i.e., zero yaw angle for all turbines), while yawing configurations of  $(-25^\circ, -15^\circ, 0^\circ)$  and  $(-20^\circ, -20^\circ, 0^\circ)$  are applied in Cases 2 and 4, respectively. These were found to be the optimal yawing strategies that maximised the overall power output from the experiments (Zong & Porté-Agel, 2021)<sup>1</sup>. The wind turbine rotational speeds  $\omega$  are also chosen to match those of the experiments.

Table 3.1: Case configurations of the wind tunnel experiments, with the specifications of the lateral offset  $S_y$ , the yaw angles  $\gamma = (\gamma_1, \gamma_2, \gamma_3)$  and the rotational speeds  $\omega = (\omega_1, \omega_2, \omega_3)$ .

No.	$S_y$	$\gamma$	$\omega$ (RPM)
Case 1	0	$(0^\circ, 0^\circ, 0^\circ)$	(2183, 1405, 1560)
Case 2	0	$(-25^\circ, -15^\circ, 0^\circ)$	(2113, 1666, 1744)
Case 3	$d/3$	$(0^\circ, 0^\circ, 0^\circ)$	(2156, 1639, 1755)
Case 4	$d/3$	$(-20^\circ, -20^\circ, 0^\circ)$	(2094, 1824, 2072)

Schematics of the simulation domain are shown in Figure 3.2. The size of the domain in the streamwise direction is  $21.3d$ . To minimise the blockage effect, the size of the simulation domain is  $10.7d$  in the spanwise direction and  $5.3d$  in the vertical direction. The pressure gradient is imposed up to the height  $Z_{bl} = 0.3$  m to create a boundary layer with the same height as in the experiments. The friction velocity  $u_* = 0.265$  m s<sup>-1</sup> and the roughness length  $z_0 = 9 \times 10^{-5}$  m in the LES cases are chosen so that the streamwise mean inflow velocity and the streamwise turbulence intensity at the hub-height match the wind tunnel measurements (Figure 3.3).

### 3.2.4 Numerical configuration

In the WiRE-LES, the spatially filtered N-S equations are solved by the pseudospectral method in the horizontal directions and the second-order finite-difference method in the vertical direction. Explicit time integration is carried out using the Adams–Bashforth method. Such a choice of numerical schemes has also been applied and validated in previous wind turbine

<sup>1</sup>For the sake of consistency with other chapters, the definition of positive yaw direction in this chapter is opposite to the one in Zong and Porté-Agel (2021): for a counter-clockwise rotating turbine (when viewed from the front), the yaw angle is positive when the turbine is yawed clockwise (when viewed from the top).

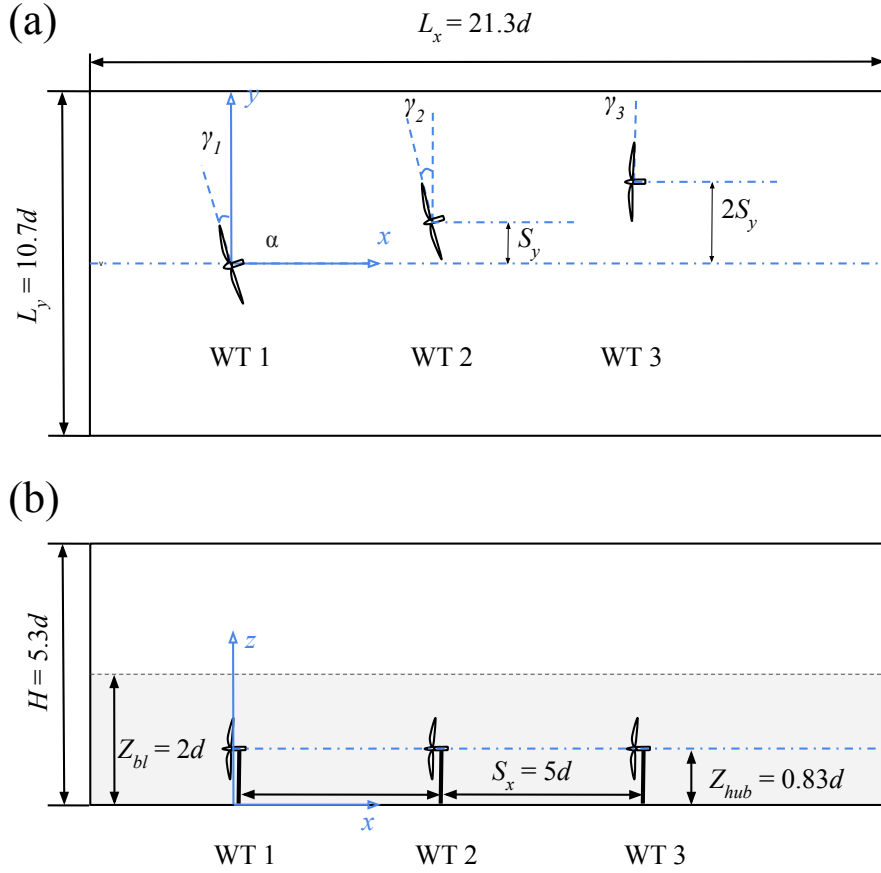


Figure 3.2: Schematic plots of the simulation domain (not to scale): (a) top view; (b) side view.

wake flow studies (Lin & Porté-Agel, 2019; Wu & Porté-Agel, 2011).

The simulation domain is discretised into a uniform grid with the cell numbers of  $256 \times 128 \times 128$  in the streamwise, spanwise and vertical directions, respectively. Since the 3/2 rule is applied in the spectral filter in the horizontal directions for the de-aliasing, the ratio between the filter size  $\tilde{\Delta}$  and the grid size ( $\Delta$ ) in the horizontal directions is  $\tilde{\Delta}_x/\Delta_x = \tilde{\Delta}_y/\Delta_y = 1.5$ . In the vertical direction, the ratio is  $\tilde{\Delta}_z/\Delta_z = 1$ . Therefore, the aspect ratio of the grid is  $\Delta_x : \Delta_y : \Delta_z = 2 : 2 : 1$  and the aspect ratio of the filter is  $\tilde{\Delta}_x : \tilde{\Delta}_y : \tilde{\Delta}_z = 3 : 3 : 1$ . In the spanwise direction, the ratio of the rotor diameter to the filter size is  $d/\tilde{\Delta}_y = 8$ , and the ratio to the grid size is  $d/\Delta_y = 12$ . In the vertical direction, the ratios of the rotor diameter to the filter size and the grid size are  $d/\Delta_z = d/\tilde{\Delta}_z = 24$ . The time step is chosen to keep the Courant number around 0.1. The total simulated physical time is 15 minutes, and the last 10 minutes of the simulation are used to obtain flow statistics and power outputs.

Periodic boundary conditions are used on the lateral boundaries in the horizontal directions ( $x$  and  $y$ ). In the vertical direction ( $z$ ), a slip-wall condition is imposed on the top boundary, and a non-penetration wall is applied on the bottom boundary with specified stress based on the logarithmic law of the wall. A precursor method is used to generate the turbulent inflow

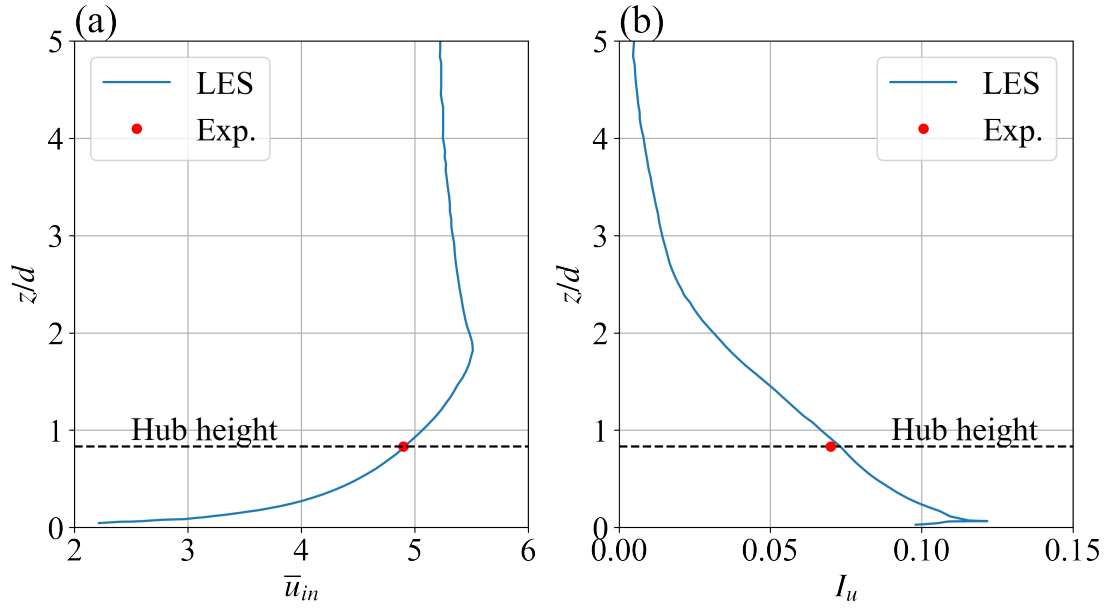


Figure 3.3: Vertical profiles of the inflow streamwise mean velocity  $\bar{u}_{in}$  (m/s) (a) and the streamwise turbulence intensity  $I_u$  (b). Blue solid lines represent the LES results, and red dots represent the corresponding measurement data at the hub height.

for the simulation (Abkar & Porté-Agel, 2015; Porté-Agel et al., 2013; Wu & Porté-Agel, 2011), and a shifting boundary method is applied (Munters et al., 2016) at the inflow to mitigate the formation of spurious locked-in streak-like structure (Fang & Porté-Agel, 2015).

### 3.3 Results

#### 3.3.1 Mean velocity

For the cases with zero lateral offset (Cases 1 and 2), contours of the normalised streamwise mean velocity in the  $x$ - $y$  plane at hub height are shown in Figures 3.4 and 3.5, respectively. In Case 1 (Figure 3.4), the turbines are not yawed, and the turbine array is aligned with the inflow direction. The second and the third turbines are fully exposed to the wakes of their upwind turbines. In Case 2 (Figure 3.5), with the yaw angles  $\gamma = (-25^\circ, -15^\circ, 0^\circ)$ , the wakes of the yawed turbines are redirected to the side where the turbine rotor plane is inclined into the downwind direction. As a result, the second and the third turbines in Case 2 are partially exposed to the wake of their respective upwind turbines.

Spanwise profiles of the normalised streamwise mean velocity at hub height in Cases 1 and 2 are shown in Figures 3.6 and 3.7, respectively. Behind the first turbine, we find that the maximum velocity deficits are slightly underestimated by LES using the ADM-std in the near wake for both non-yawed (Figure 3.6a) and yawed configurations (Figure 3.7a). As the wake develops further downstream, the results of the three models converge to the measurements.

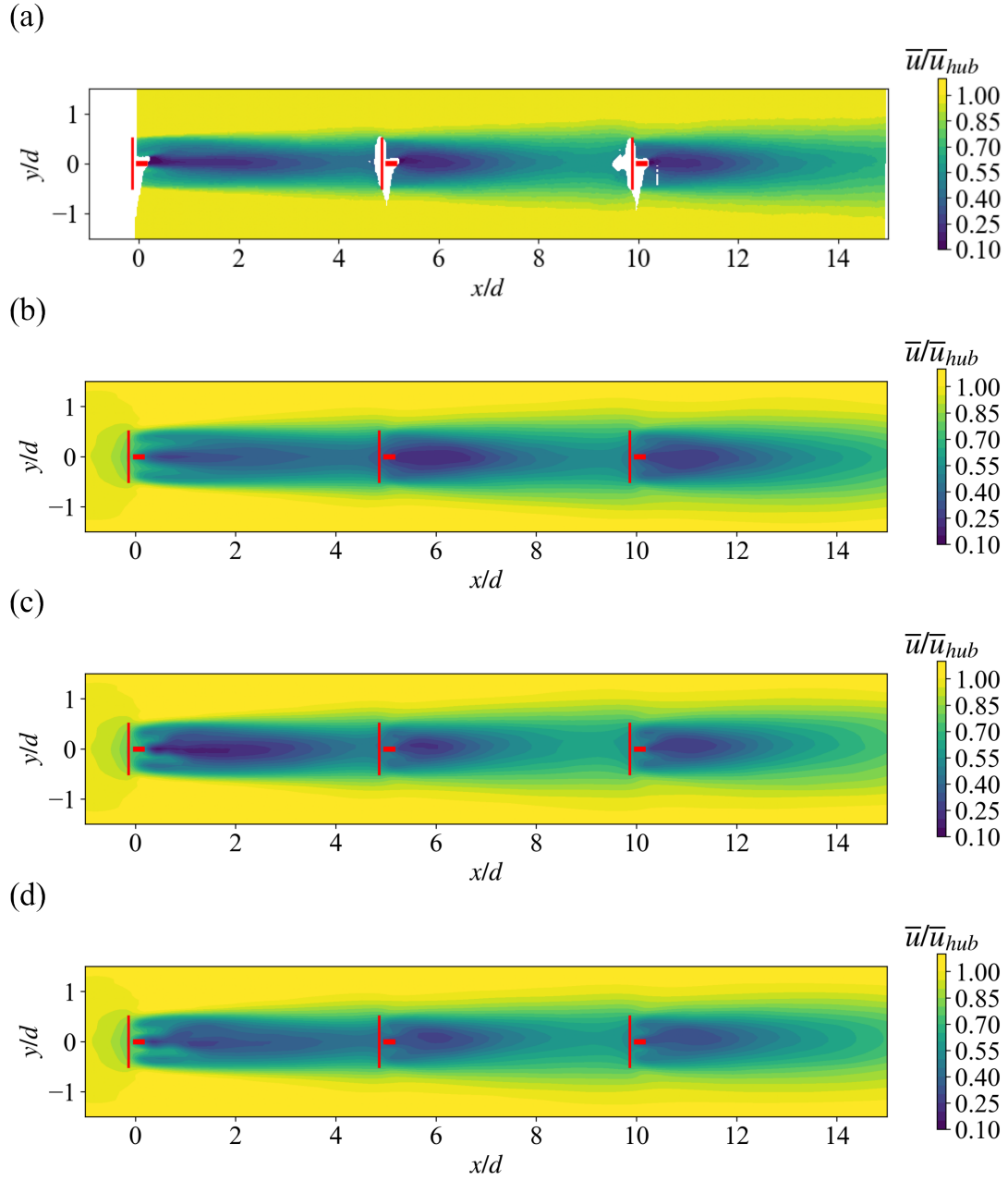


Figure 3.4: Contours of the normalised streamwise mean velocity  $\bar{u}/\bar{u}_{hub}$  in the  $x$ - $y$  plane at hub height obtained from the wind-tunnel experiments and LES in Cases 1. (a) Experiment; (b) ADM-std; (c) ADM-BE; (d) ALM.



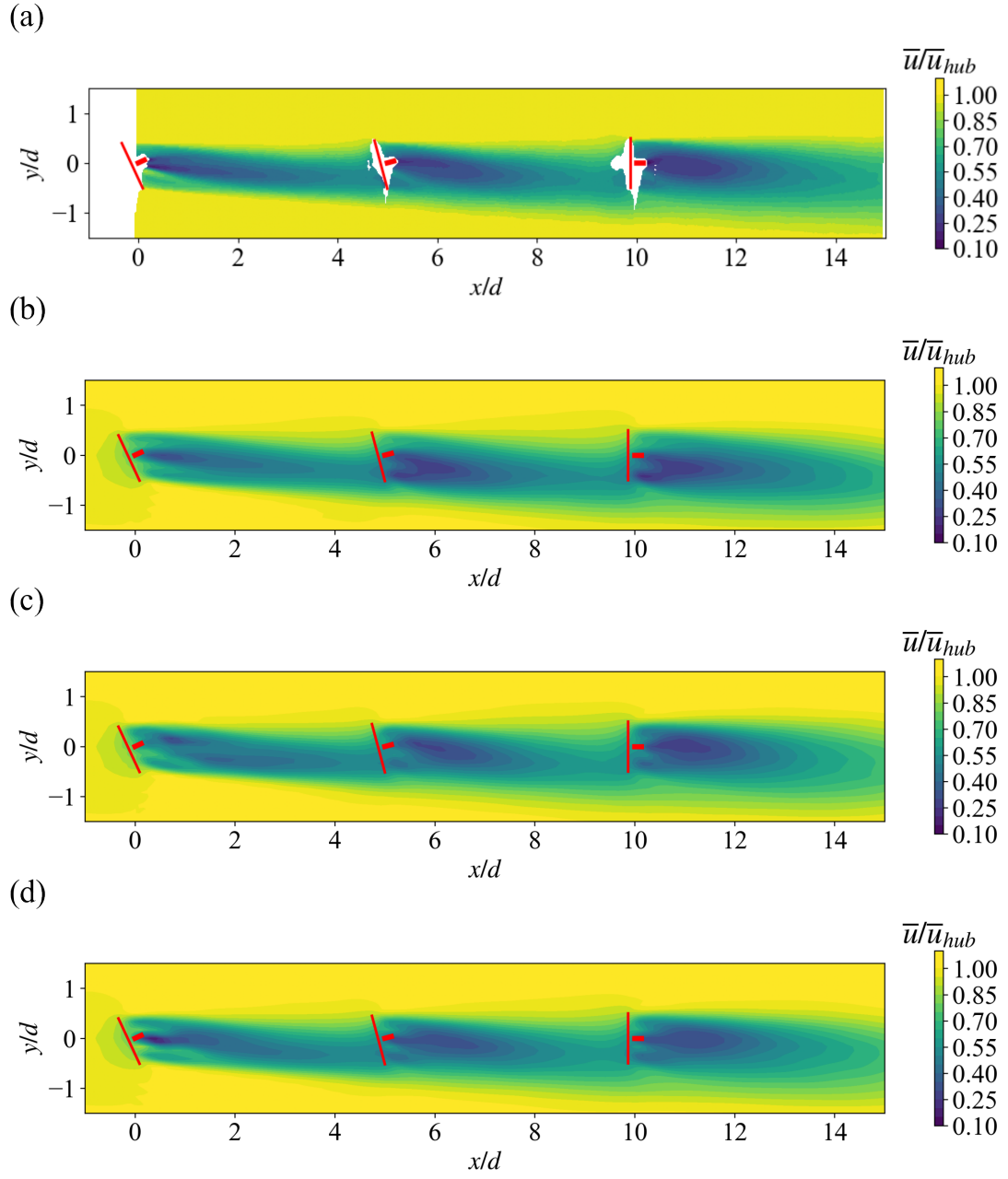


Figure 3.5: Contours of the normalised streamwise mean velocity  $\bar{u}/\bar{u}_{hub}$  in the  $x$ - $y$  plane at hub height obtained from the wind-tunnel experiments and LES in Cases 2. (a) Experiment; (b) ADM-std; (c) ADM-BE; (d) ALM.

Behind the second turbine, the wakes of the turbine parametrised by the ADM-std have slightly larger velocity deficits and wake widths compared to the measurements in the non-yawed configuration (Figure 3.6b). In the yawed configuration (Figure 3.7b), the velocity deficits obtained from LES using the ADM-std are overestimated on the side where the turbine rotor is inclined downwind and are underestimated on the upwind-inclined side. As a result, the velocity profiles are further shifted to the negative spanwise ( $y$ ) direction than the measurements. Behind the third turbine, the three models yield reasonable predictions of the mean velocity in the non-yawed configuration (Figure 3.6c), while the ADM-std again produces an unrealistic shift in the velocity profiles in the yawed configuration (Figure 3.7c).

Figures 3.8 - 3.11 show measured and simulated contours and spanwise profiles of the mean velocity, respectively, for the partial-wake cases under consideration (Cases 3 and 4). Due to the lateral offset of the turbines, the second and the third turbines are partially exposed to the incoming wakes in the non-yawed and yawed configurations. In Cases 3 and 4, where the partial-wake condition occurs, shifted velocity profiles with respect to the measurements are observed in the wakes of the second and the third turbines parametrised by the ADM-std. Furthermore, an underestimation of the velocity deficits is also observed in the wake of the third turbine parametrised by the ADM-std in Case 4.

Figure 3.12 shows the trajectories of the location of the maximum velocity deficit in the wake in different configurations. The trajectories obtained from LES using the ADM-BE and the ALM are in good agreement with the measurements. On the other hand, the trajectories obtained from LES using the ADM-std are shifted from the measurements behind the turbines in partial wake conditions. This is consistent with the shifted pattern observed in the velocity profiles. This observation can be explained by a key model assumption of the ADM-std: the turbine-induced forces are modelled as thrust forces uniformly distributed on the rotor disk. To illustrate this point, we plot the time-averaged thrust forces per unit area on the rotor disk of WT 3 in Case 2, which is a turbine partially exposed to the wake of its upstream turbine (Figure 3.13). We can see that the normal thrust force parametrised by the ADM-std (Figure 3.13a) is uniform on the rotor. By contrast, the forces parametrised by the ADM-BE (Figure 3.13b) and the ALM (Figure 3.13c) have non-uniform distributions on the rotor: specifically, larger thrust forces are found on the right side of the contours. The differences in the thrust force distribution lead to a shift from the measurements in the maximum velocity deficit trajectories in the cases using the ADM-std.

#### 3.3.2 Turbulence statistics

Contours and profiles of the streamwise turbulence intensity in the  $x$ - $y$  plane at hub height are shown from Figures 3.14 to 3.17. The experiment results of the non-yawed and yawed configurations are compared with the corresponding LES results using the ADM-std, ADM-BE and ALM. Since the wind tunnel measurements of the turbulence intensity are not available for Case 3 and Case 4, we only analyse Case 1 and Case 2 without offset.

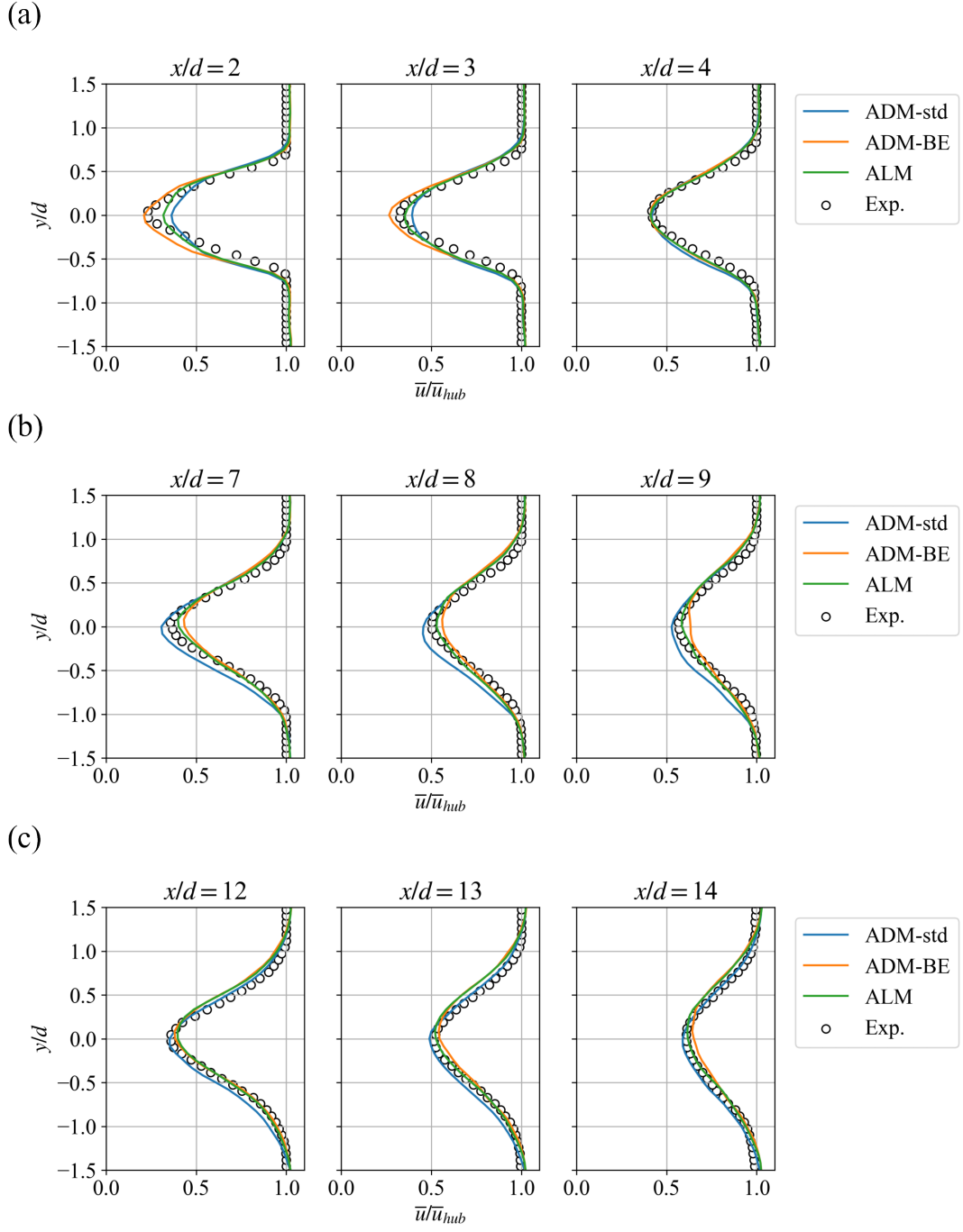


Figure 3.6: Spanwise profiles of the normalised streamwise mean velocity  $\bar{u}/\bar{u}_{hub}$  in the  $x$ - $y$  plane at hub height obtained from the wind-tunnel experiments and LES in Case 1. (a) WT 1; (b) WT 2; (c) WT 3.

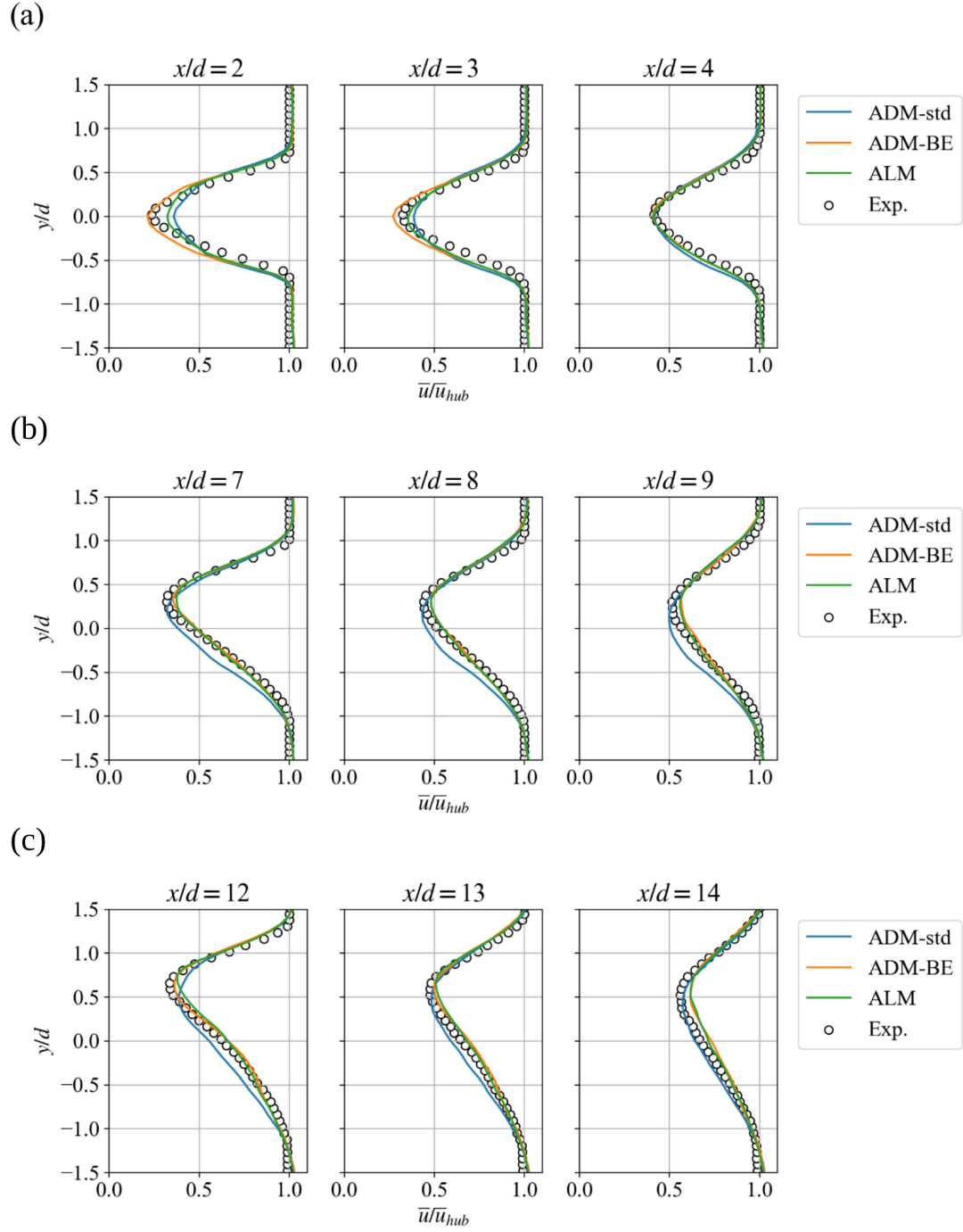


Figure 3.7: Spanwise profiles of the normalised streamwise mean velocity  $\bar{u}/\bar{u}_{hub}$  in the  $x$ - $y$  plane at hub height obtained from the wind-tunnel experiments and LES in Case 2. (a) WT 1; (b) WT 2; (c) WT 3.

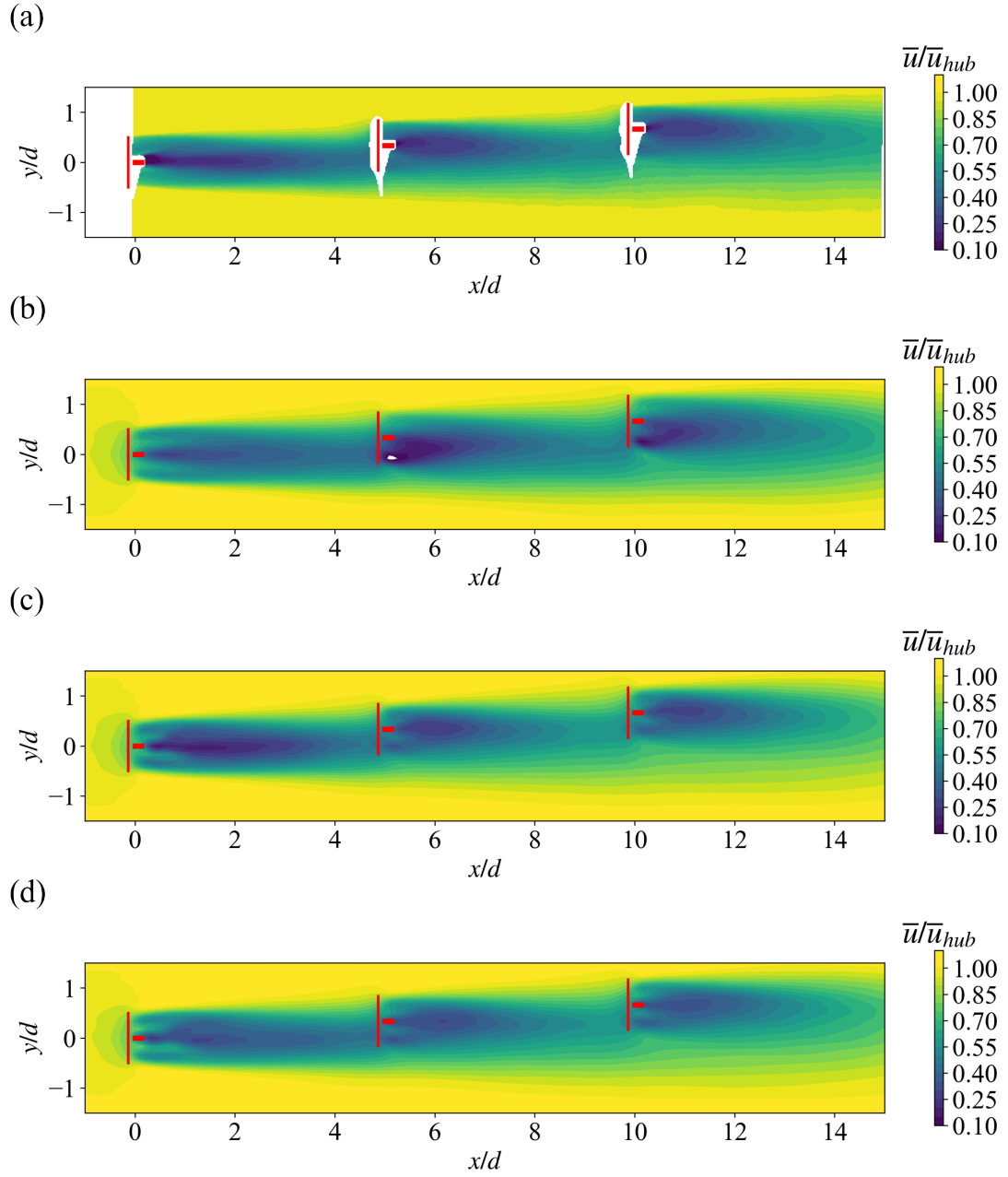


Figure 3.8: Contours of the normalised streamwise mean velocity  $\bar{u}/\bar{u}_{hub}$  in the  $x-y$  plane at hub height obtained from the wind-tunnel experiments and LES in Cases 3: (a) Experiment; (b) ADM-std; (c) ADM-BE; (d) ALM.

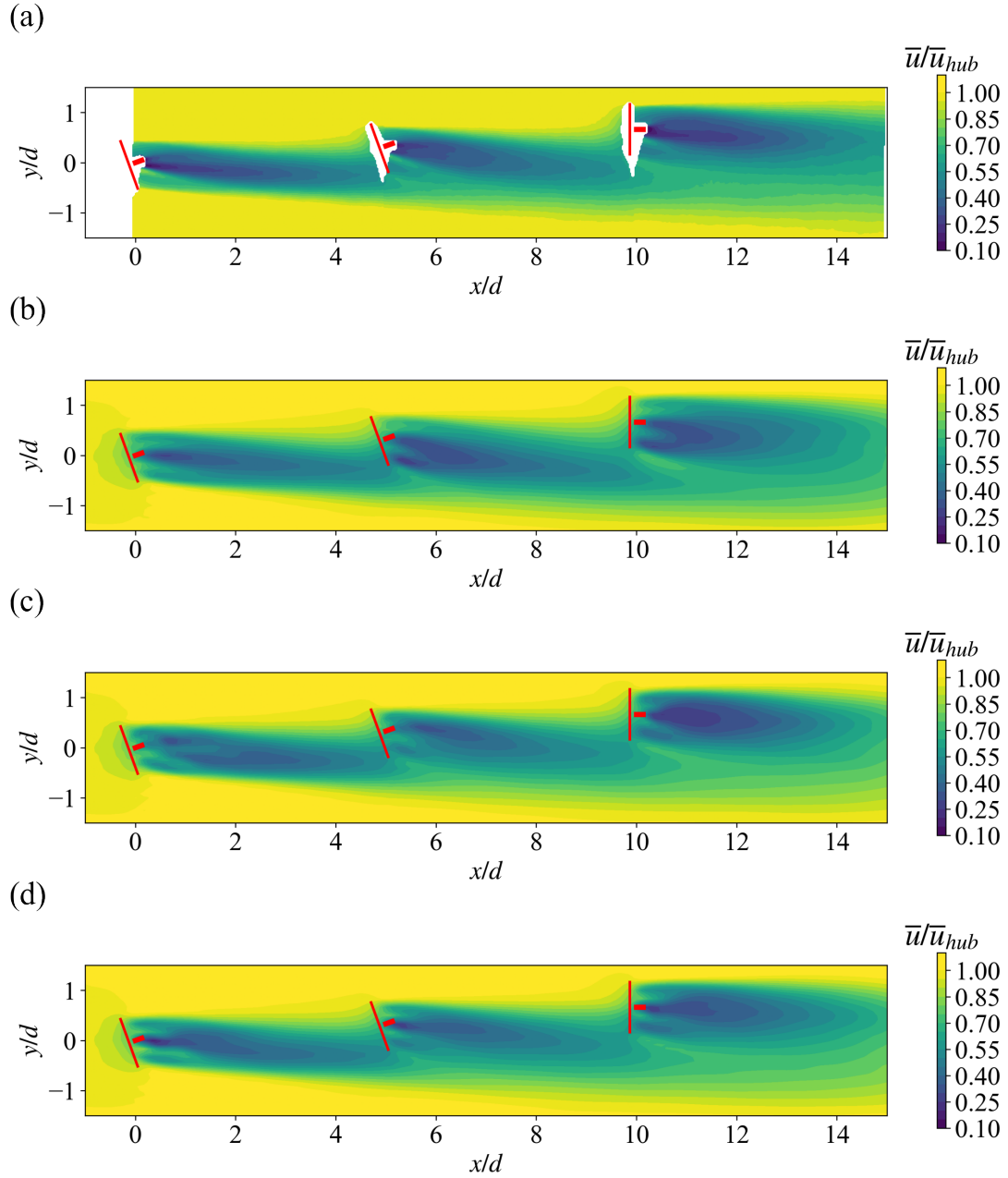


Figure 3.9: Contours of the normalised streamwise mean velocity  $\bar{u}/\bar{u}_{hub}$  in the  $x$ - $y$  plane at hub height obtained from the wind-tunnel experiments and LES in Cases 4: (a) Experiment; (b) ADM-std; (c) ADM-BE; (d) ALM.

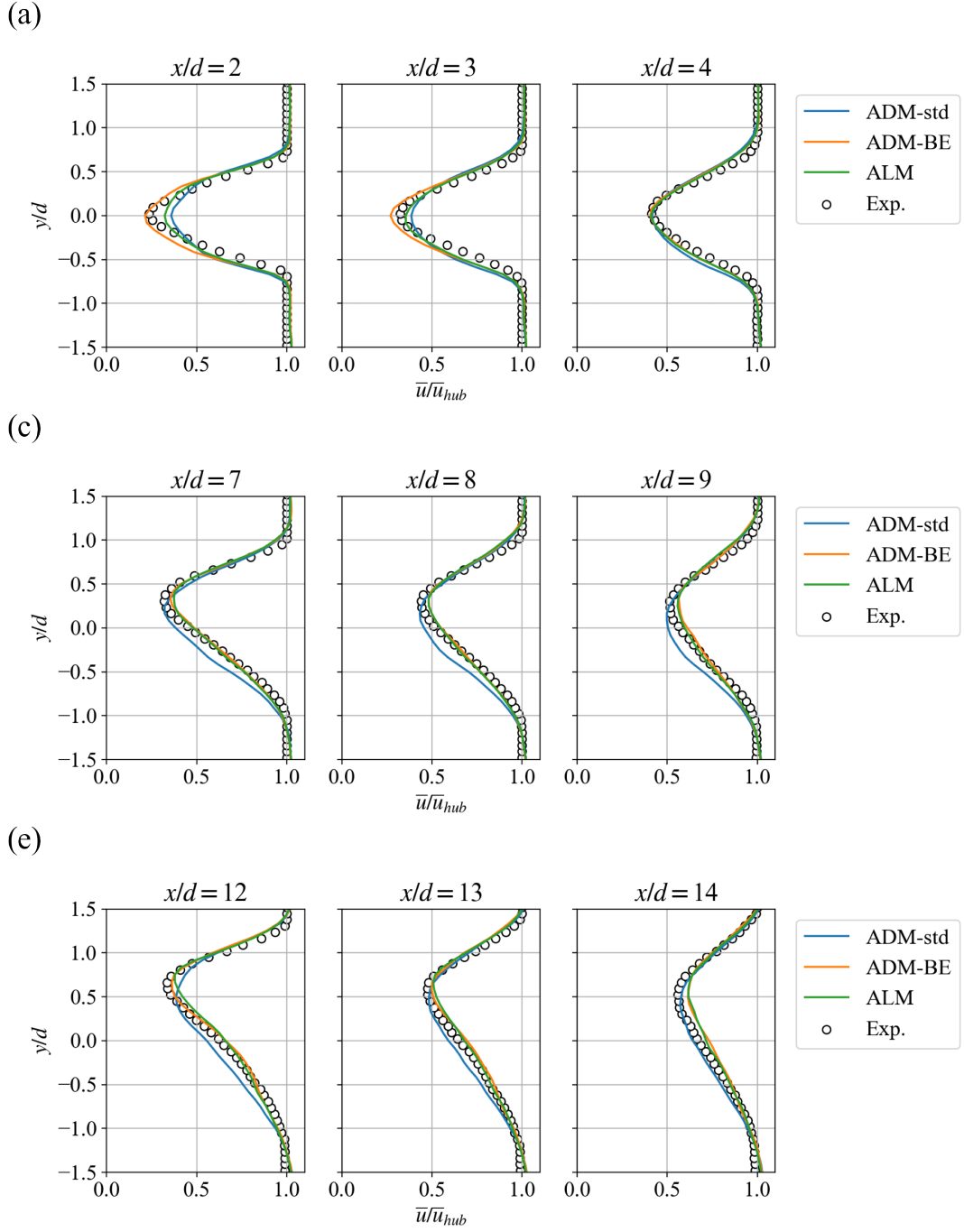
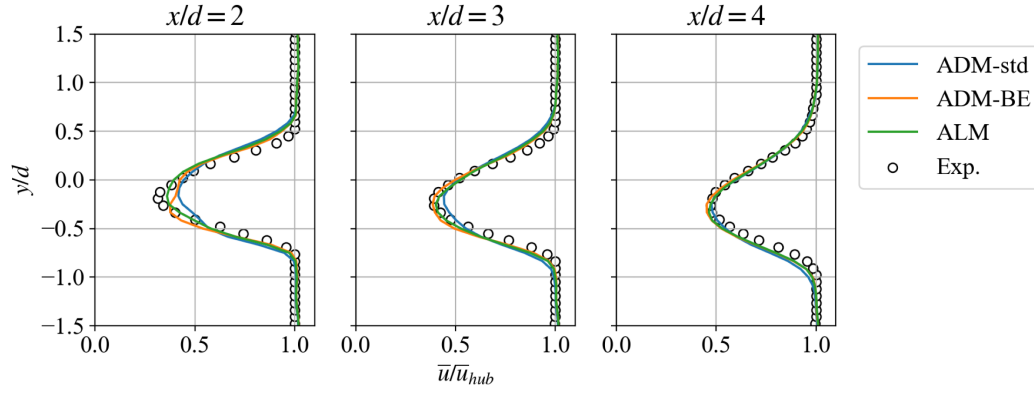
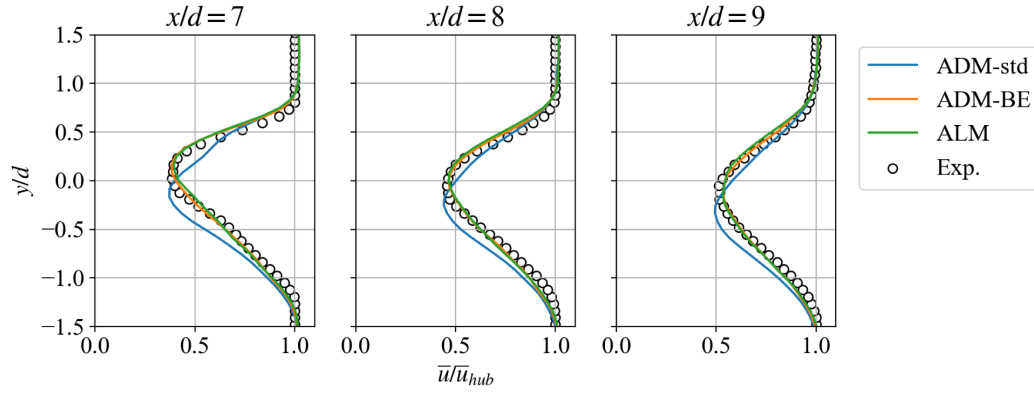


Figure 3.10: Spanwise profiles of the normalised streamwise mean velocity  $\bar{u}/\bar{u}_{hub}$  in the  $x$ - $y$  plane at hub height obtained from the wind-tunnel experiments and LES in Case 3. (a) WT 1; (b) WT 2; (c) WT 3.

(a)



(b)



(c)

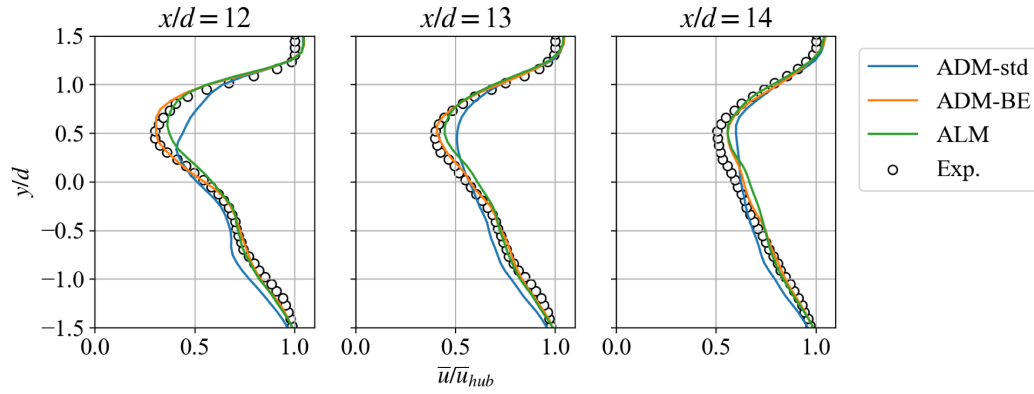


Figure 3.11: Spanwise profiles of the normalised streamwise mean velocity  $\bar{u}/\bar{u}_{hub}$  in the  $x$ - $y$  plane at hub height obtained from the wind-tunnel experiments and LES in Case 4. (a) WT 1; (b) WT 2; (c) WT 3.



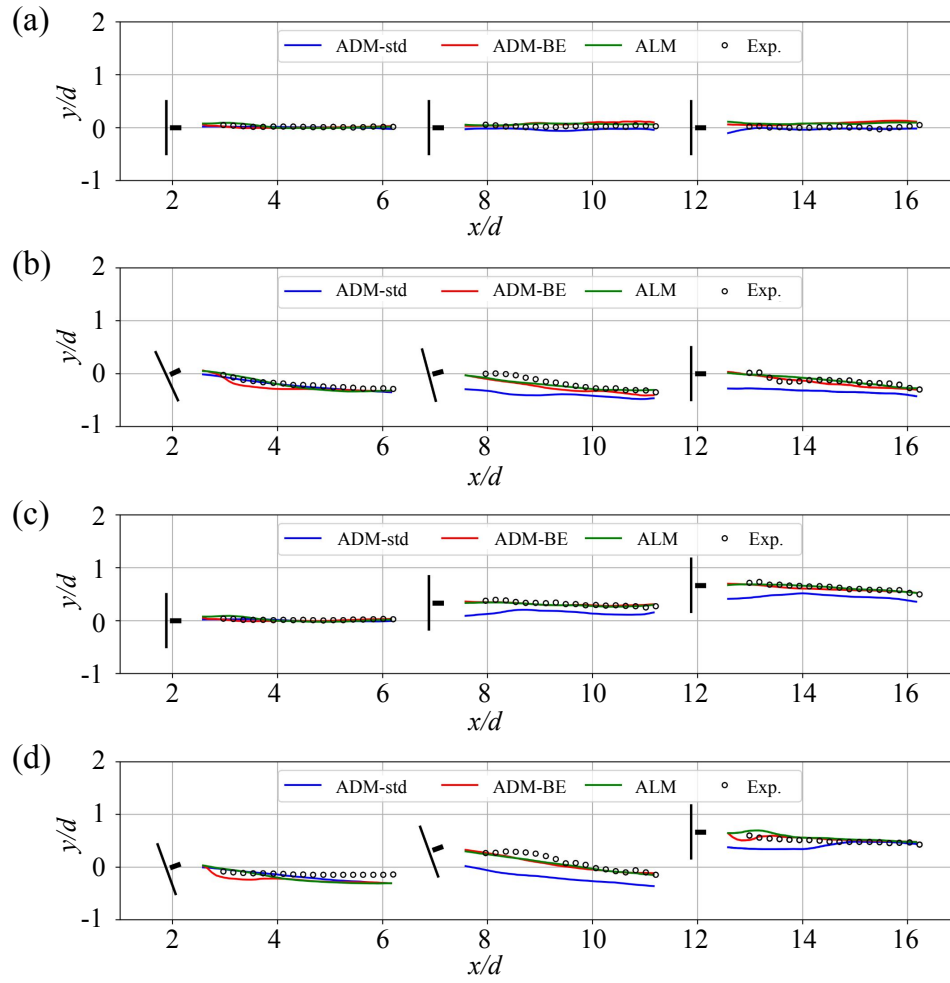


Figure 3.12: Trajectories of maximum velocity deficit location obtained from the wind-tunnel experiments, LES using the ADM-std, ADM-BE and ALM. (a) Case 1:  $\gamma = (0^\circ, 0^\circ, 0^\circ)$ , zero offset; (b) Case 2:  $\gamma = (-25^\circ, -15^\circ, 0^\circ)$ , zero offset; (c) Case 3:  $\gamma = (0^\circ, 0^\circ, 0^\circ)$ ,  $d/3$  offset; (d) Case 4:  $\gamma = (-20^\circ, -20^\circ, 0^\circ)$ ,  $d/3$  offset.

In the measurement contours shown in Figures 3.14 and 3.15, a large magnitude of turbulence intensity is observed at the edges of the wake due to the strong shear in these regions. In the non-yawed case (Figure 3.14a), the turbulence intensity in the wakes is largely symmetric with respect to the wake centre-line. In the yawed case (Figure 3.15a), the turbulence intensity on the positive  $y$  side of the wake is larger than the turbulence intensity on the negative  $y$  side.

By comparing the LES results with the measurements in the turbulence intensity contours, we find that the results of LES using the ADM-std show discrepancies with the measurements in the yawed case with the partial-wake condition. In the wakes behind the second and the third turbine, LES using the ADM-std overestimates the turbulence intensity with respect to the measurements on the negative  $y$  side of the wake. This is consistent with the overestimation of the mean velocity gradient in LES using the ADM-std on the positive  $y$  side of the skewed wake

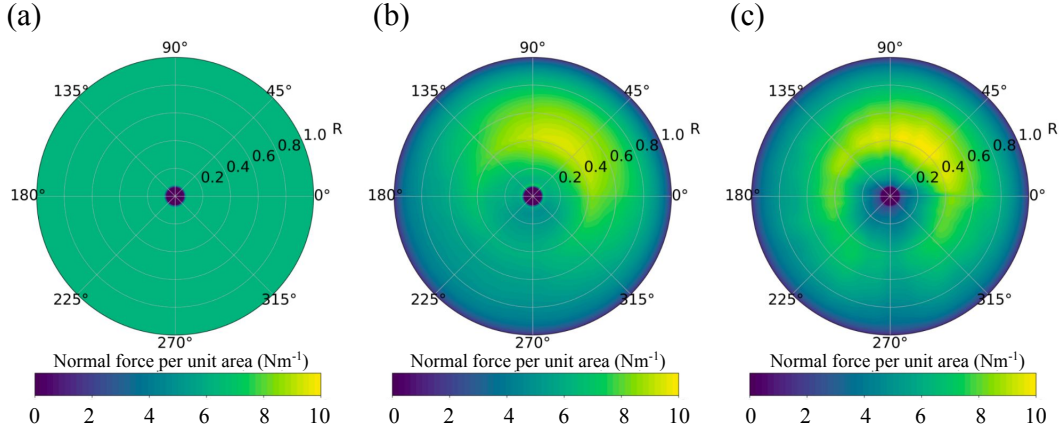


Figure 3.13: Back-view contours of the time-averaged normal force per unit area on the rotor disk of WT 3 in Case 2. The turbine forces are parametrised by (a) the ADM-std; (b) the ADM-BE; (c) the ALM.

(Figure 3.7). Furthermore, in comparison with LES using the ADM-BE and the ALM, we find that LES using the ADM-std underestimates the magnitude of the turbulence flux  $\overline{u'v'}$  on the positive  $y$  side of the wake (Figure 3.18) in the yawed case. Since the turbulence production term is defined by taking a product of the velocity gradient and the turbulence flux, such differences in LES using the ADM-std lead to an incorrect turbulence intensity distribution in the partial-wake scenario. Comparisons of the turbulence intensity profiles in Figures 3.16 and 3.17 also show that LES using the ADM-std, the ADM-BE and the ALM slightly overspread the turbulence in the wakes: the turbulence intensity profiles of the LES results are wider than the measurements in both non-yawed and yawed cases. This phenomenon is caused by the fact that the turbine forces in the LES are smeared by smoothing kernels in the turbine parametrisations. As a result, the shear layer produced at the wake's edges is wider than the measurements, causing the wider turbulence intensity profiles in the LES results.

### 3.3.3 Power prediction

Finally, we compare the power prediction obtained from LES using the ADM-std, the ADM-BE and the ALM with the power measured in the wind tunnel experiments performed by Zong and Porté-Agel (2021). Figure 3.19 shows the simulated power coefficients of a zero-yawed stand-alone turbine and their relative errors to the measurements. The power coefficients are obtained from the simulations using a baseline grid and a refined grid ( $\times 2$  refinement in  $x$ ,  $y$  and  $z$  directions from the baseline grid). We find that the ADM-BE yields the best predictions in the baseline and refined grid cases. Moreover, the errors in the predictions of the ADM-BE are within the measurement uncertainty ( $\pm 4.5\%$ ) in both cases. By contrast, in the baseline grid case, the power coefficients predicted by the ADM-std and the ALM have errors that are larger than the uncertainty upper bound. When the grid is refined, the error in the power

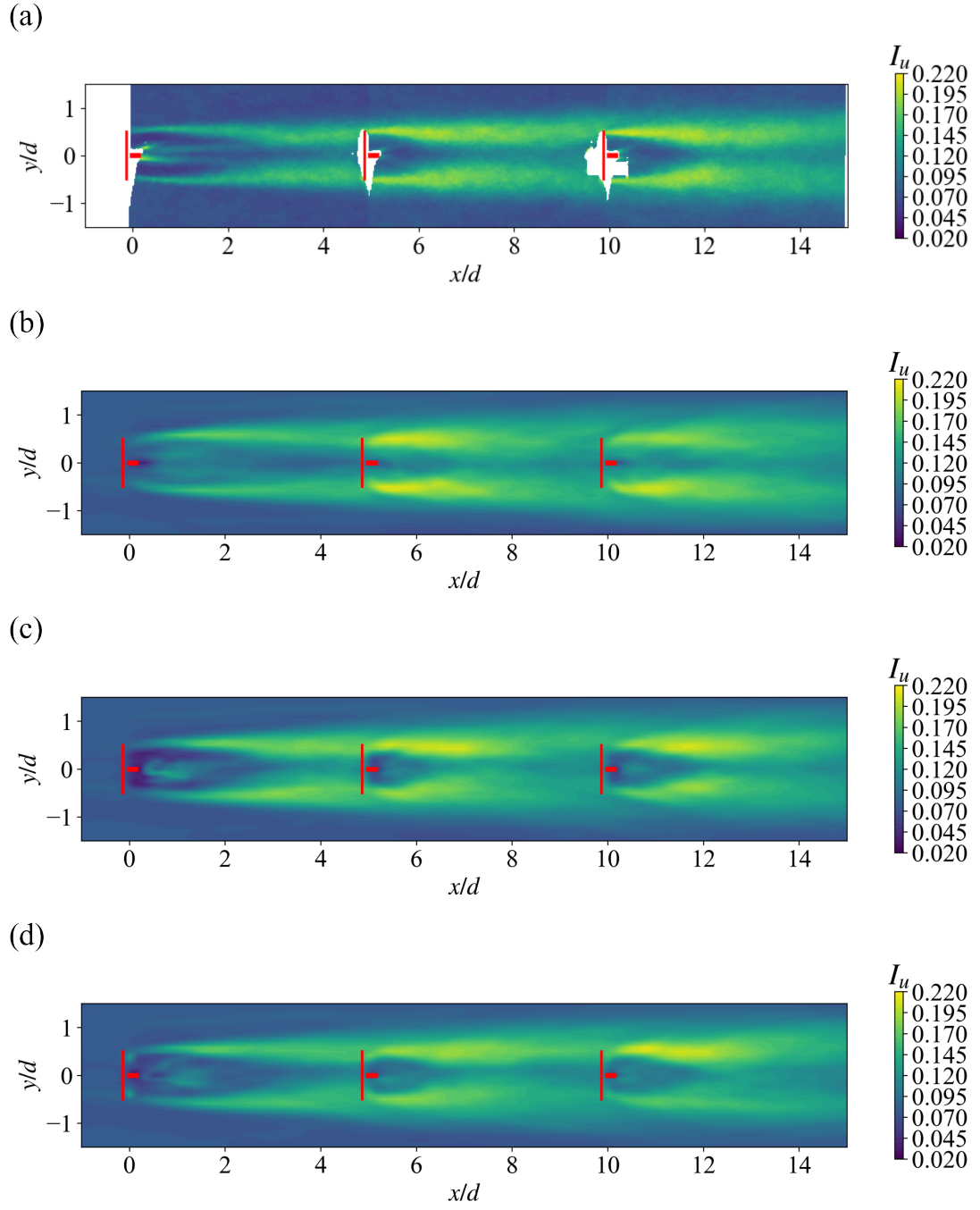


Figure 3.14: Contours of the turbulence intensity  $I_u$  in the  $x$ - $y$  plane at hub height obtained from the wind-tunnel experiments and LES in Case 1: (a) Experiment; (b) ADM-std; (c) ADM-BE; (d) ALM.

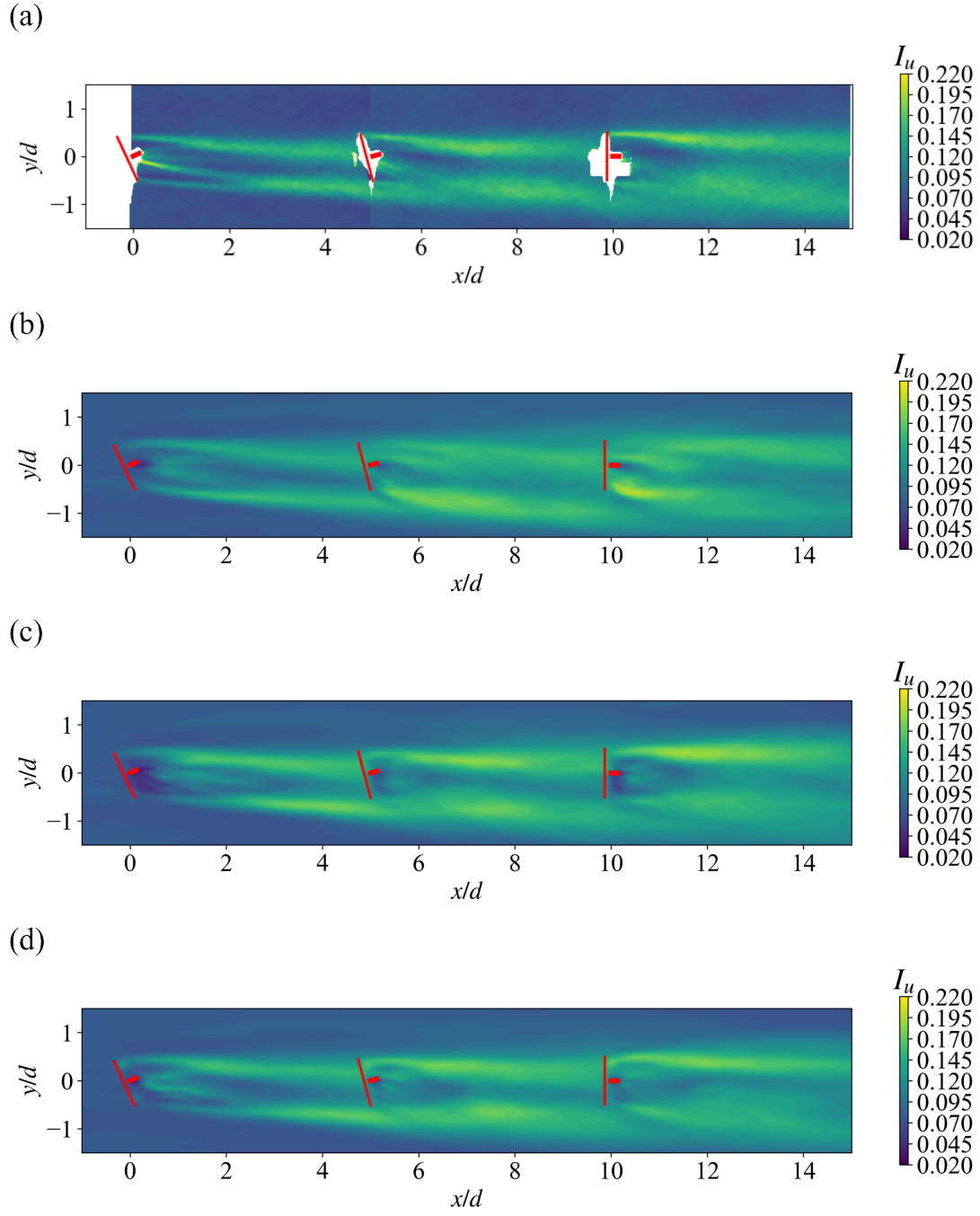


Figure 3.15: Contours of the turbulence intensity  $I_u$  in the  $x$ - $y$  plane at hub height obtained from the wind-tunnel experiments and LES in Case 2: (a) Experiment; (b) ADM-std; (c) ADM-BE; (d) ALM.

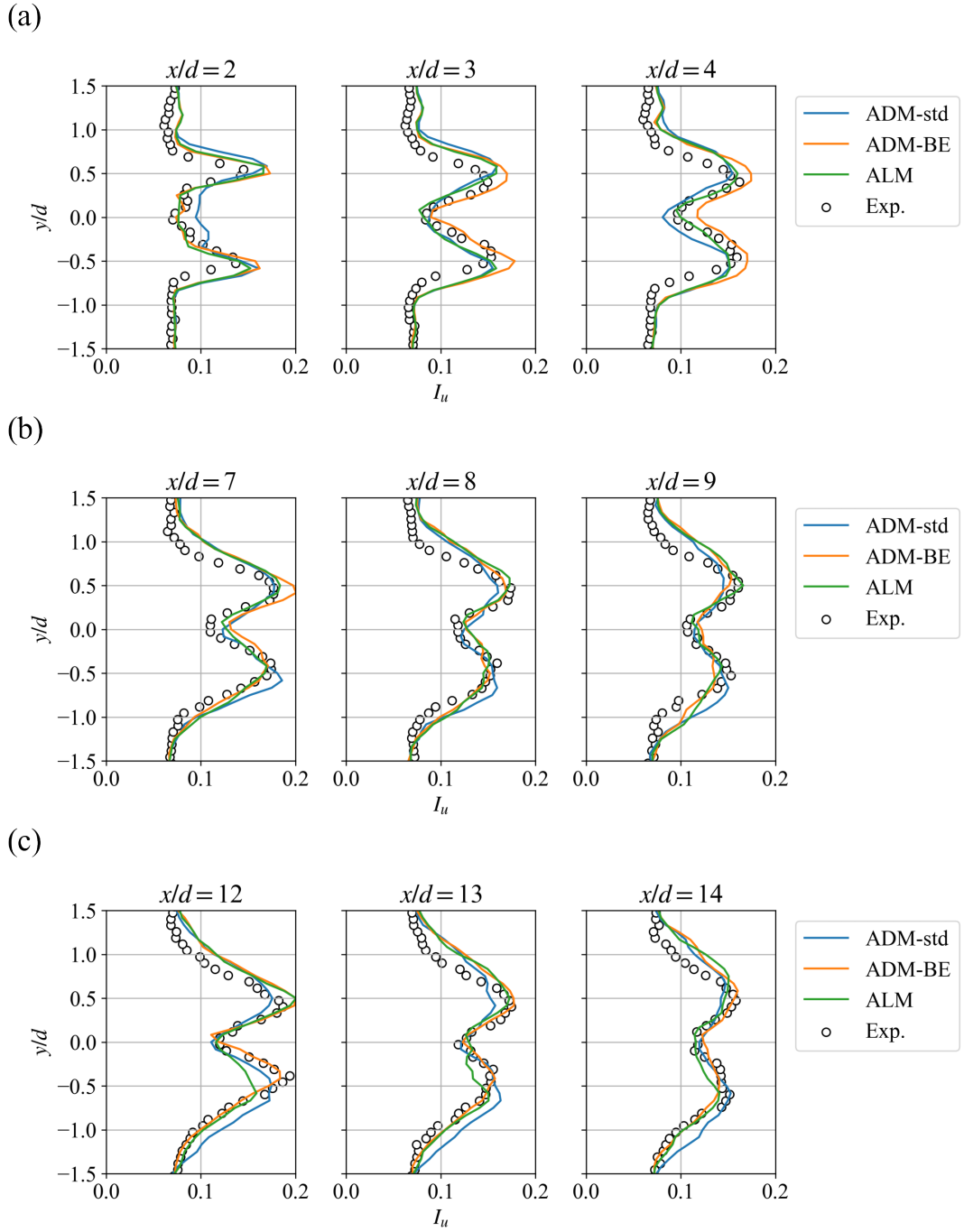


Figure 3.16: Spanwise profiles of the turbulence intensity  $I_u$  in the  $x$ - $y$  plane at hub height obtained from the wind-tunnel experiments and LES in Case 1. (a) WT 1; (b) WT 2; (c) WT 3.

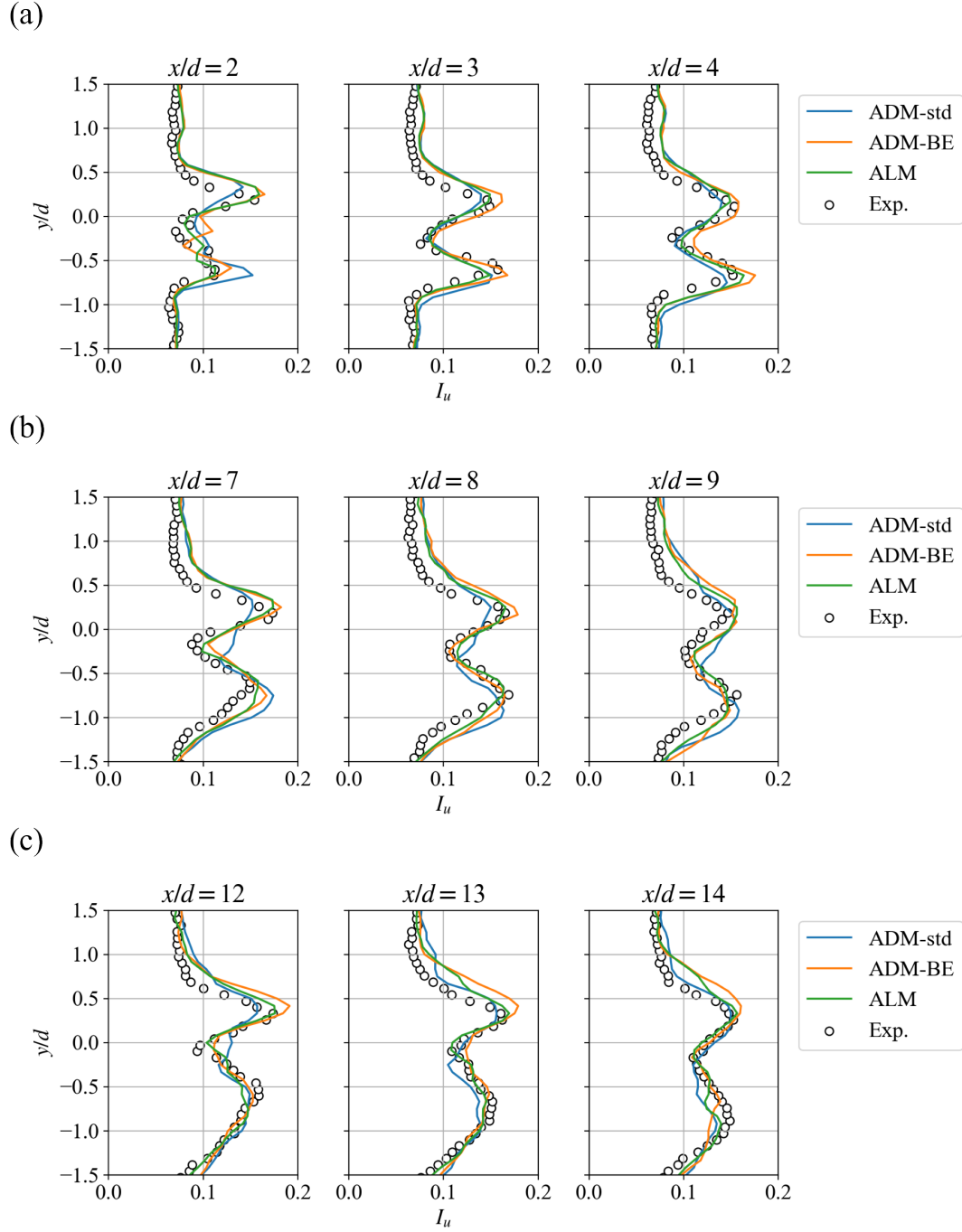


Figure 3.17: Spanwise profiles of the turbulence intensity  $I_u$  in the  $x$ - $y$  plane at hub height obtained from the wind-tunnel experiments and LES in Case 2. (a) WT 1; (b) WT 2; (c) WT 3.

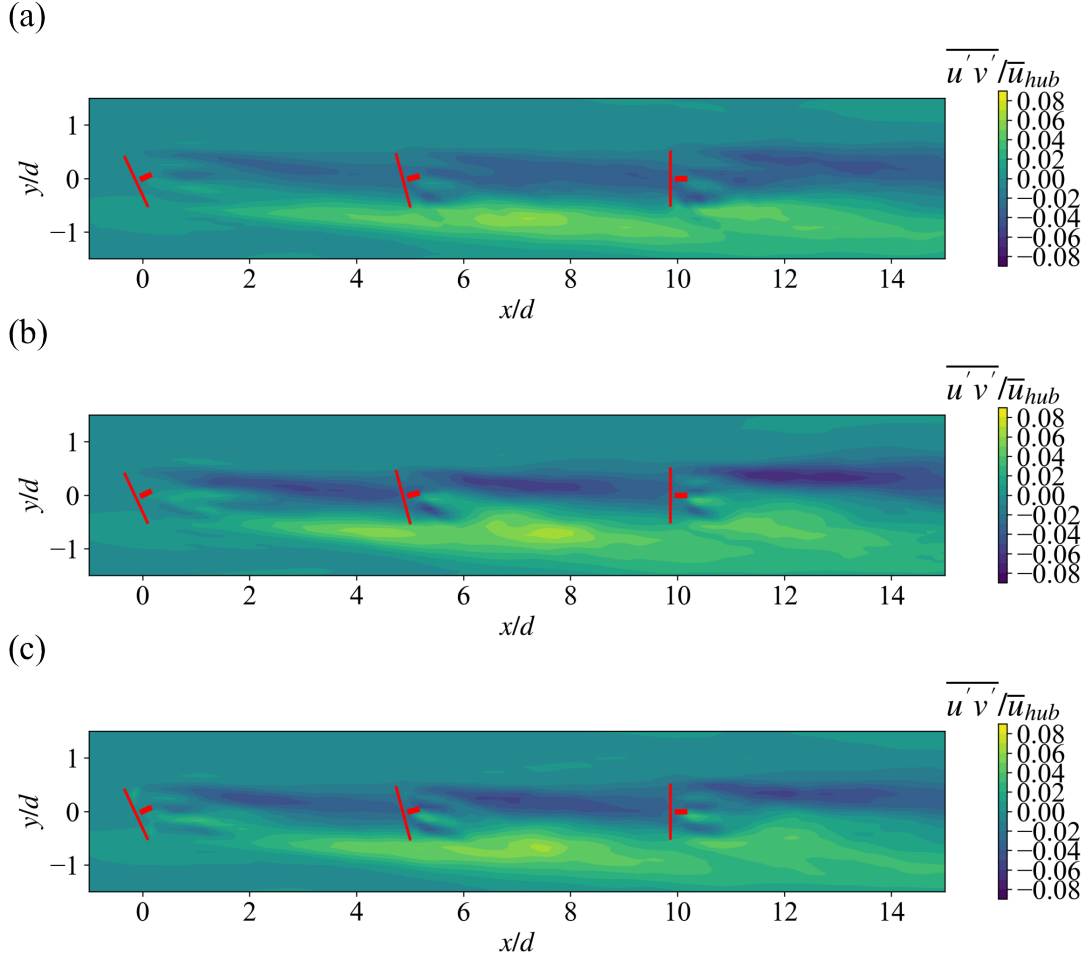


Figure 3.18: Contours of the normalised turbulence flux  $\overline{u'v'}/\overline{u}_{hub}$  in the  $x$ - $y$  plane at hub height obtained from LES using the (a) ADM-std, (b) ADM-BE and (c) ALM in the yawed Case 2 ( $\gamma = (-25^\circ, -15^\circ, 0^\circ)$ ).

coefficients predicted by the ALM is halved to a level below the uncertainty bound. On the other hand, the prediction of the ADM-std only changes marginally with the grid refinement and still overestimates the power coefficient to a level beyond the measurement uncertainty.

Figure 3.20 shows the simulated and measured power of the three-turbine array in Cases 1 to 4 specified in Table 3.1. Figure 3.21 shows the corresponding errors of the simulated power with respect to the measured power for each turbine. The power outputs and the errors are normalised by the measured power of the first turbine of the array in zero yaw. Using the data shown in Figure 3.20 and 3.21, we further compute the normalised total power error of the three-turbine array in Cases 1 to 4 (Figure 3.22) and use it as the metric to evaluate the predictions of different parametrisations. This metric is defined as the  $L^1$  norm (the summation of absolute values) of the power error of each turbine in the array, normalised by

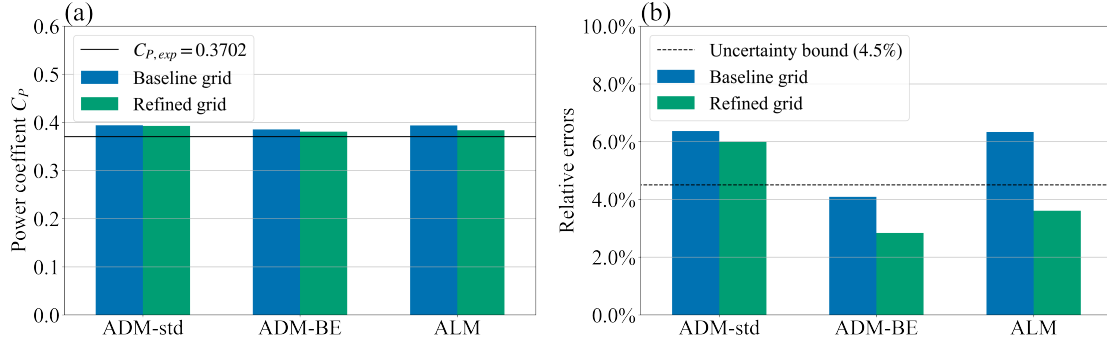


Figure 3.19: (a) Power coefficients of the first turbine in the turbine array in zero yaw. The black solid line marks the measured power coefficient. (b) Relative errors of the power coefficient compared to the power measurement. The black dashed line marks the uncertainty bound of the power measurement.

the total measured power in each case:

$$\tilde{\epsilon}_{tot} = \frac{\sum_{i=1}^3 |\epsilon_i|}{\sum_{i=1}^3 P_{i,exp}}, \quad |\epsilon_i| = |P_{i,sim} - P_{i,exp}|. \quad (3.10)$$

We find that the ADM-BE, which explicitly resolves the torque, and therefore the power, yields more accurate power predictions than the ADM-std. The errors in the ADM-std results can be attributed to the basic formulation of the model. Firstly, the model assumes a uniform thrust force distribution on the rotor. As we have shown in Figures 3.12 and 3.13, due to the inaccuracy of the uniform force assumption, the ADM-std yields shifted maximum velocity deficit trajectories compared to the measurements. Such errors in the wake velocity distribution affect the power prediction. Secondly, the ADM-std computes the power indirectly using an estimated inflow velocity reconstructed from the local disk-averaged velocity based on 1D momentum theory (Eqs. 3.6 and 3.7) and a pre-determined power curve. Since the power curve is obtained from the measurements of a turbine facing an undisturbed inflow, it is expected to be less accurate for turbines in yawed and waked conditions. Moreover, the difference between the inflow velocity reconstructed from the local disk-averaged velocity and the hub-height velocity used to normalise the power curve also introduces some errors to the power prediction. In certain scenarios, the errors originating from the aforementioned factors can cancel with each other, but overall we observe larger total errors in the power predictions of the ADM-std than the ADM-BE.

We also find that, in general, the ADM-BE outperforms the ALM, even if both of them are torque-resolving parametrisations. This is consistent with previous studies (Martinez et al., 2012; Martínez-Tossas et al., 2015) showing that the power prediction from the ALM is more sensitive to the mesh resolution than the ADM-BE. As a result, the ALM usually fails to yield satisfactory power prediction in the simulation employing a grid resolution with less than 30 grid points along the rotor diameter (Draper & Usera, 2015; Martínez-Tossas et al., 2015;



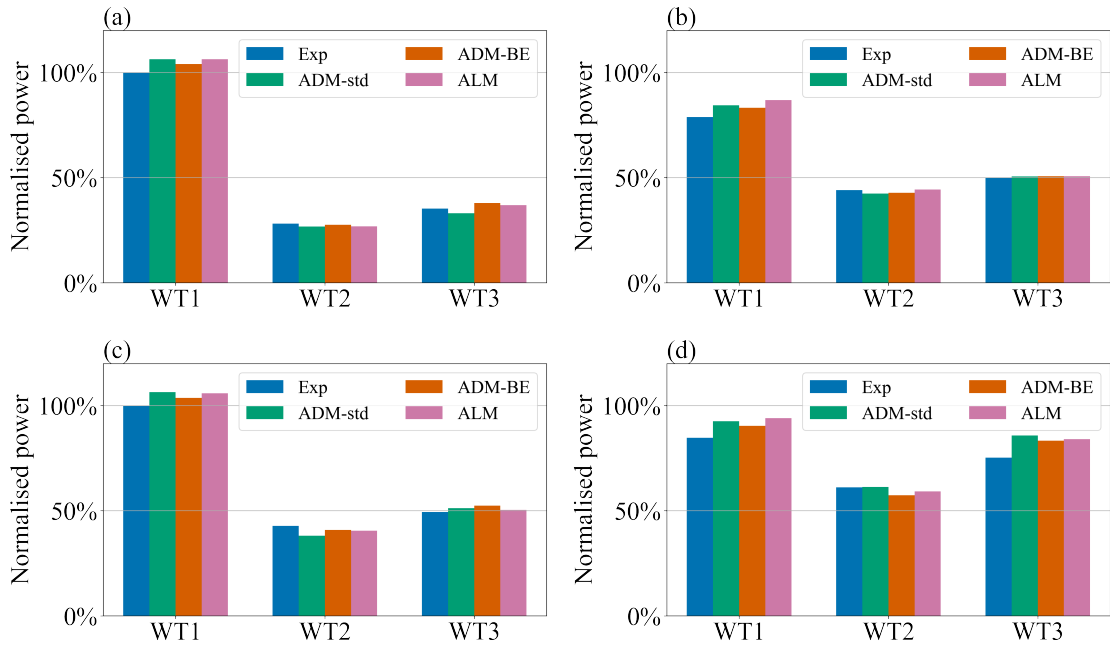


Figure 3.20: Normalised power outputs in (a) Case 1:  $\gamma = (0^\circ, 0^\circ, 0^\circ)$ , zero offset; (b) Case 2:  $\gamma = (-25^\circ, -15^\circ, 0^\circ)$ , zero offset; (c) Case 3:  $\gamma = (0^\circ, 0^\circ, 0^\circ)$ ,  $d/3$  offset; (d) Case 4:  $\gamma = (-20^\circ, -20^\circ, 0^\circ)$ ,  $d/3$  offset. The power outputs are normalised by the measured power of the zero-yawed first turbine of the turbine array.

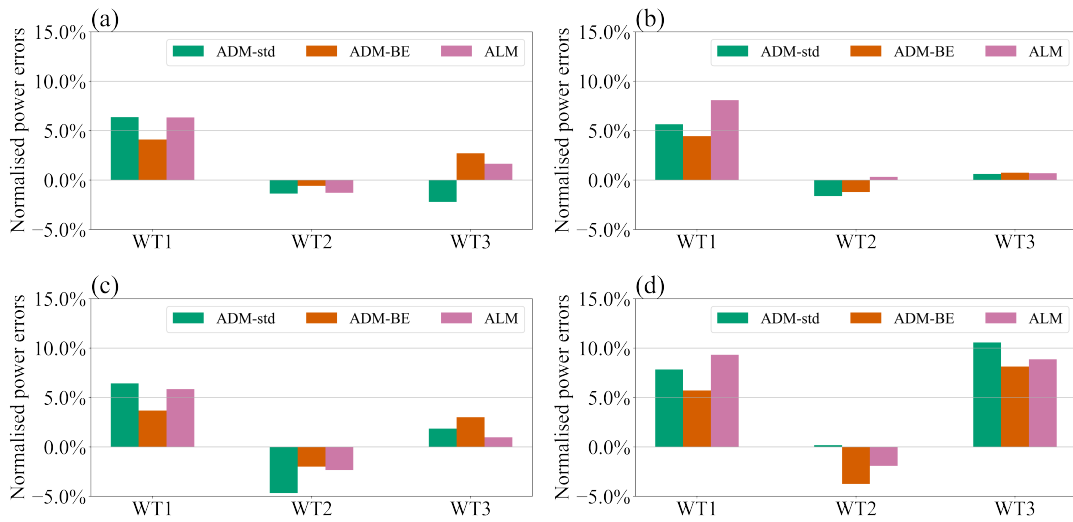


Figure 3.21: Normalised power errors in (a) Case 1:  $\gamma = (0^\circ, 0^\circ, 0^\circ)$ , zero offset; (b) Case 2:  $\gamma = (-25^\circ, -15^\circ, 0^\circ)$ , zero offset; (c) Case 3:  $\gamma = (0^\circ, 0^\circ, 0^\circ)$ ,  $d/3$  offset; (d) Case 4:  $\gamma = (-20^\circ, -20^\circ, 0^\circ)$ ,  $d/3$  offset. The power outputs are normalised by the measured power of the zero-yawed first turbine of the turbine array.

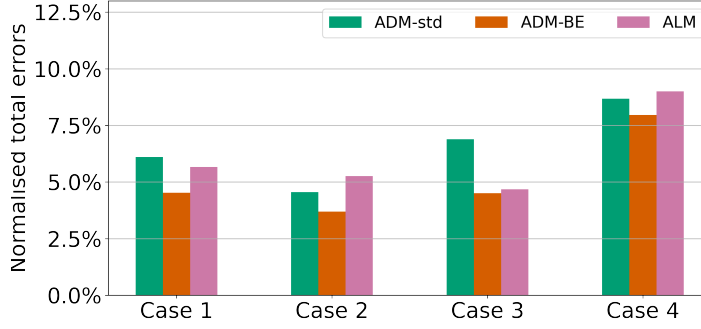


Figure 3.22: Normalised total power errors of the three-turbine array. The errors are normalised by the total measured power of the wind turbine array in each case. Case 1:  $\gamma = (0^\circ, 0^\circ, 0^\circ)$ , zero offset; Case 2:  $\gamma = (-25^\circ, -15^\circ, 0^\circ)$ , zero offset; Case 3:  $\gamma = (0^\circ, 0^\circ, 0^\circ)$ ,  $d/3$  offset; Case 4:  $\gamma = (-20^\circ, -20^\circ, 0^\circ)$ ,  $d/3$  offset.

Stevens et al., 2018).

### 3.4 Summary

In this study, we validate an LES framework with different wind turbine force parametrisations (the ADM-std, ADM-BE and ALM) to predict the flow through a three-turbine array. The simulations are set to match existing wind tunnel experiments for which flow and power measurements are available for different turbine lateral offsets (with respect to the wind direction) and different active yaw control strategies.

Comparisons with wind tunnel measurements show that LES with wind turbine models that capture the local distribution of the turbine-induced forces (the ADM-BE and ALM) provide reasonably accurate predictions of the streamwise mean velocity and the streamwise turbulence intensity in the wakes of the three wind turbines for all the considered conditions of lateral offset and yaw control. In contrast, the wake flows simulated with the standard actuator disk model (the ADM-std) show a lateral shift with respect to the measurements when the turbines are exposed to partial wake conditions produced by either lateral offset of the turbines or/and active yaw control. This is due to the fact that the assumption of uniform thrust force made by the ADM-std hinders the model from capturing the non-uniform force distribution experienced by the rotor and, consequently, the correct wake velocity distribution under partial wake conditions. Moreover, we find that LES using the ADM-BE yields overall better power predictions than the ADM-std and the ALM in the cases considered in this study. The ADM-BE is found to be better suited for the conditions of turbine yawing and partial wake overlapping than the ADM-std because the ADM-BE computes the power from the torque that is explicitly resolved on the rotor. The ADM-BE is also found to be more computationally efficient than the ALM, as the ALM requires finer grid resolution to produce satisfactory power

predictions.

From the results mentioned above, we conclude that the ADM-BE provides a good balance between accuracy and computational cost for the simulation of wind farm flows. In our future research, we plan to apply the validated LES framework to investigate optimal AYC strategies under different atmospheric conditions, e.g., turbulence intensity and atmospheric stability. Furthermore, since the ADM-BE and ALM explicitly resolve the turbine forces, the LES framework could also be applied to study structural loads in wind farms subjected to AYC.

### 3.5 Appendix

Here we present results from a grid sensitivity analysis to investigate the influence of grid resolution on the results obtained with LES. Figure 3.23 shows the hub-height profiles of the mean velocity and turbulence intensity in the wake behind a yawed turbine ( $\gamma = -25^\circ$ ) obtained from the measurements and the simulations using the ADM-std, the ADM-BE and the ALM. The simulations are carried out on the baseline grid specified in Sec. 4.2 and a refined grid ( $\times 2$  refinement in  $x$ ,  $y$  and  $z$  directions from the baseline grid). Overall, we find that simulation results converge and agree reasonably well with the measurements when the grid is refined.

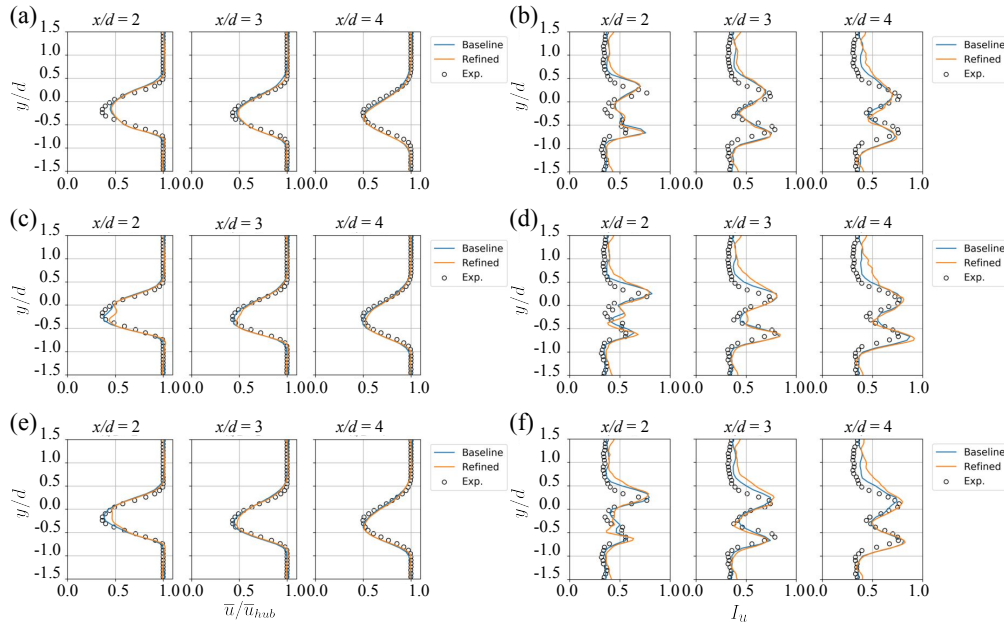


Figure 3.23: Profiles of the normalised streamwise mean velocity (left column) and turbulence intensity (right column) in the  $x - y$  plane at the hub height, obtained from the wind-tunnel experiments and the LES at different grid resolutions. (a) and (b): the ADM-std; (c) and (d): the ADM-BE; (e) and (f): the ALM. The yaw angle of the wind turbine is  $-25^\circ$ .



## 4 Power and fatigue of a wind-turbine array under active yaw control

### Abstract

This study investigates the power production and blade fatigue of a three-turbine array subjected to active yaw control (AYC) in the full-wake and partial-wake configurations. A framework of two-way coupled large-eddy simulation (LES) and aeroelastic blade simulation is applied to simulate the atmospheric boundary-layer (ABL) flow through the turbines and the structural responses of the blades. The mean power outputs and blade fatigue loads are extracted from the simulation results. By exploring the feasible AYC decision space, we find that, in the full-wake configuration, the local power-optimal AYC strategy with positive yaw angles endures less flapwise blade fatigue and more edgewise blade fatigue than the global power-optimal strategy. In the partial-wake configuration, applying positive AYC in certain inflow wind directions achieves higher optimal power gains than that in the full-wake scenario and reduces blade fatigue from the non-yawed benchmark. Using the blade-element momentum (BEM) theory, we reveal that the aforementioned differences in flapwise blade fatigue are due to the differences in the azimuthal distributions of the local relative velocity on blade sections, resulting from the vertical wind shear and blade rotation. Furthermore, the difference in the blade force between the positively and negatively yawed front-row turbine induces different wake velocity and turbulence distributions, causing different fatigue loads on the downwind turbine exposed to the wake.

### 4.1 Introduction

Active yaw control (AYC) is a wind farm control strategy which has recently attracted wide interest in the wind energy community. When wind farm operators apply AYC, they intentionally yaw upwind turbines to steer their wakes away from downwind turbines. While the yawed turbines reduce their power outputs, with a proper AYC strategy, the wind farm can yield more power and endure less structural fatigue because wake interference between wind turbines is mitigated.

Several experimental (Bastankhah & Porté-Agel, 2019; Campagnolo et al., 2022; Grant et al., 1997; Howland et al., 2016; Medici & Alfredsson, 2006; Zong & Porté-Agel, 2021) and computational (Archer & Vassel-Be-Hagh, 2019; Fleming et al., 2018; Fleming et al., 2014; Jiménez et al., 2010; Lin & Porté-Agel, 2019; Munters & Meyers, 2018a) studies have been conducted to investigate the effectiveness of AYC for wind-farm power optimisation. Recently, there has been growing interest among wind energy researchers in jointly considering fatigue reduction and power optimisation when applying AYC. Kragh and Hansen (2014) first pointed out the potential of AYC for reducing load variations on wind turbine blades caused by vertical wind shear. Zalkind and Pao (2016) later investigated the fatigue loads of a stand-alone wind turbine at different yaw angles. They found that for a clockwise-rotating (when viewed from the front) wind turbine in the vertically sheared wind, positive yaw strategies (counter-clockwise yaw when viewed from the top) decrease the damage equivalent load (DEL) of the out-of-plane (OOP) blade bending moment, while negative yaw strategies increase it. Using large-eddy simulation (LES), Fleming et al. (2015) studied a two-turbine case subjected to AYC in the full-wake condition, and they reported that applying proper positive yaw strategies can increase power outputs and reduce turbine fatigue. Damiani et al. (2018) measured the component loads acting on a utility-scale turbine under yaw conditions and also confirmed the dichotomy of positive yaw and negative yaw in wind turbine loads.

With the studies mentioned above confirming the potential of AYC for achieving power gain and fatigue reduction, wind energy researchers have conducted several optimisation studies that applied AYC to wind farms. Gebraad et al. (2017) optimised the annual power production of a hypothetical wind farm with AYC using a parametric wake model. Van Dijk et al. (2017) further incorporated a simplified load model into the wake model used in Gebraad et al. (2017) and performed a multi-objective optimisation of the power production and fatigue loads of a hypothetical wind farm subjected to AYC. Using a reduced-order flow solver, Kanev et al. (2018) applied AYC to real-world wind farms to optimise the lifetime power production and fatigue loading. Reyes et al. (2019) developed a computationally cheap look-up table approach to optimise fatigue loads in wind farms and validated it with wind tunnel and full-scale field tests. Ma et al. (2021) investigated the cooperative yaw strategies for a single column of turbines, and they found that significant power gains can be achieved using simplified strategies with only two yaw angles: the yaw angle of the first turbine and the one for the downstream turbines (excluding the last turbine). B. Li et al. (2022) further compared the cooperative yaw control and axis induction control, and they found that the yaw control is more effective than the

induction control in achieving meaningful power gains. Lin and Porté-Agel (2020) used LES to investigate Pareto-optimal AYC strategies for an array of three miniature wind turbines to maximise power production and minimise fatigue loads. They found Pareto-optimal yaw strategies with gradually decreasing yaw angles from upwind to downwind turbines.

As shown in the literature, AYC can potentially increase the power outputs and mitigate the fatigue loads of a wind farm with proper yaw strategies. However, a poorly chosen yaw strategy can also significantly increase wind turbine fatigue loads while only achieving marginal power gains. Therefore, the main objective of this study is to understand how the application of different AYC strategies affects power production and fatigue loading for a wind farm under various inflow configurations.

The rest of the chapter is structured as follows. In Section 4.2, we discuss the two-way coupled aeroelastic LES frameworks used in this study and the methodology for evaluating power production and fatigue loads. In Section 4.3, we present the results of the simulations using different configurations. In Section 4.4, we present a theoretical analysis of the differences in flapwise blade fatigue in the turbines under positive and negative yaw strategies. In Section 4.5, we present the conclusions drawn from these findings and discuss possible extensions of this study.

## 4.2 Methodology

### 4.2.1 Governing equations

This study uses the GPU-accelerated version of the in-house WiRE-LES code (Abkar & Porté-Agel, 2015; Lin & Porté-Agel, 2019; Porté-Agel et al., 2011a; Wu & Porté-Agel, 2011), which solves the spatially filtered, incompressible Navier-Stokes equations:

$$\frac{\partial \tilde{u}_i}{\partial x_i} = 0, \quad (4.1)$$

$$\frac{\partial \tilde{u}_i}{\partial t} + \tilde{u}_j \left( \frac{\partial \tilde{u}_i}{\partial x_j} - \frac{\partial \tilde{u}_j}{\partial x_i} \right) = -\frac{\partial \tilde{p}^*}{\partial x_i} - \frac{\partial \tau_{ij}}{\partial x_j} + \frac{F_p}{\rho} \delta_{i1} - \frac{\tilde{f}_i}{\rho}, \quad (4.2)$$

where the subscript  $i$  represents the streamwise ( $i = 1$ ), spanwise ( $i = 2$ ) and vertical ( $i = 3$ ) directions of the ground-fixed coordinate system  $x - y - z$  (Figure 4.1), respectively,  $\tilde{u}_i$  is the spatially filtered flow velocity,  $\tilde{p}^*$  is the modified kinematic pressure,  $F_p$  is the pressure gradient imposed on the flow,  $\tau_{ij} = \overline{u_i u_j} - \tilde{u}_i \tilde{u}_j$  is the kinematic sub-grid scale stress, and  $\tilde{f}_i$  are the forces exerted by the wind turbine blades, the nacelle, and the tower on the flow.

To incorporate aeroelasticity in the simulation, we treat the rotating wind turbine blades as 1d Euler-Bernoulli beams governed by the dynamic Euler-Bernoulli equations (Meng et al., 2018):

$$\frac{\partial^2 q_k}{\partial t^2} + \frac{1}{\mu} \frac{\partial^2 M_k}{\partial r^2} = \frac{1}{\mu} \frac{\partial}{\partial r} \left( \int_r^R \mu \omega^2 r dr \frac{\partial q_k}{\partial r} \right) + g_k + \frac{\hat{f}_k}{\mu}, \quad (4.3)$$

$$M_k = K_{kl} \frac{\partial^2 q_l}{\partial r^2}, \quad (4.4)$$

where the subscript  $k$  specifies the flapwise ( $k = 1$ ) and edgewise ( $k = 2$ ) directions of the blade-following coordinate system  $x'_n - y'_n - z'_n$  for the  $n$ th blade (Figure 4.1),  $r$  is the distance between the blade element and the hub centre,  $q_k$  is the blade deformation,  $M_k$  is the blade bending moment,  $g_k$  is the component of gravitational acceleration in the  $k$ th direction,  $\mu$  is the blade mass per unit length,  $\hat{f}_k$  is the aerodynamic load exerted by the flow on the blade,  $K_{kl}$  is the stiffness matrix of the blade section, and  $\omega$  is the rotational speed of the rotor.

#### 4.2.2 Simulation setup

In the WiRE-LES code, the filtered Navier-Stokes equations are solved numerically using the pseudo-spectral method in the horizontal directions ( $x$  and  $y$ ) and the second-order finite-difference scheme in the vertical direction  $z$ . Time integration is done using the second-order Adam-Bashforth method. The sub-grid scale stress term is parametrised by the modulated gradient model (Lu & Porté-Agel, 2010). The body forces induced by the wind turbine blades are parametrised with the elastic actuator line model (EALM) proposed by Meng et al. (2018). The EALM simultaneously resolves the aerodynamic forces on turbine blade elements as the classical ALM (Sørensen & Shen, 2002) and solves the discretised Euler-Bernoulli beam equations using the finite-difference time-domain method to obtain blade deformations. The deformations are then used to update the ALM calculation in the next time step. The two-way coupling procedure in the EALM is summarised in Figure 4.2.

In this study, the simulation domain ( $L_x \times L_y \times L_z = 4096 \text{ m} \times 2048 \text{ m} \times 1024 \text{ m}$ ), shown in Figure 4.3, is discretised into a  $512 \times 256 \times 512$  grid uniformly in each direction. A wind-turbine array consisting of three NREL 5 MW reference wind turbines (Jonkman et al., 2009), with a  $7d$  distance between each turbine, is placed in the simulation domain. The wind turbines are not tilted. The turbine rotational speed in the simulation is determined by the dynamic torque-balance procedure proposed by Wu and Porté-Agel (2015). The first two wind turbines are subjected to yaw control, while the last turbine is not yawed. In the vertical direction ( $z$ ) of the domain, a slip-wall boundary condition is applied to the top, and a non-penetration wall boundary condition with specified stresses according to the logarithmic law of the wall is applied to the bottom. Periodic boundary conditions are applied to the lateral boundaries in the horizontal directions. The inflow is generated by a precursor simulation without the wind turbine array and is then imposed at the inlet section of the simulation domain with wind turbines. A buffer section is added in front of the inflow section to transform the flow from the



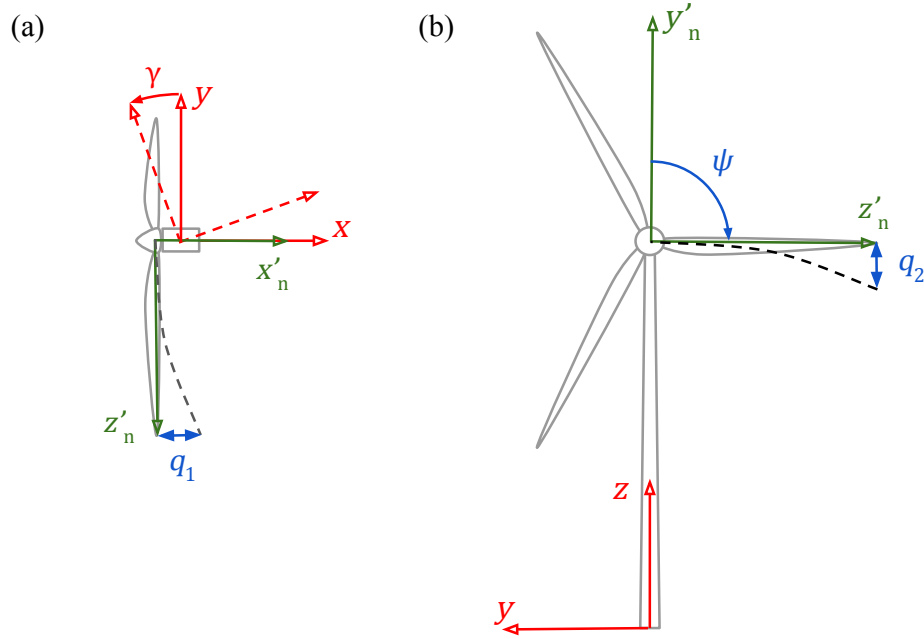


Figure 4.1: The ground-fixed coordinate system  $x - y - z$  for solving the filtered Navier-Stokes equations and the blade-following coordinate system  $x'_n - y'_n - z'_n$  for solving the Euler-Bernoulli beam equations for the  $n$ th blade: (a) top view; (b) front view.  $\psi$  is the phase angle of the blade.  $\gamma$  is the yaw angle of the turbine. The positive directions of  $\psi$  and  $\gamma$  follow the right-hand rule.

outlet to the inlet of the simulation domain through a smooth weighting function. The mean streamwise hub-height inflow velocity  $\bar{u}_{hub} = 10$  m/s, and the streamwise hub-height inflow turbulence  $I_u = 7.5\%$ .

### 4.2.3 Fatigue evaluation

In this study, wind turbine fatigue damage is quantified according to the damage equivalent loads (DELs) of blade-root bending moments (flapwise and edgewise). The procedures for computing DELs are as follows (Freebury & Musial, 2000):

- Extract time series of blade-root bending moments from the LES coupled with the EALM.
- Apply the rainflow cycle-counting algorithm and extract the histograms of load-cycle means  $M_{mean}$  and load-cycle ranges  $M_{range}$ .
- Use Goodman's rule to correct the effect of mean loads on fatigue damages and obtain

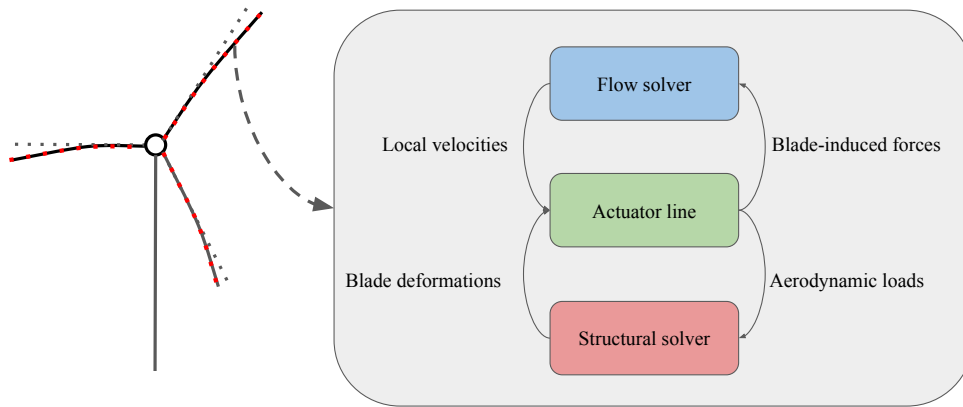


Figure 4.2: The coupling procedure between the flow solver and the structural solver in the EALM. The arrows in the flowchart represent the variable passing between different modules of the solver.

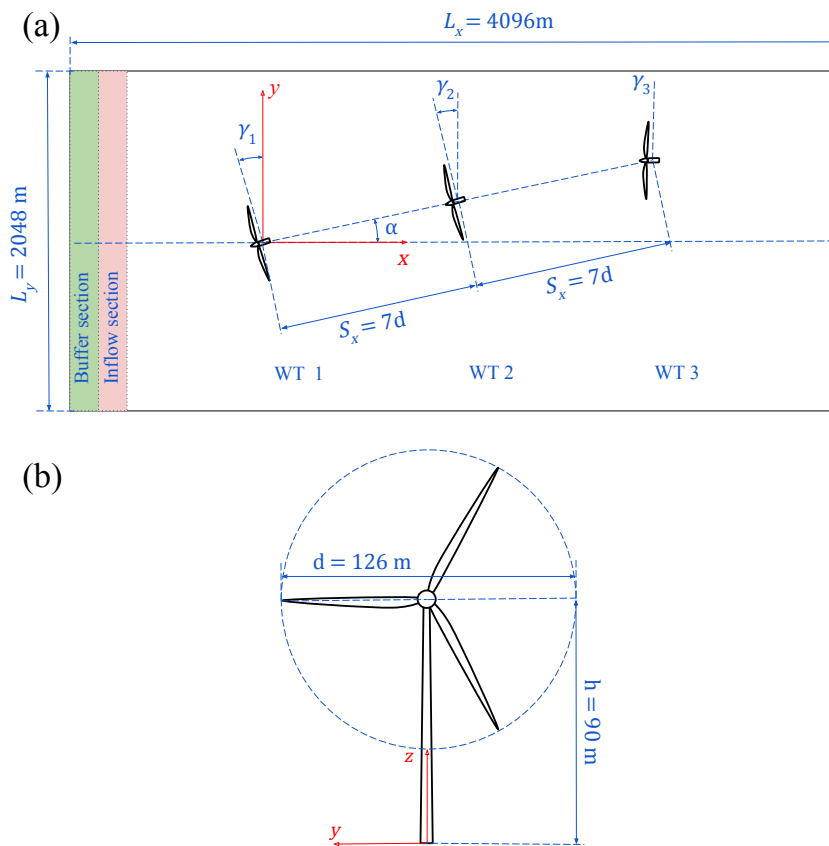


Figure 4.3: Schematic plots (not to scale) of (a) the simulation domain; (b) NREL 5MW reference wind turbine.

the corrected cycle range  $M'_{range,k}$  for the  $k$ th bin of the histogram:

$$M'_{range,k} = \frac{M_{range,k}}{1 - \frac{M_{mean,k}}{\sigma M_{max}}}, \quad (4.5)$$

where  $M_{max}$  is the maximum bending moment of the time series,  $\sigma$  is a safety factor, and its value is chosen as 1.5.

- Use the Palmgren-Miner rule, which assumes linear accumulation of fatigue damages, to compute DELs:

$$M_{DEL} = \left( \frac{\sum_{k=1}^{n_b} n_k M'_{range,k}{}^m}{N_{ref}} \right)^{1/m}, \quad (4.6)$$

where  $n_b$  is the total bin number of the histogram extracted from the rainflow cycle-counting,  $n_k$  is the cycle count of the  $k$ th bin of the histogram,  $N_{ref}$  is the reference cycle number, and  $m$  is a material parameter which takes the value of 10 for composite materials.

## 4.3 Results

In this section, we present the simulation results of different AYC strategies in the full-wake and partial-wake configurations. The AYC decision space is defined by the yaw angles of the first two turbines in the array (WT 1 and WT 2):  $\Gamma = \{\gamma_1 : -30^\circ, -25^\circ, \dots, 25^\circ, 30^\circ\} \times \{\gamma_2 : -30^\circ, -25^\circ, \dots, 25^\circ, 30^\circ\}$ <sup>1</sup>, and the yaw angle of the last turbine is fixed to  $0^\circ$ . A time window of 800 s is chosen to extract the mean velocity fields, mean power outputs and fatigue loads based on the recommendations of IEC standards (IEC, 2019).

### 4.3.1 Velocity deficits

Figure 4.4 shows the contours of the normalised mean streamwise velocity deficits  $\Delta \bar{u} / \bar{u}_{hub}$  of six representative cases (Table 4.1) in the horizontal  $x - y$  plane at the hub height. The wind turbine array is in the full-wake configuration  $\alpha = 0^\circ$  in Cases (a-c) and partial-wake configuration  $\alpha = 3^\circ$  in Cases (d-f).

When the turbine array is in the full-wake configuration  $\alpha = 0^\circ$  (Figures 4.4a - 4.4c), we observe that applying positive and negative yaw strategies deflects the wakes of upwind turbines away from downwind turbines. When the array is in partial-wake configuration  $\alpha = 3^\circ$  (Figures 4.4d - 4.4f), the positive yaw strategy is clearly more favourable due to the spanwise offset of the turbines. In Figure 4.4e, wake interference is largely avoided by applying positive yaw, whereas

<sup>1</sup>When viewed from the front, the NREL 5 MW reference turbine rotates clockwise, while WiRE-01 rotates counter-clockwise. Therefore, for the NREL 5MW turbine, the yaw angle is defined as positive when the turbine is yawed counter-clockwise (when viewed from the top).

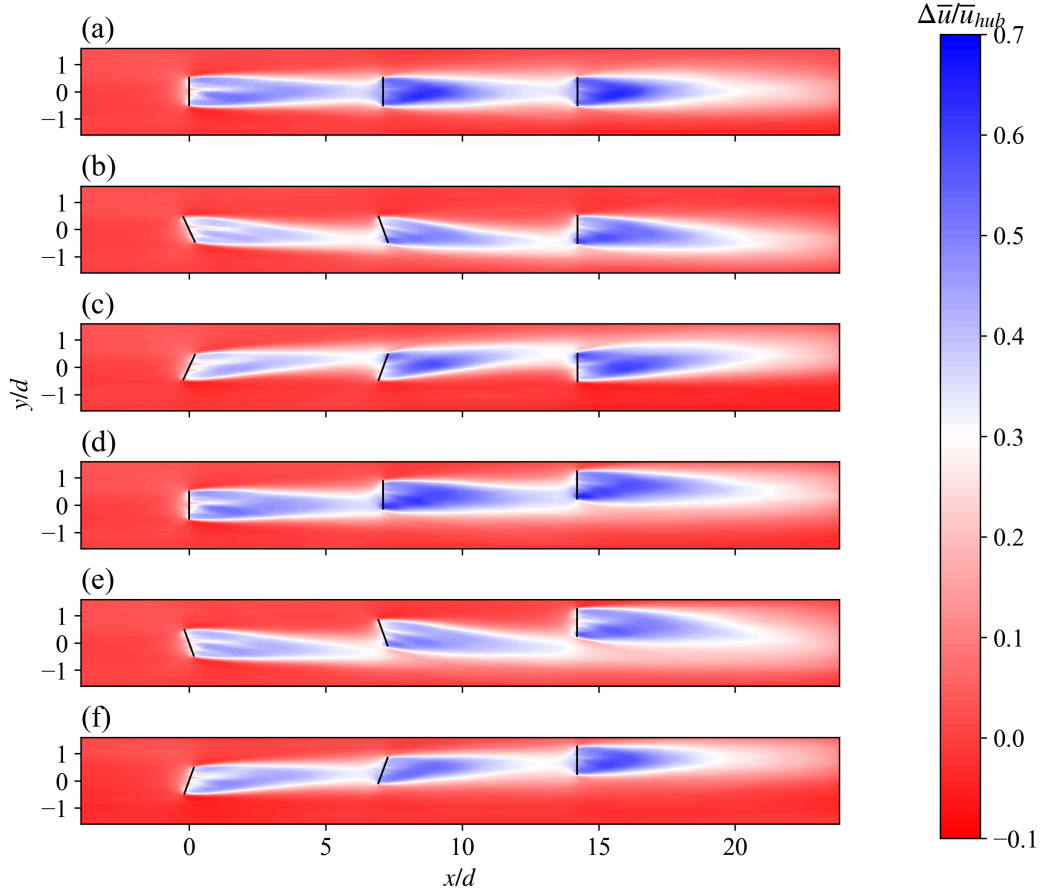


Figure 4.4: Top-view  $x - y$  cross-section contours of normalised streamwise mean velocity deficits  $\Delta\bar{u}/\bar{u}_{hub}$  at the hub height. Full-wake configuration ( $\alpha = 0^\circ$ ): (a)  $\gamma = (0^\circ, 0^\circ, 0^\circ)$ ; (b)  $\gamma = (25^\circ, 20^\circ, 0^\circ)$ ; (c)  $\gamma = (-25^\circ, -20^\circ, 0^\circ)$ . Partial-wake configuration ( $\alpha = 3^\circ$ ): (d)  $\gamma = (0^\circ, 0^\circ, 0^\circ)$ ; (e)  $\gamma = (25^\circ, 20^\circ, 0^\circ)$ ; (f)  $\gamma = (-25^\circ, -20^\circ, 0^\circ)$ .

in Figure 4.4f, the application of negative yaw aggravates the interference of the wakes. We also observe the phenomenon of secondary wake deflection in the results, i.e., the additional deflection in the wake of a non-yawed turbine exposed to the wake of the yawed upwind turbine. For example, as shown in Figures 4.4b and 4.4c, although WT 3 itself is not yawed, the wake of WT 3 is still deflected when the turbine is exposed to the wake of the yawed upwind turbine. The secondary wake deflection is caused by the non-zero cross-flow in the wake of the yawed upwind turbine (Bastankhah & Porté-Agel, 2016; Zong & Porté-Agel, 2020b).

To further compare the wake structure of non-yawed and yawed turbines, in Figure 4.5 we show the contours of normalised mean streamwise velocity deficits  $\Delta\bar{u}/\bar{u}_{hub}$  in the vertical  $y - z$  cross-section plane  $6d$  downwind of WT 1. The velocity deficit contours are overlapped with the vector fields of in-plane velocity components ( $\bar{v}$  and  $\bar{w}$ ). In the non-yawed case (Figure 4.5a), the velocity deficit region is largely circular; in the yawed cases (Figures 4.5b and 4.5c), a distinctive asymmetric kidney-shaped (curled) velocity deficit region is found in the wakes

Table 4.1: Configurations of the six representative cases in the full-wake and partial-wake configurations.

Case	Yaw angle ( $\gamma$ )	Inflow angle ( $\alpha$ )
(a)	(0°, 0°, 0°)	0°
(b)	(25°, 20°, 0°)	0°
(c)	(-25°, -20°, 0°)	0°
(d)	(0°, 0°, 0°)	3°
(e)	(25°, 20°, 0°)	3°
(f)	(-25°, -20°, 0°)	3°

behind yawed turbines, which is associated with the formation of a counter-rotating vortex pair (CVP) (Bastankhah & Porté-Agel, 2016; Shapiro et al., 2018; Zong & Porté-Agel, 2020b). The CVP is induced by the cross-flow in the wake, which creates a skewed inflow for downwind turbines and leads to additional wake deflection behind those turbines.

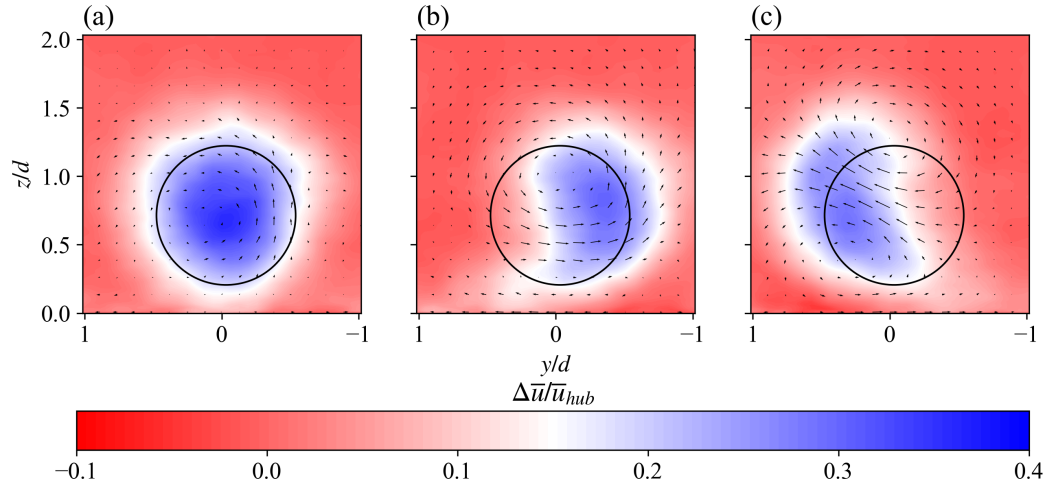


Figure 4.5: Front-view  $y - z$  cross-section contours of normalised streamwise velocity deficits  $\Delta\bar{u}/\bar{u}_{hub}$  at the location  $6d$  downwind of WT 1, overlapped with vector fields of in-plane velocity components: (a)  $\gamma_1 = 0^\circ$ ; (b)  $\gamma_1 = 25^\circ$ ; (c)  $\gamma_1 = -25^\circ$ .

Furthermore, as shown in Figure 4.5, the wake structure of the positively yawed turbine (Figure 4.5b) differs from its negatively yawed counterpart (Figure 4.5c). On the vertical  $y - z$  cross-section plane, the upper half of the velocity deficit region behind the negatively yawed turbine is deflected further away from the domain centre-line ( $y/D = 0$ ) than its counterpart behind the positively yawed turbine. The lower half of the wake deficit region, on the other hand, is closer to the centre line ( $y/D = 0$ ) behind the negatively yawed turbine than that of the positively yawed one. The cross-flow in the wake of the positively yawed turbine is largely horizontal, whereas the direction of the cross-flow behind the negatively yawed turbine is around  $45^\circ$  upwards. Zong and Porté-Agel (2020b) observed a similar dichotomy of the wake structure of a positively and negatively yawed turbine in the wind tunnel experiments carried

out in their study, and they explained it by the different vorticity evolution behind a positively yawed and negatively yawed turbine, which affects the deformation of the velocity deficit region.

### 4.3.2 Power production

The power production of wind farms subjected to AYC is an important metric for evaluating different AYC strategies. Figure 4.6 shows the normalised power outputs of the six representative cases specified in Table 4.1. In the full-wake configuration (Figure 4.6a), the positive and negative yaw strategies yield very similar power outputs for WTs 1 and 2; for WT 3, the negative yaw strategy yields 5.7% more power than the positive one because negative yaw induces larger wake deflection than positive yaw (Zong & Porté-Agel, 2020b). In partial-wake configuration  $\alpha = 3^\circ$  (Figure 4.6b), applying positive yaw can help to achieve power gains in the downwind turbines. In contrast, applying negative yaw redirects the wakes back to downwind turbines, as shown in Figure 4.5f, and leads to power losses for all three turbines.

Figure 4.7 shows the contours of the normalised total power gains in the AYC decision space  $\Gamma$  with different inflow angles  $\alpha$ . Normalisation is carried out using the total power of the non-yawed baseline case  $P_0$ . The most noticeable difference between full-wake ( $\alpha = 0^\circ$ ) and partial-wake ( $\alpha \neq 0^\circ$ ) configurations is that there are two local optima in the decision space of the full-wake configuration, while there is only one optimum for partial-wake configurations. Consistent with the experimental results of Zong and Porté-Agel (2021), the local power optimum corresponding to negative yaw (+5.14%) is larger than the one corresponding to positive yaw (+4.23%). Furthermore, in the partial-wake configurations under consideration ( $\alpha = \pm 3^\circ, \pm 5^\circ$ ), smaller yaw angles are needed to alleviate the wake interference in the turbine array due to the spanwise offset of the wind turbines, and the power gains achieved by applying the optimal AYC are larger than the one in the full-wake configuration. The optimal power gains in the configurations with  $\alpha = \pm 5^\circ$  are also smaller than their counterparts with  $\alpha = \pm 3^\circ$ . This observation can be explained by the fact that the turbines in the non-yawed baseline cases become less exposed to the wake flows with the increasing magnitude of the inflow angle; hence, the room for power improvement with AYC is reduced.

### 4.3.3 Blade fatigue loading

Besides power production, fatigue loading is another critical metric to consider when applying AYC to a wind farm. Figure 4.8 shows the time-series segments of the flapwise bending moment (FBM) (Figure 4.8a) and the edgewise bending moment (EBM) (Figure 4.8b) at the blade root of WT 1. We find that, when the turbine is yawed, whether positively or negatively, the means of the FBM are decreased. However, a negatively yawed turbine has a larger FBM variation than the non-yawed baseline, while a positively yawed turbine has a smaller variation. As for the EBM, the differences between yawed and non-yawed turbines are less significant than the FBM because the variation in the EBM is dominated by the cyclic gravity load acting on

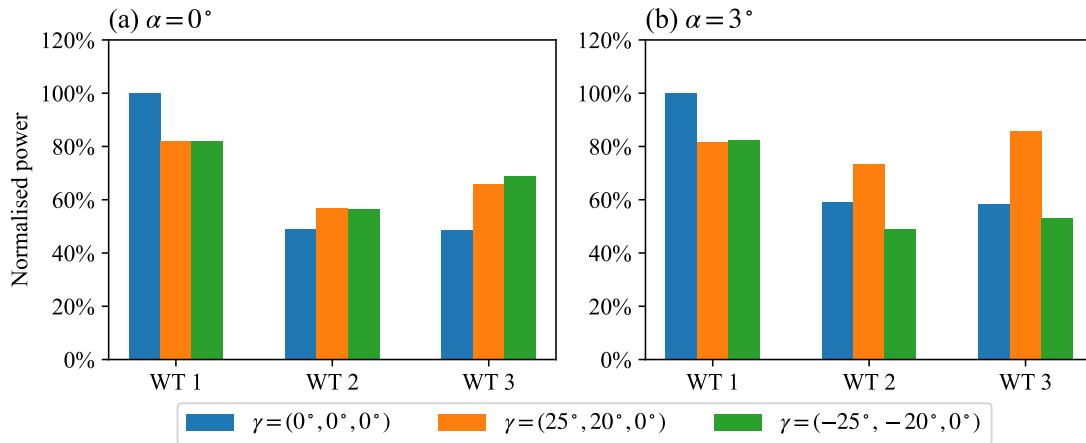


Figure 4.6: Normalised power outputs of different AYC configurations, normalised by the power of WT 1 in zero yaw (a) in the full-wake configuration  $\alpha = 0^\circ$  (b) in partial-wake configuration  $\alpha = 3^\circ$ .

rotating blades; thus, it is less sensitive to changes in the aerodynamic loads caused by AYC.

Using the transient blade loads extracted from the simulations, we further evaluate blade fatigue with the methodology discussed in Section 4.2.3. Figure 4.9 shows the flapwise and edgewise DELs for the wind turbine array at different AYC configurations. In the full-wake configuration  $\alpha = 0^\circ$ , we observe that:

- In the flapwise direction (Figure 4.9a), the positive yaw case has lower DELs in WTs 1 and 2 and a higher DEL in WT 3 compared to the non-yawed baseline. On the other hand, the negative yaw case has larger DELs than the baseline for all three turbines.
- In the edgewise direction (Figure 4.9c), applying positive yaw decreases the DEL in WT 1 while increasing it in WTs 2 and 3. The negative yaw strategy decreases the DELs for all three turbines.

In partial-wake configuration  $\alpha = 3^\circ$ , we observe that:

- In the flapwise direction (Figure 4.9b), the DELs of WTs 2 and 3 are larger than those of WT 1 in the non-yawed baseline. This is caused by the downwind turbines being partially exposed to the wakes of upwind turbines in this configuration, creating significant load variations on the blades. When the positive yaw strategy is adopted, as noted in the wake contour (Figure 4.4e), the wake interference is largely avoided, and the turbine fatigue loads are alleviated. Applying negative yaw in this configuration redirects the wakes back to the downwind turbines (Figure 4.4f), which also alleviates the partial wake overlapping. As a result, we observe decreases in the DELs of WT 2 and WT 3 in the negative yaw case.

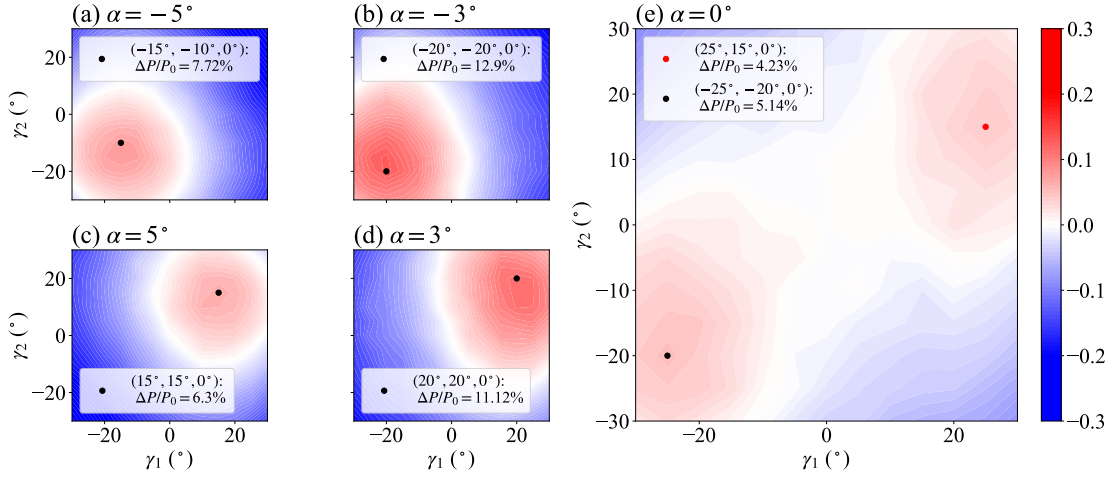


Figure 4.7: Normalised power gain contours in the AYC decision space  $\Gamma$  for different inflow angles. Black dots show the AYC configurations with the largest power gains.

- In the edgewise direction (Figure 4.9d), applying positive yaw decreases the DEL in WTs 1 and 2 while increasing it for WT 3. The negative yaw strategy reduces the DELs for all three turbines. Similar to the full-wake configuration, the edgewise DELs are less sensitive to changes in yaw angles than the FBM.

To further reveal the relation between blade fatigue in the turbine array and AYC, we define the summation of the DEL of each turbine as the total DEL of the turbine array and compute the normalised total DEL variation  $\Delta DEL / DEL_0$ . Normalisation is carried out using the total DEL of the non-yawed baseline case  $DEL_0$ . Figure 4.10 shows the contours of  $\Delta DEL / DEL_0$  in the flapwise (Figures 4.10a to 4.10e) and edgewise directions (Figures 4.10f to 4.10j) in the decision space  $\Gamma$  for different inflow angles. Consistent with our observations in Figures 4.8 and 4.9, we find that the changes in the flapwise DELs are more significant than in the edgewise DELs. Furthermore, in contrast to the power gain contours (Figure 4.7), we observe an asymmetry in the DEL variation contour: the AYC strategies with opposite signs for yaw and inflow angles produce similar power outputs but very different DELs. For example (Table 4.2), the two AYC strategies  $\gamma = (-20^\circ, -20^\circ, 0^\circ)$ ,  $\alpha = -3^\circ$  and  $\gamma = (20^\circ, 20^\circ, 0^\circ)$ ,  $\alpha = 3^\circ$  in the decision space  $\Gamma$  yield similar power gains (12.9% vs 11.12%). However, the negative strategy increases the flapwise DEL (+7.09%) and edgewise DEL (+0.54%) from the non-yaw benchmark, while the positive strategy  $\gamma_+$  decrease the flapwise DEL (-3.18%) but increases the edgewise DEL (+0.99%).

Table 4.2: Power gains and DEL variations for the configurations with opposite yaw angles.

$\gamma$	$\alpha$	$\Delta P / P_0$	$\Delta DEL_F / DEL_{F,0}$	$\Delta DEL_E / DEL_{E,0}$
$(-20^\circ, -20^\circ, 0^\circ)$	$-3^\circ$	12.9 %	7.09%	0.54%
$(20^\circ, 20^\circ, 0^\circ)$	$3^\circ$	11.12%	-3.18%	0.99%



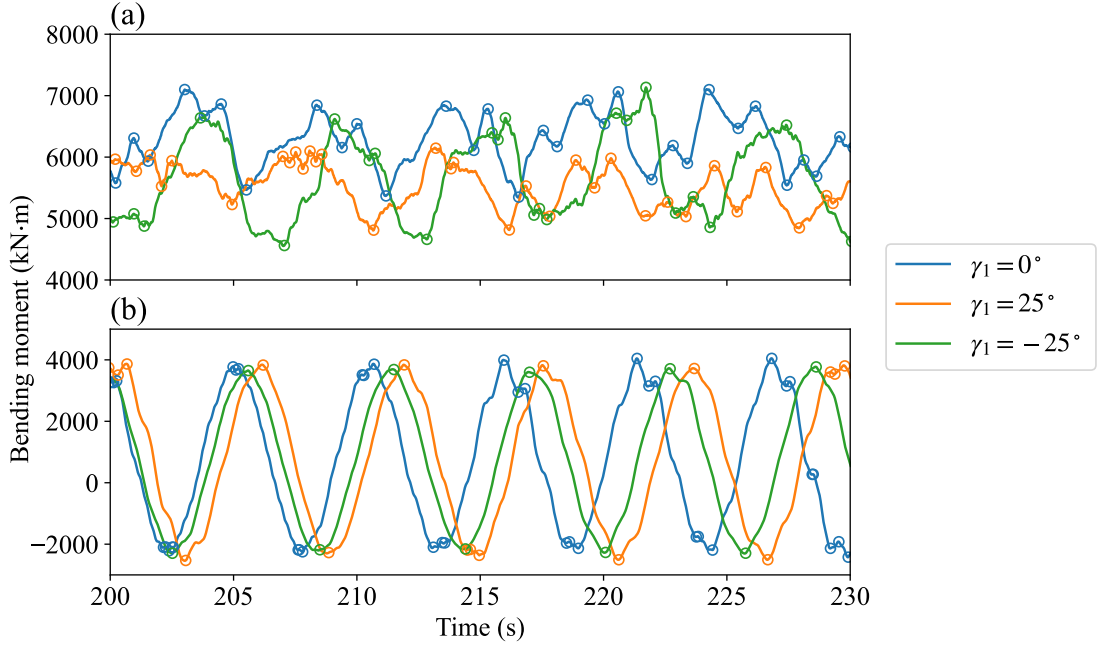


Figure 4.8: Time series segments of blade-root bending moments of WT 1: (a) flapwise bending moment; (b) edgewise bending moment. Empty circles show the load reversal points extracted by the rainflow counting algorithm.

#### 4.4 Theoretical analysis on flapwise blade fatigue

Figures 4.9 and 4.10 have shown that applying positive or negative yaw strategies leads to significantly different flapwise fatigue loading not only in the yawed turbines but also in the non-yawed turbines exposed to the wakes of yawed upwind turbines. In this section, we present a theoretical analysis of the causes of these differences.

Flapwise blade fatigue is induced by the variations of the force normal to the rotor disk  $F_n$  (Figure 4.11) acting on wind turbine blades. The force variation can be attributed to inflow turbulence and blade rotation. For a front-row turbine, it experiences the same level of inflow turbulence when it is positively or negatively yawed with the same yaw magnitude. Therefore, the difference in flapwise fatigue is mainly caused by the different blade-force variations per rotation, which can be analysed according to the blade element momentum (BEM) theory. Computing the aerodynamic forces acting on the rotating wind turbine blades based on the BEM theory requires an iterative process. However, we can simplify this process into closed-form expressions with reasonable approximations and directly analyse the variation of aerodynamic loads.

According to the velocity and force triangles in the BEM theory shown in Figure 4.11, the normal force  $F_n$  acting on a blade element per unit length can be expressed as follows:

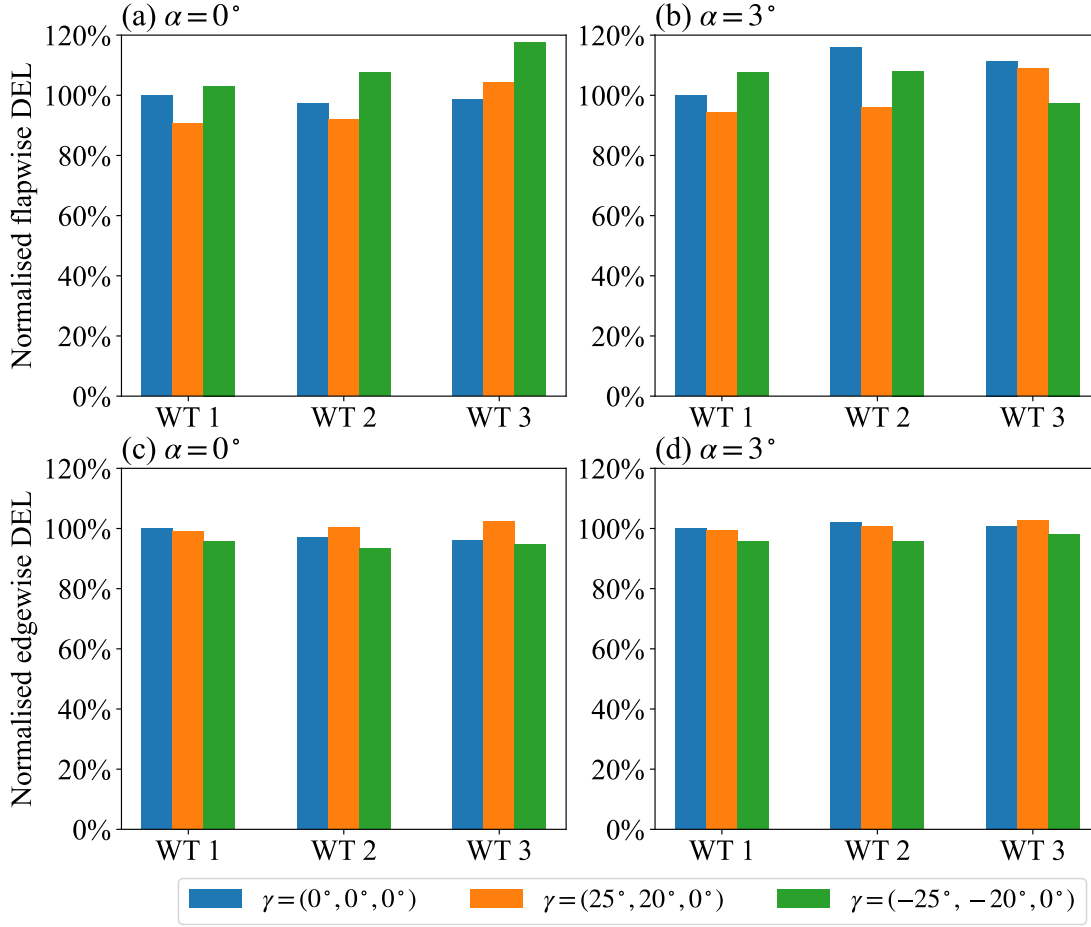


Figure 4.9: Normalised DELs of blade-root blending moments in different AYC configurations and inflow angles, normalised by the DELs of WT 1 in the zero-yaw condition: (a)-(b) flapwise bending moment; (c)-(d) edgewise bending moment.

$$F_n = \frac{1}{2} c \rho \left( \frac{V_t}{\cos \varphi} \right)^2 (C_L \cos \varphi + C_d \sin \varphi), \quad \varphi = \arctan \left( \frac{V_n}{V_t} \right). \quad (4.7)$$

where  $c$  is the chord length,  $\rho$  is the air density,  $V_{rel}$  is the magnitude of the resultant local relative velocity of the rotating blade with respect to the flow,  $V_t$  and  $V_n$  are the tangential and normal components of  $V_{rel}$ , respectively, and  $\varphi$  is the angle between resultant relative velocity and the rotation plane.

We approximate  $F_n$  by applying small-angle approximations to the trigonometric functions of  $\varphi$ :

$$F_n \approx \frac{1}{2} c \rho V_t^2 (C_L + C_d \varphi). \quad (4.8)$$

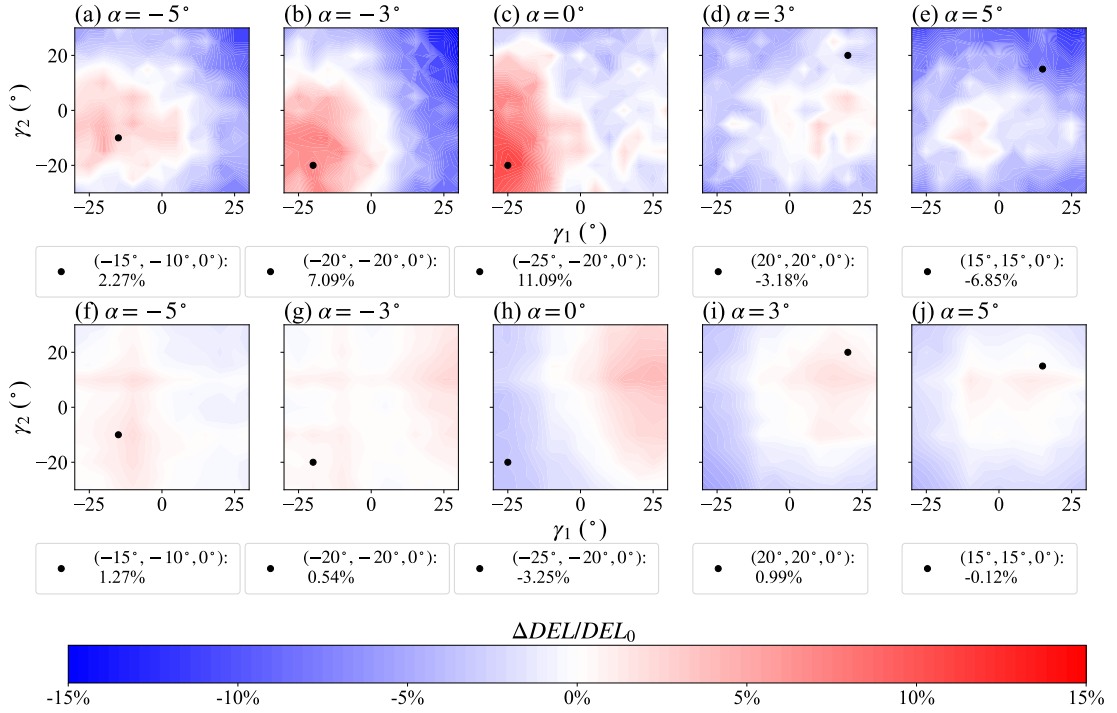


Figure 4.10: Normalised DEL variation contours in the AYC decision space  $\Gamma$  for different inflow angles for (a)-(e) flapwise bending moment; (f)-(j) edgewise bending moment. Black dots show the power-optimal AYC configurations and their corresponding DEL variations.

The approximations of the trigonometric functions can be justified by the fact that the FBM at the blade root is dominated by the flapwise loads acting on the sections near the blade tip. In those sections, the flow angle  $\varphi$ , angle of attack (AoA)  $\alpha$ , and blade twist angle  $\beta$  are small.

According to classical thin-airfoil theory (Anderson, 2011) and the fact that the twist angle  $\beta$  is small, the lift coefficient  $C_L$  of an airfoil in small AoAs can be approximated by:

$$C_L \approx 2\pi\alpha, \quad \alpha = \varphi - \beta \approx \varphi. \quad (4.9)$$

Substituting Eq. 4.9 into Eq. 4.8, we obtain:

$$F_n \approx \frac{1}{2} c \rho V_t^2 (2\pi + C_d) \varphi. \quad (4.10)$$

Since  $C_d \ll 2\pi$  at small AoAs, we neglect the contribution of  $C_d$  and further simplify Eq. 4.10 to:

$$F_n \approx \pi c \rho V_t V_n. \quad (4.11)$$

We find that  $F_n$  is approximately proportional to the product of  $V_t$  and  $V_n$ :

$$F_n \propto V_t V_n. \quad (4.12)$$

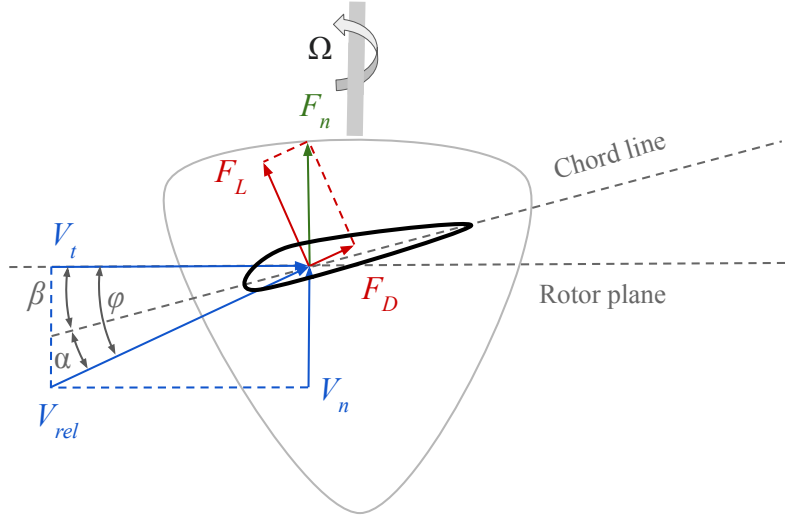


Figure 4.11: Schematic plot of the velocity and force triangles on a rotating wind turbine blade based on the BEM theory (replotted from Burton et al. (2011)).

Therefore, to study the variation of the normal force  $F_n$ , we can focus on the variation of  $V_t V_n$ . Since the tangential induction is very weak in the blade sections close to the tip, we do not take into account the contribution of tangential induction and derive  $V_t$  and  $V_n$  of a yawed turbine according to the BEM theory (Burton et al., 2011):

$$V_n = V_0(\cos \gamma - a), \quad V_t = \Omega r + V_0 \cos \psi (a \tan \frac{\chi}{2} - \sin \gamma). \quad (4.13)$$

where  $V_0$  is the freestream inflow velocity to the turbine,  $\gamma$  is the turbine yaw angle,  $\Omega$  is the turbine rotation speed,  $r$  is the distance of the blade element to the hub,  $\psi$  is the phase angle of the rotating blade,  $\chi$  is the wake skewing angle, and  $a$  is the axial induction factor of the turbine. Glauert (1927) proposed that the axial induction factor  $a$  can be approximated as follows:

$$a = a_0(1 + f(\frac{r}{R})K(\chi) \sin \psi), \quad (4.14)$$

where  $a_0$  is the induction factor of the turbine in non-yawed condition,  $R$  is the radius of the turbine, and  $f$  is the wake expansion function. Øys (1992) proposed the following polynomial fit for  $f$ :

$$f(\frac{r}{R}) = \frac{1}{2}(\frac{r}{R} + 0.4(\frac{r}{R})^3 + 0.4(\frac{r}{R})^5). \quad (4.15)$$

Coleman et al. (1945) proposed that  $K(\chi)$  can be approximated by:

$$K(\chi) = 2 \tan(\frac{\chi}{2}), \quad \chi = (0.6a_0 + 1)\gamma. \quad (4.16)$$

As an example, we consider the  $V_n V_t$  variations in a front-row turbine with  $\gamma_1 = \pm 25^\circ$  at the

blade location  $r = 0.7R$  in a uniform inflow and a vertically sheared inflow. The non-yawed induction factor is assumed to be azimuthally unchanged, and we take the theoretical optimal value predicted by the BEM theory:

$$a_0 = 1/3. \quad (4.17)$$

Figure 4.12 shows the freestream inflow velocity  $V_0$  to the blade section  $r = 0.7R$  at different heights  $z$  and blade phase angles  $\psi$ . We can see that  $V_0$  varies with  $\psi$  in the vertically sheared flow while staying constant in the uniform inflow. When the turbine rotates in the vertically sheared inflow, the azimuthal distributions of the local relative velocity on blade sections in the positively and negatively yawed turbine are different. Figure 4.13 shows the variation of  $V_t V_n$  computed from Eq. 4.13 with respect to  $\psi$  in the two different inflows shown in Figure 4.12. We find that the magnitudes of the variation for the positive and negative yaw angles are the same in the uniform inflow. However, in the vertically sheared inflow, the negative yaw angle leads to a larger variation of  $V_t V_n$  than the positive yaw angle. As a result, according to Eq. 4.16, the negatively yawed turbine experiences a larger variation in the normal thrust force per rotation and, consequently, greater flapwise blade fatigue than the positively yawed one.

Furthermore, applying positive or negative yaw to the upwind turbine also affects the flapwise blade fatigue in its downwind turbine, even if the downwind turbine is not yawed, due to the different wake structures between the positively and negatively yawed turbine. For example, for a non-yawed turbine installed  $7d$  downstream of WT 1 without spanwise offset, the front-view contours of its inflow statistics (normalised mean velocity and turbulence intensity)  $1d$  in front of the downwind turbine are shown in Figure 4.14. The spanwise deflection of the wake of the negatively yawed WT 1 is larger than that of the positively yawed WT 1. As a result, the azimuthal variation of the streamwise inflow velocity for the downwind turbine in the wake of the negatively yawed WT 1 is larger than that in the wake of the positively yawed WT 1. The turbine in the wake of the negatively yawed WT 1 is also exposed to a higher level of streamwise turbulence than that in the wake of the positively yawed WT 1. Therefore, in this configuration, the downwind turbine would endure higher flapwise blade fatigue in the wake of a negatively yawed turbine than in the wake of a positively yawed turbine. The simulation results confirm that the flapwise DEL of the non-yawed WT 2 in the AYC case  $\gamma = (-25^\circ, 0^\circ, 0^\circ)$ ,  $\alpha = 0^\circ$  is 7.7% higher than its counterpart in the AYC case  $\gamma = (25^\circ, 0^\circ, 0^\circ)$ ,  $\alpha = 0^\circ$ .

## 4.5 Summary

This study uses a two-way coupled aeroelastic-LES framework to investigate the power production and blade fatigue of a three-turbine array in the full-wake and partial-wake configurations. The simulations are carried out at discrete decision points of the AYC decision space  $\Gamma$  spanned by the yaw angles of the first two turbines:  $\Gamma = \{\gamma_1 : -30^\circ, -25^\circ, \dots, 25^\circ, 30^\circ\} \times \{\gamma_2 : -30^\circ, -25^\circ, \dots, 25^\circ, 30^\circ\}$ . We extract the time series of the power and the blade bending moments from the simulations and compute the mean power outputs and the blade fatigue loads

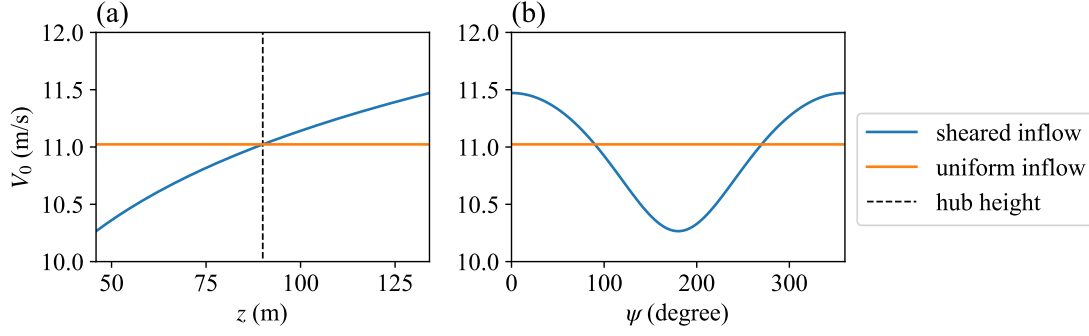


Figure 4.12: Freestream inflow velocity to the turbine blade section  $r = 0.7R$ : (a) at different vertical heights; (b) at different blade phase angles.

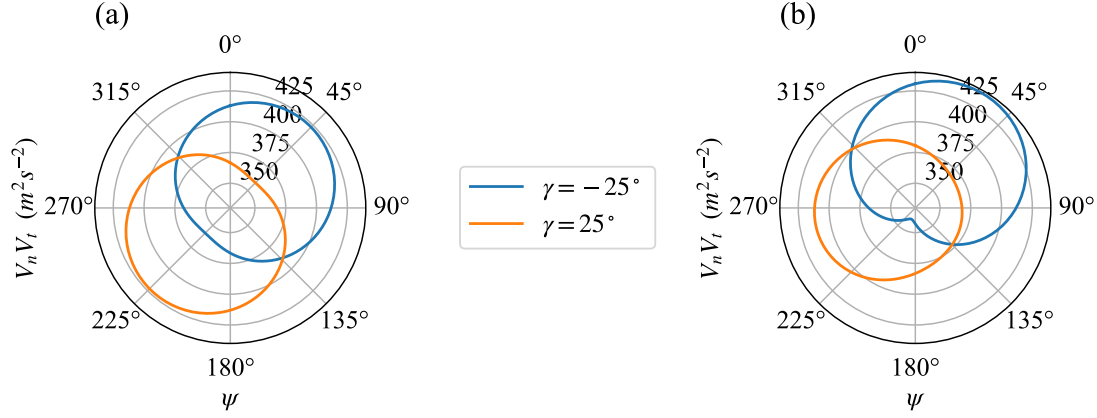


Figure 4.13: Azimuthal variations of  $V_n V_t$  at  $r = 0.7R$  with respect to the blade phase angle  $\psi$  predicted by the BEM theory in (a) a uniform inflow  $u(z) = 11$  m/s; (b) a vertically sheared inflow  $u(z) = \frac{u_*}{\kappa} \log(z/z_0)$ , in which  $u_* = 0.45$  m/s,  $\kappa = 0.4$ , and  $z_0 = 0.005$  m.

of the turbine array.

In the full-wake configuration  $\alpha = 0^\circ$ , we observe two local power optima in the explored AYC decision space  $\Gamma$ : one in the positive quadrant ( $\gamma_1 > 0^\circ, \gamma_2 > 0^\circ$ ) and the other in the negative quadrant ( $\gamma_1 < 0^\circ, \gamma_2 < 0^\circ$ ). The optimal yaw strategy with positive yaw angles yields less power than that with negative yaw angles. We also find that the locally power-optimal positive yaw strategy endures less flapwise blade fatigue and more edgewise blade fatigue than its counterpart with negative yaw angles.

In partial-wake configurations  $|\alpha| = 3^\circ$  and  $5^\circ$ , only one power optimum exists in the explored decision space. Due to the spanwise offset of the turbines, applying optimal AYC achieves larger optimal power gains than that in the full-wake configuration. When the magnitude of  $\alpha$  increases from  $|\alpha| = 3^\circ$  to  $5^\circ$ , the optimal power gains start to decrease, as the non-yawed baseline in this configuration is less affected by wake interference. As for the blade fatigue,

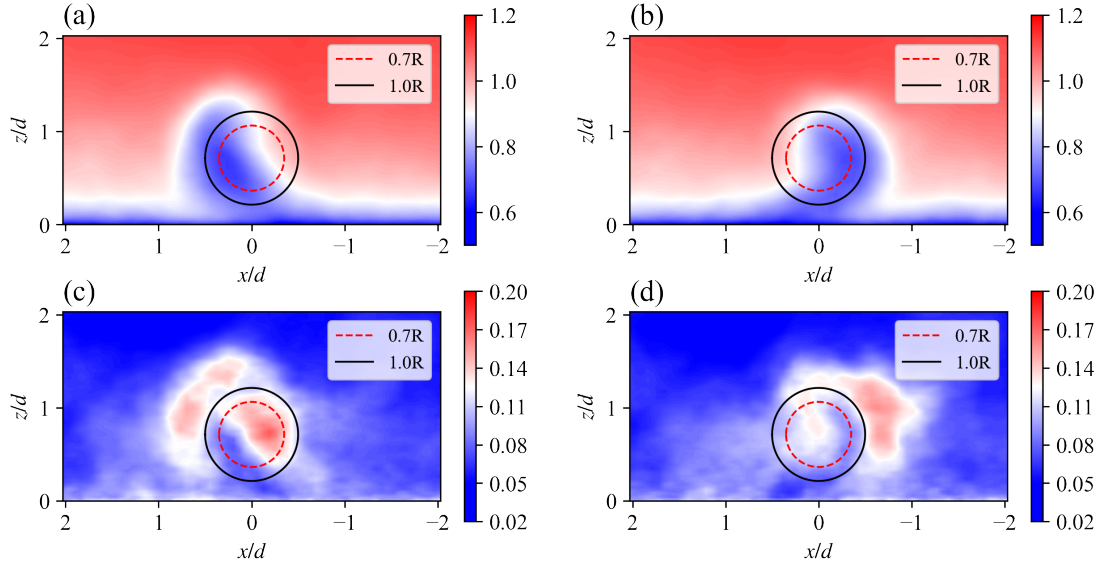


Figure 4.14: Front-view  $y$  -  $z$  cross-section contours of normalised streamwise mean velocity and turbulence intensity  $I_u$  at the location  $6d$  downwind of WT 1: (a)  $\bar{u}/\bar{u}_{hub}$ ,  $\gamma_1 = -25^\circ$ ; (b)  $\bar{u}/\bar{u}_{hub}$ ,  $\gamma_1 = 25^\circ$ ; (c)  $I_u$ ,  $\gamma_1 = -25^\circ$ ; (d)  $I_u$ ,  $\gamma_1 = 25^\circ$ . Black and red circles represent the trajectories of the blade sections  $r = 1.0R$  and  $r = 0.7R$  of the rotating blade, respectively.

when the inflow angle  $\alpha$  is positive, applying the power-optimal yaw strategy in the positive quadrant of the AYC decision space achieves power gains while reducing the flapwise blade fatigue. In contrast, when the inflow angle is negative, the power-optimal strategies with negative yaw angles lead to higher flapwise blade fatigue than the baseline case. Compared with the flapwise fatigue, the variations of the edgewise fatigue to different AYC strategies are less significant in the partial-wake configurations under consideration.

Furthermore, by performing a BEM-based analysis, we reveal that, for the front-row turbine, the aforementioned differences in the flapwise blade fatigue between the positively and negatively yawed turbine are caused by the different azimuthal variations of the local relative velocity on blade sections, which result from the combined effects of vertical wind shear and blade rotation. For the downwind turbine exposed to the wake of the yawed turbine, differences in the flapwise blade fatigue are caused by the different wake deficit and turbulence distributions in the wake of the positively and negatively yawed turbine. These findings highlight that, in the wake modelling of wind turbines subjected to AYC, it is necessary to consider the inflow inhomogeneity and blade rotation, as well as the differences between the wake structures of positively and negatively yawed turbines, particularly when fatigue evaluation is needed from the model.

In future studies, we plan to improve the analytical wake modelling by considering the asymmetry mentioned above of the wake of the positively and negatively yawed turbines. We also plan to develop a computationally cheap optimisation procedure for turbines subjected

to AYC in the full and partial wake conditions based on the improved analytic wake model. Furthermore, we plan to extend the aeroelastic analysis from the blades to other components of wind turbines with finite-element modelling.



## **5 Wake meandering of a wind-turbine array under dynamic yaw control**

### **Abstract**

In this study, we use large-eddy simulation (LES) to investigate the wake-meandering of a wind turbine array under dynamic yaw control (DYC) and the effects on power and fatigue. The wind turbine array consists of eight NREL 5 MW reference turbines. The first turbine in the array is subjected to sinusoidal yaw control with different yaw frequencies. Based on spectral and dynamic-mode-decomposition (DMD) analyses of the flow fields, we find that the wake meandering of the turbine array is significantly amplified when the turbine yaw frequency coincides with the natural wake meandering frequency of the turbine array in the static zero-yaw condition. The resonance of wake meandering accelerates wake recovery and helps the turbine array achieve optimal power production. We also find that the fatigue of the turbine array overall increases with the yaw frequency of the first turbine, highlighting the necessity of jointly considering power production and fatigue when applying DYC.

### 5.1 Introduction

Amid the global challenges of the energy crisis and climate change, wind energy stands out as one of the fastest-growing renewable energy sectors (GWEC, 2022). The main reason for the rapid growth of wind energy is its increasing efficiency, which reduces the cost-per-kilowatt of wind power to a level comparable to traditional fossil-based energy sources (Shen et al., 2020).

Among the various challenges of improving wind energy efficiency, wake interference is a critical issue that has drawn great interest from wind energy developers and researchers. The problem of wake interference arises from the fact that modern wind energy projects are mostly developed in the form of wind farms, with wind turbines installed within designated areas. In certain wind directions, the wakes of the upstream turbines can interfere with the downstream turbines, causing significant losses in power and increases in fatigue (Archer et al., 2018; Barthelmie & Jensen, 2010; Porté-Agel et al., 2020).

To address the issue of wake interference, researchers have explored various solutions, e.g. active yaw control (AYC) (Archer & Vassel-Be-Hagh, 2019; Bastankhah & Porté-Agel, 2016; Bastankhah & Porté-Agel, 2019; Fleming et al., 2014; Howland et al., 2019; Jiménez et al., 2010; Lin & Porté-Agel, 2019; Zong & Porté-Agel, 2021). So far, most of the AYC studies have focused on *static* strategies, i.e., adopting constant yaw angles to redirect wakes from downwind turbines when the mean incoming wind direction and speed are unchanged. Recently, there has been a new push in the research community regarding the potential of applying *dynamic* strategies to achieve power maximisation in wind farms. Munters and Meyers (2017) explored the potential of applying dynamic induction control (DIC) to optimise the power output of a wind farm with adjoint numerical simulations. Later, Munters and Meyers (2018b) analysed the wake behaviour of wind turbines under sinusoidal induction control. They found that the application of dynamic control accelerated the breakup of coherent flow structures behind turbines and enhanced wake recovery. This observation was further confirmed in the wind-tunnel studies carried out by Houck and Cowen (2019) and Frederik et al. Frederik, Weber, et al. (2020). In a follow-up study, Frederik, Doekemeijer, et al. (2020) proposed a dynamic pitch control strategy that enhances wake mixing while avoiding large variations in thrust and power as in DIC. Frederik and van Wingerden (2022) also evaluated the impact of applying periodic induction control on the fatigue loads endured by turbine structures.

In addition to DIC, Munters and Meyers (2018c) explored the application of dynamic yaw control (DYC) in wind farms using numerical simulations and showed the potential to achieve power gains through the DYC strategy. Kimura et al. (2019) studied forced wake meandering behind a stand-alone wind turbine under sinusoidal DYC and observed an early breakdown of coherent structures and an accelerated wake recovery. In a context different from DYC for power maximisation, Z. Li et al. (2022) also observed the forced meandering and accelerated recovery of the wake behind a stand-alone floating wind turbine under wave-induced side-to-side motion. Based on the results of large eddy simulation (LES), they showed that when the turbine motion frequency coincides with the natural wake meandering frequency of a

static turbine, far wake meandering can be triggered by a small turbine motion amplitude. Duan and Porté-Agel (2023) conducted a wind tunnel study of an array of miniature wind turbines under DYC. They found that significant power gains can be achieved for the entire array by just applying sinusoidal yaw at the optimal frequency to the first turbine. This finding is consistent with the critical frequency behaviour of forced wake meandering observed in (Z. Li et al., 2022).

To further understand the flow physics of forced wake meandering and its implications for power production and fatigue loading in wind farms under DYC, in this paper we use a two-way coupled LES and aeroelastic solver to study an array of eight NREL 5MW reference turbines under sinusoidal DYC. The rest of this chapter is organised as follows. In Section 5.2, we discuss the numerical simulation framework and configurations applied in this study. In Section 5.3, we present spectral and dynamic-mode-decomposition (DMD) analyses of the flow fields, and evaluate the effects of different yaw frequencies on wind-turbine power production and fatigue. In Section 5.4, we summarise the conclusions drawn from the results of this study and discuss the implications of these results for the application of DYC in wind farms.

## 5.2 Methodology

### 5.2.1 Governing equations and simulation framework

The simulations in this study are carried out using the GPU-accelerated version of the WiRE-LES code (Lin & Porté-Agel, 2022; Lin & Porté-Agel, 2019; Wu & Porté-Agel, 2011), which solves the spatially-filtered, incompressible Navier-Stokes (NS) equations in a ground-fixed reference frame:

$$\frac{\partial \tilde{u}_i}{\partial x_i} = 0, \quad (5.1)$$

$$\frac{\partial \tilde{u}_i}{\partial t} + \tilde{u}_j \left( \frac{\partial \tilde{u}_i}{\partial x_j} - \frac{\partial \tilde{u}_j}{\partial x_i} \right) = -\frac{\partial \tilde{p}^*}{\partial x_i} - \frac{\partial \tau_{ij}}{\partial x_j} + \frac{F_p}{\rho} \delta_{i1} - \frac{\tilde{f}_i}{\rho}. \quad (5.2)$$

The subscript  $i$  takes the value  $i = 1, 2, 3$  and represents the streamwise, spanwise and vertical directions, respectively;  $\tilde{u}_i$  represents the spatial-filtered velocity of the flow;  $\tilde{p}^*$  represents the modified kinematic pressure,  $F_p$  is the pressure gradient imposed to drive the flow;  $\tau_{ij} = \widetilde{u_i u_j} - \tilde{u}_i \tilde{u}_j$  represents the kinematic sub-grid scale stress modelled by the modulated gradient model (Lu & Porté-Agel, 2010);  $\tilde{f}_i$  are the forces applied by the turbine blades, the nacelle, and the tower on the flow.

The structural deformations of the wind turbine blades are obtained by solving the dynamic

Euler-Bernoulli equations (Meng et al., 2018) in a blade-following rotating reference frame:

$$\frac{\partial^2 q_k}{\partial t^2} + \frac{1}{\mu} \frac{\partial^2 M_k}{\partial r^2} = \frac{1}{\mu} \frac{\partial}{\partial r} \left( \int_r^R \mu \omega^2 r dr \frac{\partial q_k}{\partial r} \right) + g_k + \frac{\hat{f}_k}{\mu}, \quad (5.3)$$

$$M_k = K_{kl} \frac{\partial^2 q_n}{\partial r^2}. \quad (5.4)$$

The subscript  $k$  takes the value of  $k = 1, 2$  and represents the flapwise and edgewise directions of the blade, respectively;  $r$  represents the distance between the blade element and the hub centre;  $q_k$  and  $M_k$  represent the deformation and the bending moment of the blade, respectively;  $g_k$  represents the component of gravitational acceleration projected onto the  $k$ th direction of the blade;  $\mu$  represents the blade mass density;  $\omega$  is the turbine rotational speed;  $K_{kl}$  represents the stiffness matrix of the blade section;  $\hat{f}_k$  is the aerodynamic load exerted by the flow on the blade.

During the simulations, the flow solver for Eqs. 5.1 and 5.2 is two-way coupled with the structural solver for Eqs. 5.3 and 5.4 using the framework of the elastic actuator line model (EALM) proposed by Meng et al. (2018). A more detailed description of the coupling procedure and numerical methods used to solve the governing equations can be found in Lin and Porté-Agel (2023).

### 5.2.2 Simulation case setup

The simulation domain ( $L_x \times L_y \times L_z = 8192 \text{ m} \times 1024 \text{ m} \times 1024 \text{ m}$ ) used in this study is shown in Figure 5.1. It is discretised into a uniform grid with  $1024 \times 128 \times 512$  nodes in  $x$ ,  $y$  and  $z$  directions, respectively.

An array of eight NREL 5 MW wind turbines is placed along the centre-line of the simulation domain, with a distance of  $7d$  between each turbine. The turbine diameter  $d = 126 \text{ m}$ , and the hub height  $z_{hub} = 90 \text{ m}$ . A more detailed description of the design parameters of the NREL 5

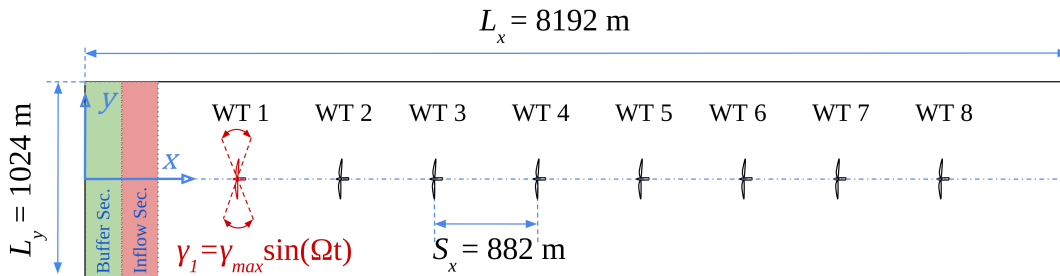


Figure 5.1: Top-view of the simulation domain and the wind turbine array (not to scale).

MW reference wind turbine can be found in Jonkman et al. (2009). In the simulations with DYC, the first wind turbine in the array is subjected to sinusoidal yaw control:

$$\gamma_1 = \gamma_{max} \sin(\Omega t), \quad \Omega = 2\pi f_{yaw}, \quad (5.5)$$

where  $\gamma_{max}$  is the magnitude of the yaw angle, and  $f_{yaw}$  is the frequency of the periodic yaw control. Duan and Porté-Agel (2023) have found that increasing  $\gamma_{max}$  have positive effects on the power output of the turbine array. However, it can be difficult for the yaw mechanism of a utility-scale turbine to reach the intended yaw frequency  $f_{yaw}$  with a large  $\gamma_{max}$ . Therefore, in this study, we choose  $\gamma_{max} = 10^\circ$  for all cases under consideration and focus our investigation on the influence of the yaw frequency  $f_{yaw}$ . The yaw frequency  $f_{yaw}$  varies from 0 Hz to 0.016 Hz in the simulations.

The top boundary of the simulation domain is set to be a frictionless wall. At the bottom boundary, a rough wall condition is set with specified wall shear stresses based on the logarithmic law of the wall. The friction velocity  $u_* = 0.38 \text{ m s}^{-1}$  and the roughness length  $z_0 = 0.005 \text{ m}$ . Periodic boundary conditions are applied to the lateral boundaries of the domain. A precursor simulation without the wind turbine array is performed to generate the inflow, which is then imposed at the inflow section of the domain of the main simulation with wind turbines. A buffer section is added in front of the inflow section to enforce the periodic condition and smoothly transform the recycled flow to the inflow generated by the precursor simulation (Figure 5.1). At 90 m above the ground (turbine hub height), the mean stream inflow velocity  $\bar{u}_{hub}$  is  $9.6 \text{ m s}^{-1}$ , and the streamwise inflow turbulence intensity  $I_u$  is 8%. The simulation time step is 0.02 s and the total simulation time is 2000 s. The results presented in the following sections are extracted from 200 s to 2000 s of the simulation.

## 5.3 Simulation results

### 5.3.1 Wake meandering in the turbine array

Wake meandering refers to the large-scale lateral and vertical movements of the wake behind a wind turbine (Baker & Walker, 1984; Taylor et al., 1985). Wind energy researchers have mainly proposed two explanations for the onset of wake meandering: the disturbance of inflow turbulence (Braunbehrens & Segalini, 2019; Brugger et al., 2022; Espana et al., 2012; Larsen et al., 2008; Muller et al., 2015) and the intrinsic shear instability of the wake (Gupta & Wan, 2019; Iungo et al., 2013; Kang et al., 2014; Medici & Alfredsson, 2006; Yang & Sotiropoulos, 2019) (Figure 5.2). In the configuration of a row of eight turbines considered in this study, most turbines are exposed to the highly turbulent wakes of their upstream counterparts, and the wake meandering is strongly affected by the inflow is strongly affected by disturbance of inflow turbulence. Since DYC mainly affects the lateral movement of the wake, in this study we focus on the lateral wake meandering on the horizontal  $x$ - $y$  plane at the hub height.

Figure 5.3 shows the time-averaged and instantaneous contours of the streamwise velocity at

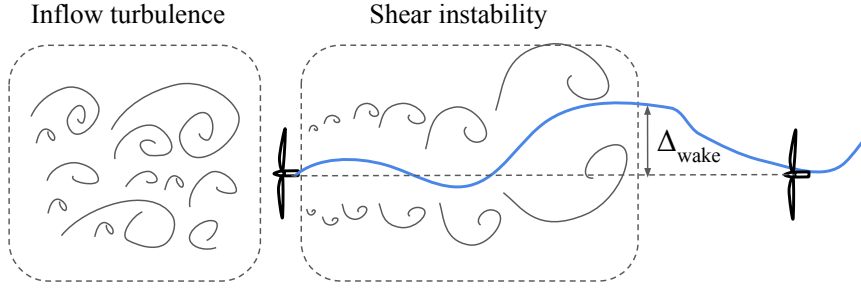


Figure 5.2: Schematic plot of the mechanisms of wake meandering behind a wind turbine. The blue line represents the trajectory of the maximum velocity deficit in the wake.

the hub height ( $z = 90$  m) in the static zero-yaw baseline case. The trajectories of the maximum velocity deficit are marked in black dotted lines, and the centre-line of the turbine array is marked in black dashed lines. While the maximum deficit trajectory in the mean velocity field is largely aligned with the domain centre-line, its counterpart in the instantaneous velocity field is oscillatory, demonstrating the meandering behaviour of the wake.

### 5.3.2 Space-time dynamics of the maximum wake deficit trajectory

To visualise the oscillation of the maximum wake deficit trajectory over time, in Figure 5.4 we show the space-time plots of the lateral displacements of the maximum wake deficit trajectory from the domain centre-line in (a) the static baseline case; (b) the case where the first turbine is periodically yawed ( $\gamma_{max} = 10^\circ$ ,  $f_{yaw} = 0.01$  Hz). The space-time plots demonstrate the dynamics of the maximum wake deficit trajectory. Firstly, in Figure 5.4, we observe a pattern of inclined streaks, which reflects the advection of wake deficits from upstream to downstream. The slope of the streaks reflects the wake advection velocity and is largely unchanged.

Furthermore, the quasi-cyclic pattern of the negative displacement (blue) and positive displacement (red) patterns in Figure 5.4 reveals the behaviour of wake meandering. We observe that the wake meandering is amplified as it propagates in the turbine array. By comparing Figure 5.4a and Figure 5.4b, we can also see that the application of DYC to the first turbine significantly enhances the wake meandering in the wind turbine array, particularly for the turbines near the rear of the array (WTs 5-8). The long-range influence of DYC shown in Figure 5.4 can be explained by the fact that the meandering motion of the wake behind a turbine will affect the wake meandering of the next turbine, consecutively affecting the turbines further downstream, triggering a cascading effect in the wind turbine array.

### 5.3.3 Power spectrum analysis of the velocity signals

After qualitatively illustrating the characteristics of wake meandering, here we investigate this phenomenon in a more quantitative manner. Table 5.1 summarises the configurations of four representative cases selected to study.

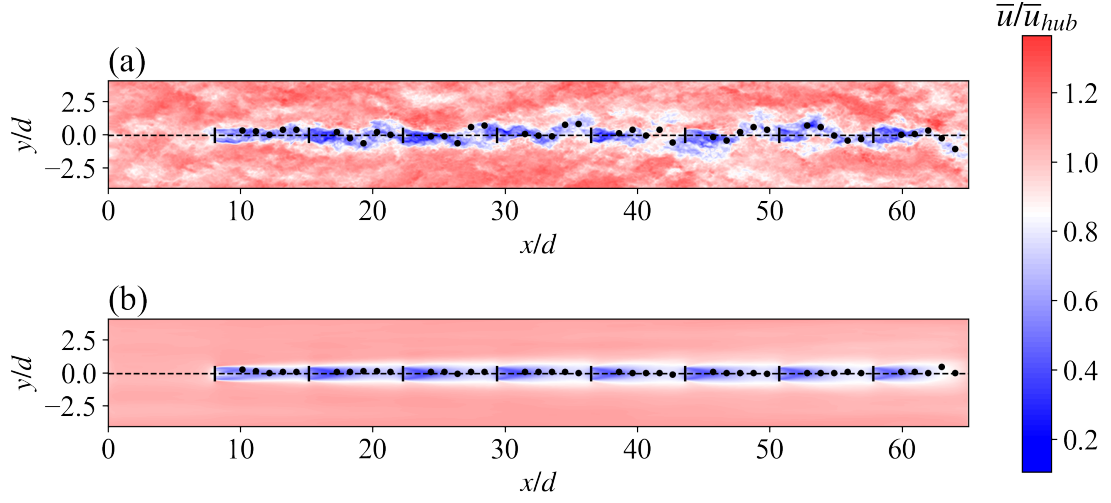


Figure 5.3: Instantaneous (a) and time-averaged (b) contours of the streamwise velocity at the hub height  $z = 90$  m in the static zero-yaw baseline case. The black dotted lines represent trajectories of the maximum  $u$  deficit in the wakes. The black dashed line represents the centre-line of the turbine array.

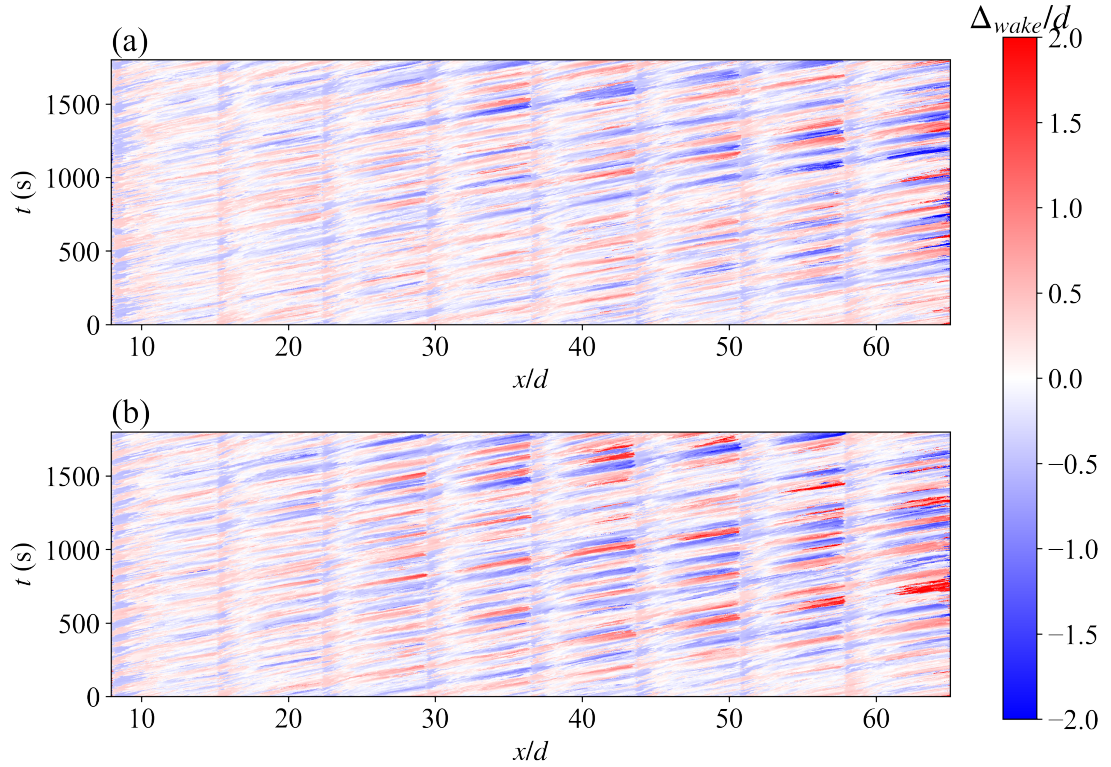


Figure 5.4: Space-time plots of the lateral displacement of maximum velocity deficit locations normalised by the turbine diameter  $\Delta_{wake}/d$ : (a) Zero-yaw baseline case  $\gamma_{max} = 0^\circ$ ,  $f_{yaw} = 0$  Hz; (b) DYC case  $\gamma_{max} = 10^\circ$ ,  $f_{yaw} = 0.01$  Hz.

Table 5.1: Configurations of the four simulation cases.

Case	Condition	$\gamma_{max}$ (°)	$f_{yaw}$ (Hz)
(a)	Static zero-yaw baseline	0	0
(b)	Slow yaw	10	0.004
(c)	Moderate yaw	10	0.01
(d)	Fast yaw	10	0.016

In each case, we sample the hub-height lateral velocity component  $v$  at the points located 6D downstream of each turbine along the centre-line of the array. We then perform the Fast Fourier Transform (FFT) to the sampled time series and compute their power spectrum densities (PSDs). The results are shown in Figure 5.5. In the static baseline case (a), there is no significant peak in the PSD of the sampled velocity behind WT 1. From WT 3 a peak begins to emerge around the frequency 0.01 Hz. In the three yawed cases (b), (c) and (d), there are significant peaks at their respective yaw frequencies in the PSD of the sampled velocity behind WT 1, indicating the dominant forced wake meandering induced by the periodic yaw of WT 1. However, for the downstream turbines, only the moderate yaw case (b), with its yaw frequency of 0.01 Hz coinciding with the wake meandering frequency observed in the baseline case (a), maintains the dominance of the wake meandering motion at the yaw frequency of WT 1.

### 5.3.4 Dynamic mode decomposition (DMD) analysis

The results in Figure 5.4 and Figure 5.5 suggest that the wake meandering in the wind turbine array under DYC exhibits a resonance behaviour. To further reveal the spatial-temporal characteristics of such a system, we adopt a tool that is widely used in the data-driven analysis of dynamical systems: dynamic mode decomposition (DMD) (Schmid, 2010).

DMD decomposes the flow field  $\mathbf{u}(\mathbf{x}, t)$  as in Eq. 5.6:

$$\mathbf{u}(\mathbf{x}, t) \approx \sum_{k=1}^n \underbrace{\boldsymbol{\phi}_k(\mathbf{x})}_{\text{spatial modes}} \overbrace{\exp(\omega_k t) b_k}^{\text{time dynamics}} = \sum_{k=1}^n \boldsymbol{\phi}_k(\mathbf{x}) \lambda_k^{(t/\Delta t)} b_k, \quad (5.6)$$

where  $\boldsymbol{\phi}_k(\mathbf{x})$  is the  $k$ th spatial mode of the flow fields,  $\lambda_k$  and  $b_k$  are the  $k$ th eigenvalue and amplitude coefficient associated with the  $k$ th spatial mode, respectively, and  $\Delta t$  is the time step between two snapshots of the flow field. The detailed DMD algorithm for calculating each term in Eq. 5.6 from the data can be found in Appendix A. As an example, Figure 5.6 shows the first 15 spatial modes and associated time dynamics extracted from the DMD analysis on the dataset containing 900 snapshots of the hub-height lateral velocity field  $v$  in the static zero-yaw baseline case. The time step between two snapshots is 2 s.

In the time dynamics extracted from the DMD, the frequencies are determined by the phase angle of the complex eigenvalues  $\lambda_k$ , and the amplitudes are determined by the amplitude coefficient  $b_k$ . The one-to-one mapping of the frequency and the amplitude gives us another



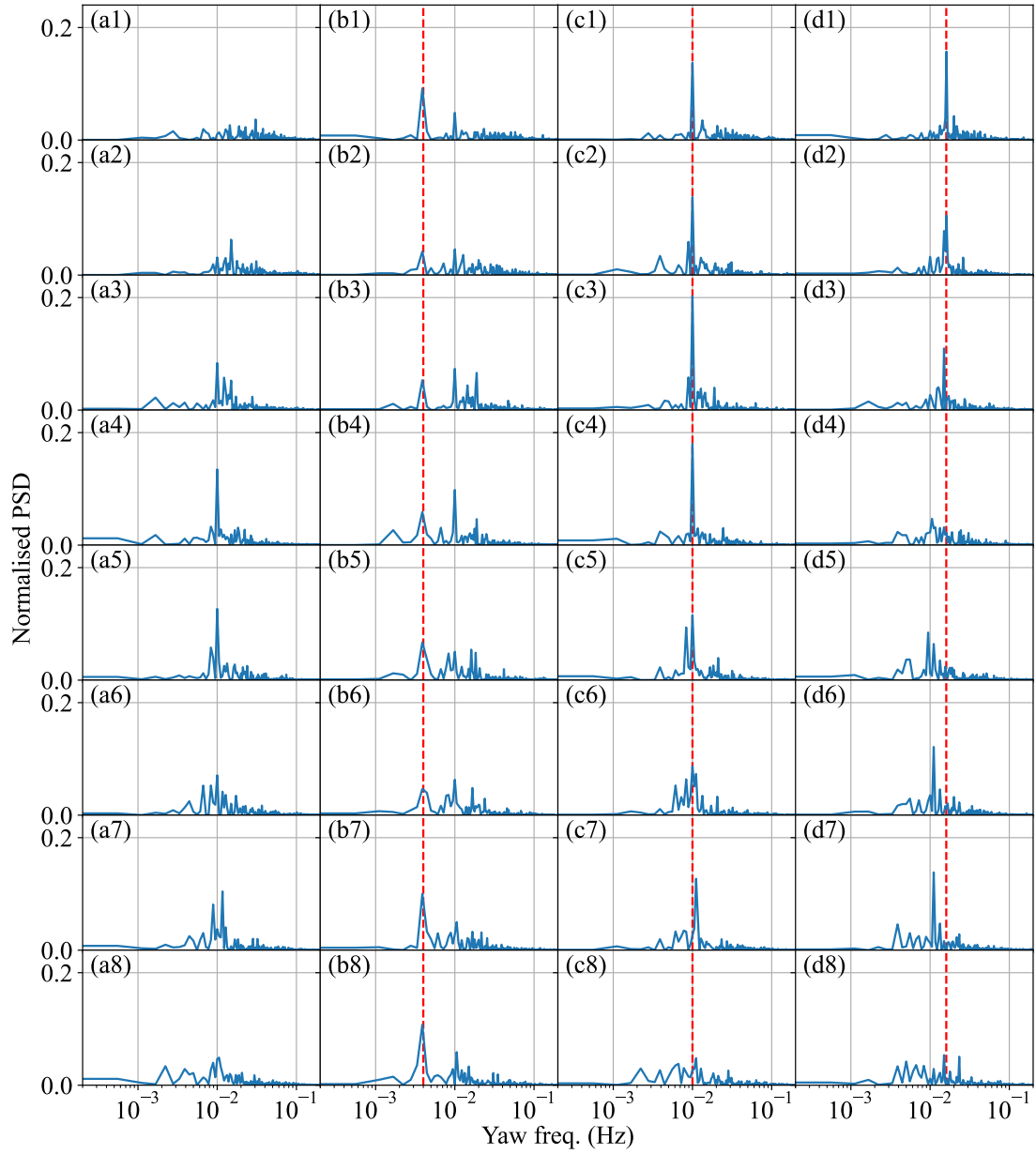


Figure 5.5: Normalised power spectrum density (PSD) plots of lateral velocity component  $v$  sampled at 6D downstream of each turbine. The red dashed lines mark the yaw frequency in different cases: (a1) - (a8) Static zero-yaw baseline  $f_{yaw} = 0$  Hz; (b1) - (b8) Slow yaw  $f_{yaw} = 0.004$  Hz; (c1) - (c8) moderate yaw  $f_{yaw} = 0.01$  Hz; (d1) - (d8) fast yaw  $f_{yaw} = 0.016$  Hz.

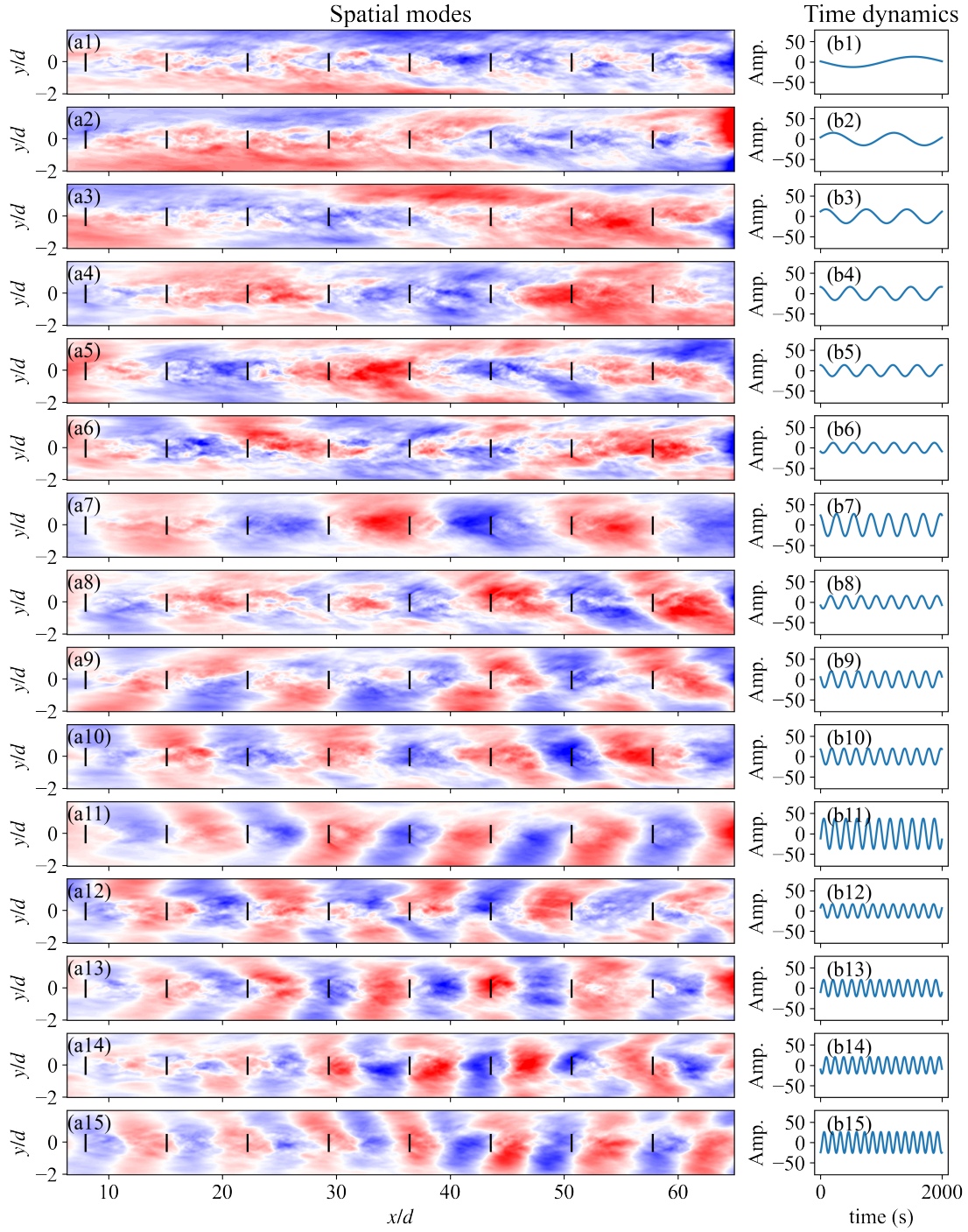


Figure 5.6: First 15 DMD components (redundant conjugated components removed) of the lateral velocity  $v$  in the static zero-yaw baseline case: (a) spatial modes; (b) associated time dynamics.

way to reveal the resonance behaviour of the wake meandering in the wind turbine array under DYC in the spectral space. Figure 5.7 shows the plots of mode amplitude coefficient vs mode frequency extracted from the DMD of the hub-height lateral velocity  $v$  in different DYC configurations. In the static baseline case (a), we observe a peak at the frequency 0.01 Hz as in the PSD plots in Figure 5.5, indicating a natural wake meandering frequency in the wind turbine array. In the DYC cases (b) - (d), there is another peak associated with the yaw frequency of WT 1. The highest peak of the amplitude coefficient is found in case (c), where the yaw frequency coincides with the natural meandering frequency.

Another important one-to-one mapping of the DMD components is the one between the spatial mode and the mode frequency. In the study of a wind turbine array under periodic yaw, the selection of mode frequency is obvious: in the static baseline, we focus on the spatial mode associated with the natural wake meandering frequency (0.01 Hz in this case); in the yawed case, we focus on the spatial mode associated with the frequency of the periodic yaw.

Figure 5.8 shows the contours of the selected DMD spatial modes of the hub-height lateral velocity  $v$  in different cases. The alternating pattern of positive (red) and negative (blue) magnitude in the contours evidently reveals that the underlying dynamics of the natural and forced wake meandering within the wind turbine array is similar to a travelling wave. At the natural meandering frequency, the wavelength of the wake meandering is approximately equal to the distance between two turbines (Figure 5.8a). When the first turbine is under periodic DYC, the wavelength of the forced wake meandering decreases with the increases in the yaw frequency. In the slow yaw case (Figure 5.8b), the wake magnitude of the associated spatial mode is small; in the fast yaw case (Figure 5.8d), the forced wake meandering is attenuated within a short range; In the case where the yaw frequency coincides with the natural meandering frequency (Figure 5.8c), the wake meandering is largely maintained within the wind turbine array.

### 5.3.5 Streamwise profiles of the wake flow statistics

The results presented in the previous sections reveal that applying a suitable yaw frequency to the first turbine can trigger wake-meandering resonance in the wind turbine array. It is natural to further explore its impact on the wake flow statistics. Figure 5.9 shows the profiles of normalised streamwise mean velocity  $\bar{u}/\bar{u}_{hub}$  and turbulence intensity  $I_u$  averaged within the projections of turbine rotors on the  $y$ - $z$  plane at different streamwise locations. We can see that the fast yaw case initially has a faster wake recovery than the other two cases behind WTs 1 and 2. From WT 3, the wake recovery of the fast yaw case is surpassed by that of the moderate yaw case. A similar trend is found in the streamwise turbulence intensity profiles: behind WTs 1 and 2, the locations of the highest  $I_u$  peaks are found in the fast yaw case, and from WTs 3 to 8, they are found in the moderate yaw case.

The aforementioned results of flow statistics show that the forced wake meandering enhances the turbulent mixing behind the turbine and accelerates the recovery of the wake. Applying a

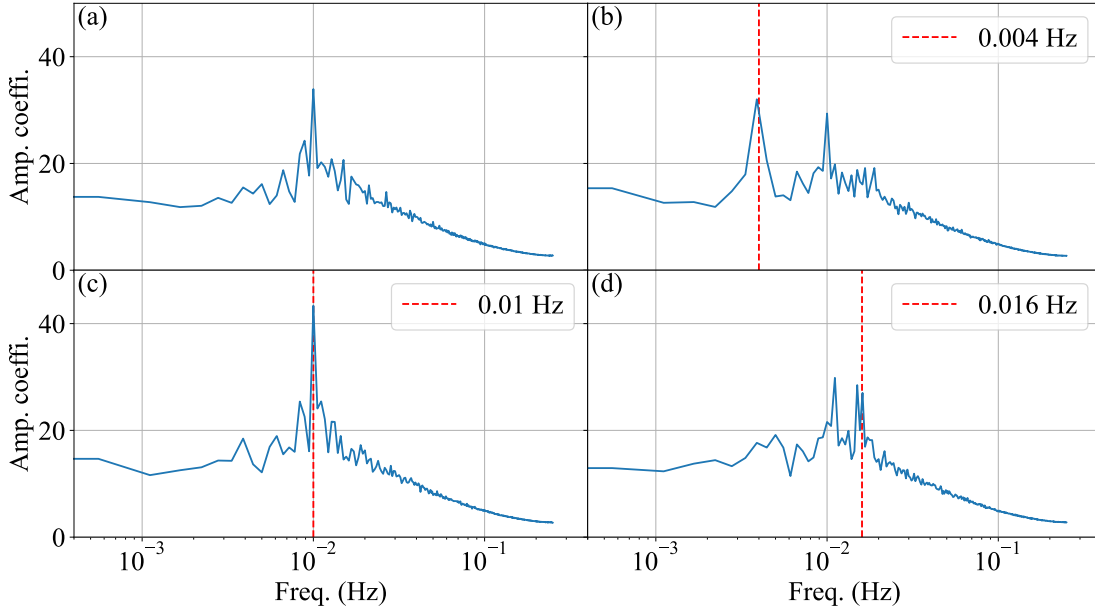


Figure 5.7: Mode amplitude coefficients vs mode frequencies extracted from the DMD of the hub-height lateral velocity  $v$ : (a) static zero-yaw baseline; (b)  $f_{yaw} = 0.004$  Hz; (c)  $f_{yaw} = 0.01$  Hz; (d)  $f_{yaw} = 0.016$  Hz. Red dashed lines represent the yaw frequency.

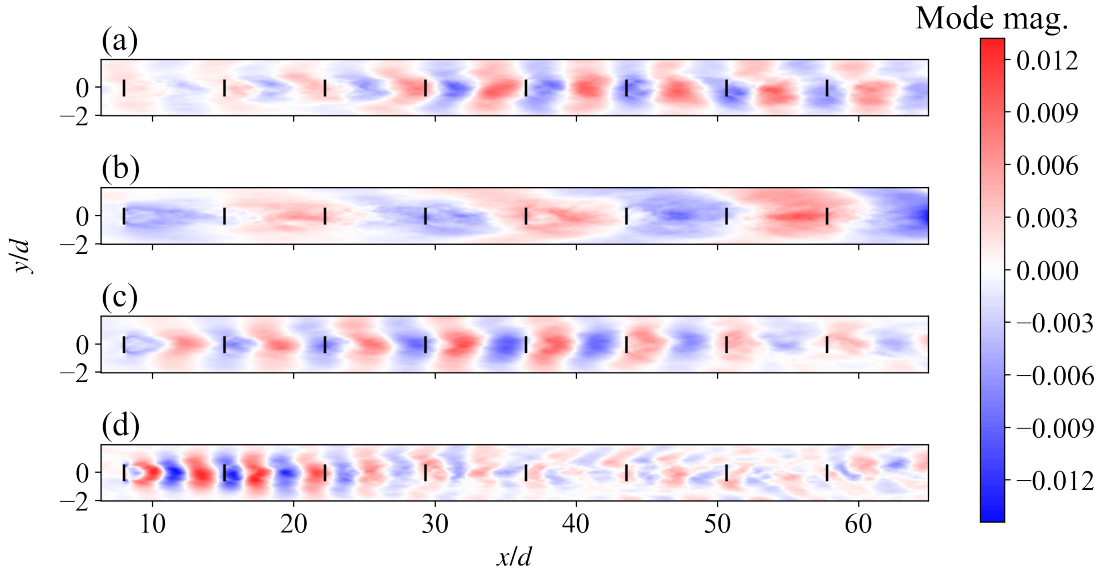


Figure 5.8: Contours of the selected DMD spatial modes of the hub-height lateral velocity  $v$  in difference cases: (a) static zero-yaw baseline  $f_{yaw} = 0$  Hz (b) slow yaw  $f_{yaw} = 0.004$  Hz (c) moderate yaw  $f_{yaw} = 0.01$  Hz (d) fast yaw  $f_{yaw} = 0.016$  Hz. The associated mode frequency in (a) is 0.01 Hz. In (b) - (d), the associated frequencies are the same as the yaw frequencies.

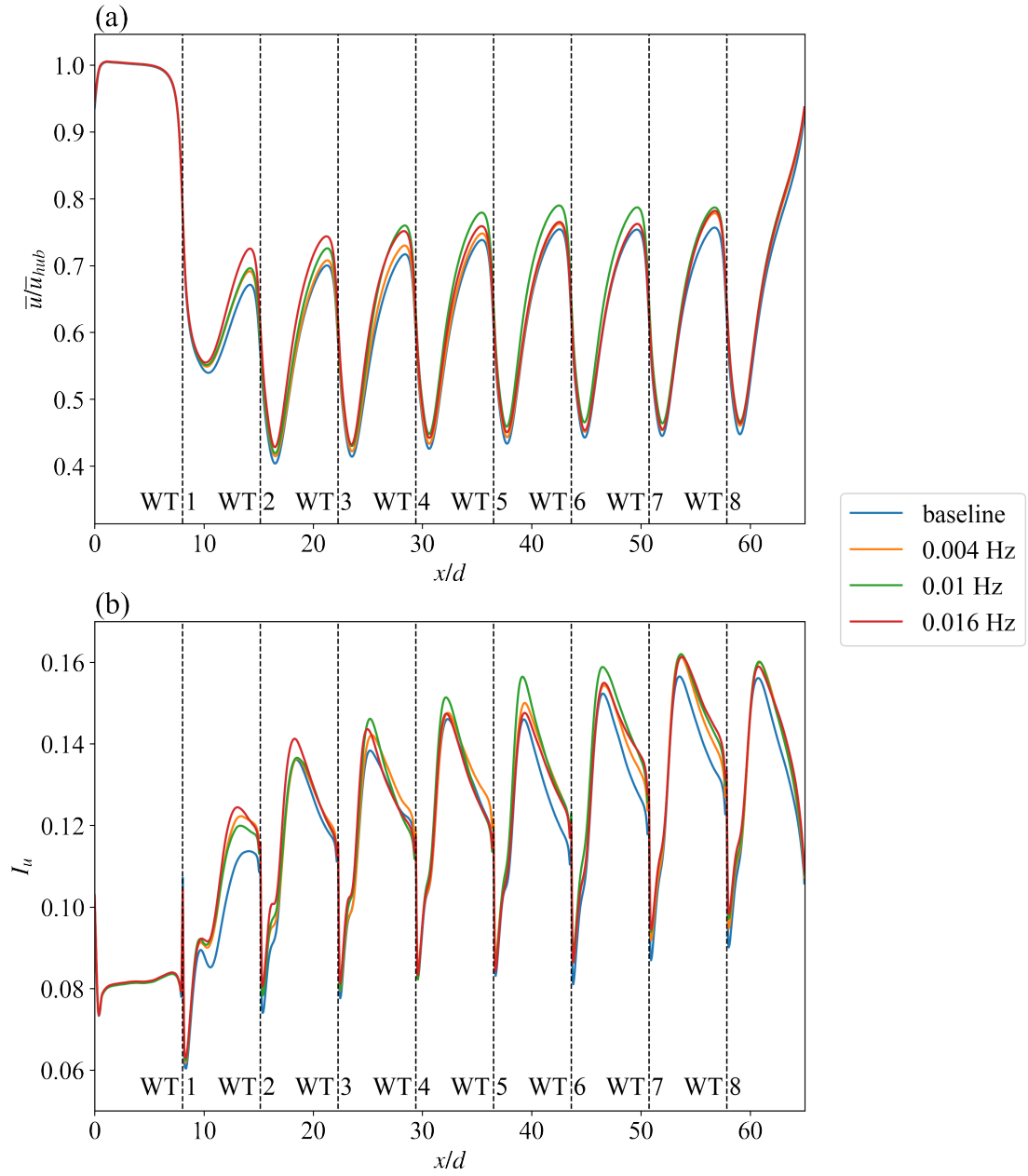


Figure 5.9: Profiles of the flow statistics averaged within the projections of turbine rotors at different streamwise locations: (a) normalised streamwise mean velocity; (b) streamwise turbulence intensity.

high-frequency DYC (0.016 Hz) can only enforce strong wake meandering within a short range to the yawed turbine. On the other hand, the DYC case with a resonating yaw frequency (0.01 Hz) successfully accelerates the wake recovery of the turbines further downstream.

### 5.3.6 Impacts on wind turbine power and fatigue

In this section, we evaluate the impacts of applying different DYC strategies on the power output and fatigue loading of the wind turbine array. Figure 5.10 shows the mean normalised power outputs of each turbine in the wind turbine array. In Figure 5.10a, the power output is normalised by the power of the first turbine in the baseline case  $P_{1,baseline}$ . Due to wake interference, the power outputs of downstream turbines (WTs 2-8) are significantly lower than that of WT 1. To further evaluate the influence of applying different DYC strategies, we normalise the power output of each turbine by their counterpart in the baseline case  $P_{i,baseline}$ , as shown Figure 5.10b. In comparison with the baseline case, the application of DYC slightly decreases the power of the yawed turbine while increases the power outputs of downstream non-yawed turbines due to the accelerated wake recovery triggered by DYC. Similar to the trend of wake recovery shown in Figure 5.9, the fast yaw case ( $f_{yaw} = 0.016$  Hz) yields the largest power gains in the turbines in the vicinity of the yawed turbine, i.e., WTs 2 and 3. However, it is surpassed by the moderate yaw case ( $f_{yaw} = 0.01$  Hz) from WT 5 and the turbines further downstream. The optimal total power gain is achieved when the yaw frequency of WT 1 is 0.01 Hz, which triggers the resonance of the wake meandering within the wind turbine array (Figure 5.11).

In addition to power outputs, fatigue loading is another important factor to consider when applying DYC. In this study, we focus on two types of turbine fatigue damage: the blade-root flapwise fatigue and yaw bearing fatigue at the nacelle, as they are particularly susceptible to the sinusoidal yaw movement of the rotor and nacelle. Fatigue loading is quantified by the damage equivalent load (DEL). Figure 5.12 presents an example of the evaluation of the DEL using the time series of the flapwise blade-root bending moment of WT 1 in the baseline case. The main procedures can be summarised as follows:

- Identify the load reversal points from the load spectrum (Figure 5.12a).
- Apply the rainflow counting algorithm to extract the load cycles from the identified reversal points. The extracted load cycles can be visualised in the form of a rainflow matrix (Figure 5.12b), where the column of the matrix is the starting point of the cycle, and the row is the destination point.
- Obtain the cumulative distribution of the load ranges and calculate the DEL based on the Miner's rule of linear damage accumulation.

Figure 5.13 shows the normalised DELs of the blade-root flapwise bending moment for each turbine in the array. In the static baseline case, we observe a trend of increasing DELs from the

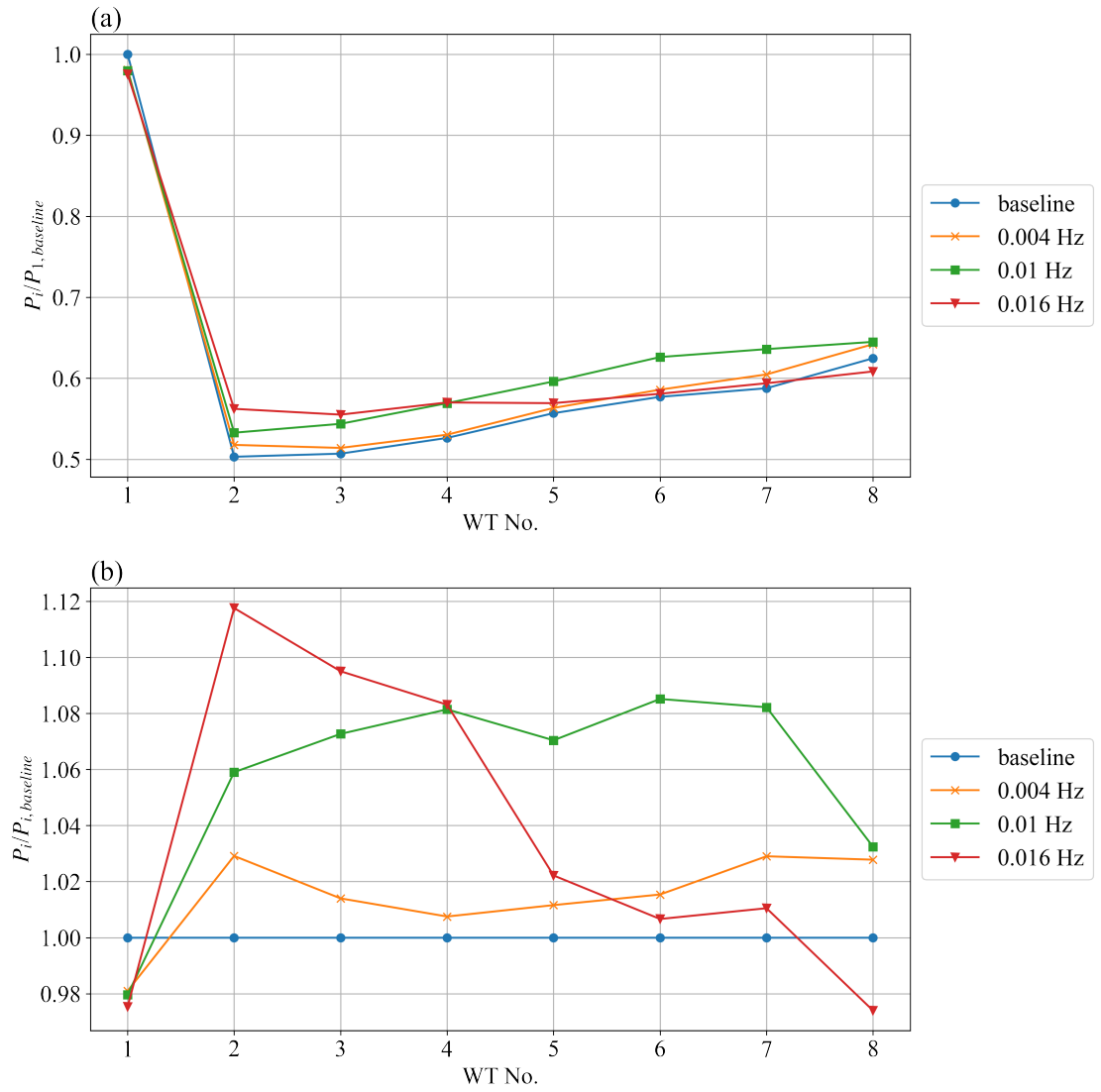


Figure 5.10: Normalised power outputs of each turbine in the array: (a) normalised by the power of the first turbine in the baseline case  $P_{1, \text{baseline}}$ ; (b) normalised by the power of each turbine in the baseline case  $P_{i, \text{baseline}}$ , respectively.

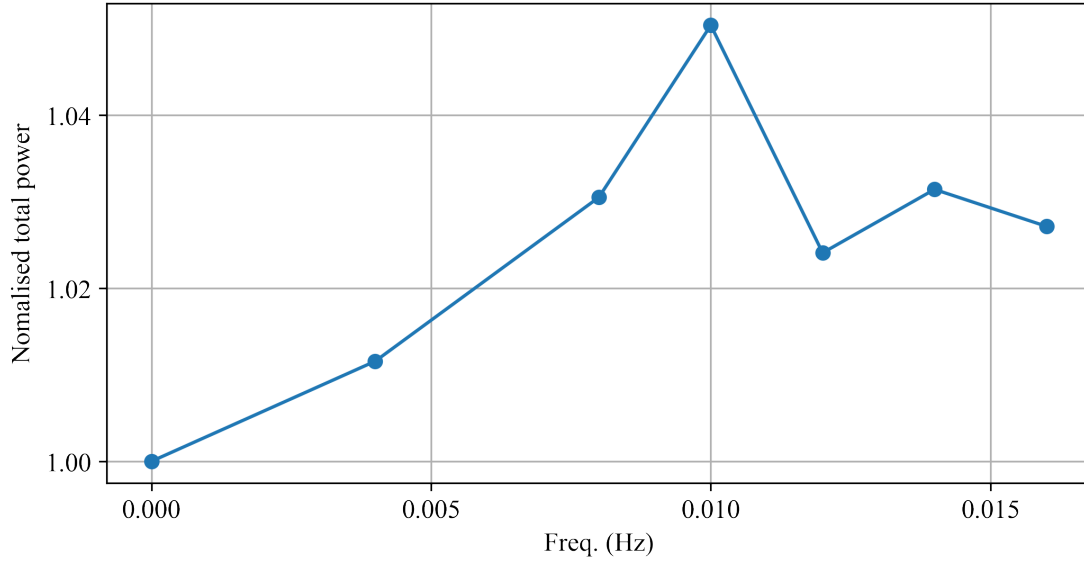


Figure 5.11: Total power outputs of the wind turbine array vs WT 1 yaw frequency  $f_{yaw}$ . The power outputs are normalised by the total power of the static zero-yaw baseline case.

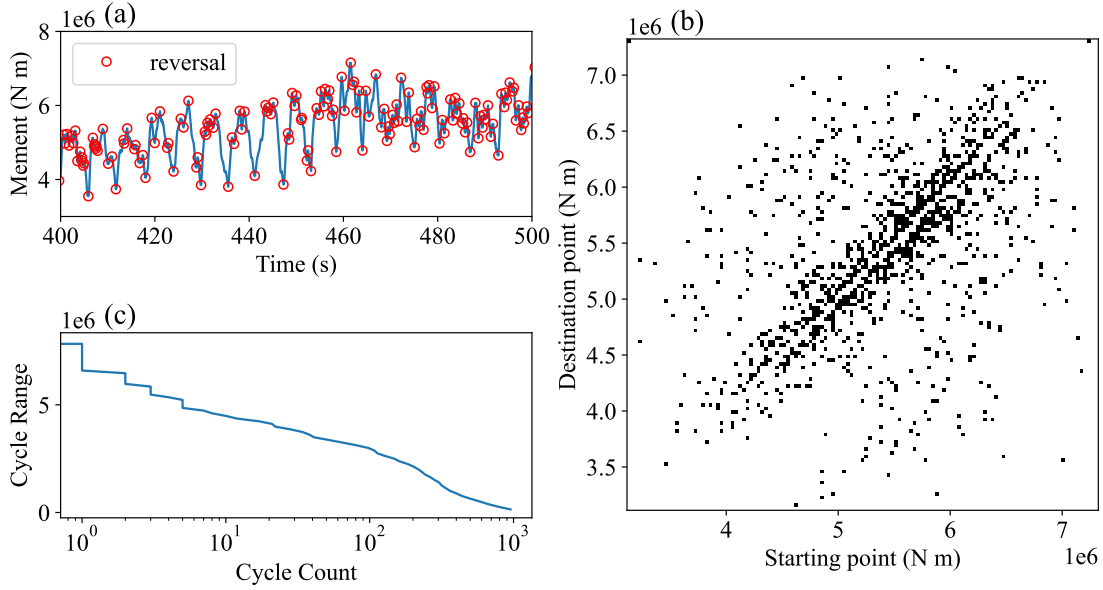


Figure 5.12: Fatigue evaluation using the time series of the flapwise blade-root bending moment of WT 1 in the baseline case: (a) identify the load reversal points; (b) use the rainflow counting algorithm to extract the load cycles and assemble the rainflow matrix; (c) obtain the cumulative distribution of the ranges of load cycles and calculate the DEL using the Miner's rule.



upstream to the downstream turbines, highlighting the wake-induced fatigue in the turbine array. When WT 1 is under DYC, we find that, due to the enhanced wake meandering, the blade fatigue is increased for all the turbines in the array, particularly in the fast yaw case ( $f_{yaw} = 0.016$  Hz), where the blade DEL of the yawed WT 1 is more than 15% higher than that in the baseline case.

Figure 5.14 shows the normalised DELs of the yaw moment at the turbine nacelle for each turbine in the array. In the static baseline case, we find that the downstream turbines endure significantly higher yaw fatigue than the front turbine due to their exposure to the meandering wake. We also observe that the yaw fatigue in WT 1 is more susceptible to the application of DYC than the flapwise blade fatigue. In the fast yaw case, the yaw fatigue in WT 1 is around 35% higher than that in the static baseline case and reaches a fatigue level similar to that of a downstream turbine exposed to the meandering wake.

## **5.4 Summary and conclusions**

This study uses a two-way coupled LES and aeroelastic solver to numerically explore the wake meandering within a wind turbine array under DYC. The wind turbine array comprises eight NREL 5 MW reference wind turbines, and only the first turbine is subjected to sinusoidal yaw control with different frequencies ranging from 0 Hz to 0.016 Hz.

Based on the spectral analysis and the data-driven dynamic mode decomposition of the hub-height flow fields, we observe a dominant natural wake meandering frequency emerging in the static non-yawed baseline, particularly in the wakes of the turbines near the rear of the array. When the front turbine is yawed at the same frequency as the natural wake meandering frequency, the forced wake meandering is significantly amplified in the turbine array. The resonance of wake meandering enhances the mixing of the wake and the outer flow and accelerates the wake recovery in the turbine array. As a result, the case with the resonance yaw frequency for WT 1 yields the optimal total power output. We also find that the flapwise blade fatigue and nacelle yaw fatigue of the turbines overall increase with the yaw frequency of the first turbine, particularly for the nacelle yaw fatigue.

Furthermore, the findings of this study indicate that DYC is more suitable for long wind turbine arrays than short ones, as DYC at a suitable frequency can improve the power outputs of turbines that are far away from the yawed turbine. If the wind turbine array is too short, the wake meandering is not fully developed for DYC to exploit its advantage of long-range influence, and applying DYC may lead to a net power loss in this case.

In future studies, we plan to further explore the theoretical mechanisms of the wake meandering resonance in the wind turbine array under DYC from the aspect of flow stability theory. We also plan to quantify the increased fatigue with a proper cost function so that the power output and fatigue damage can be jointly optimised in wind farms under DYC.

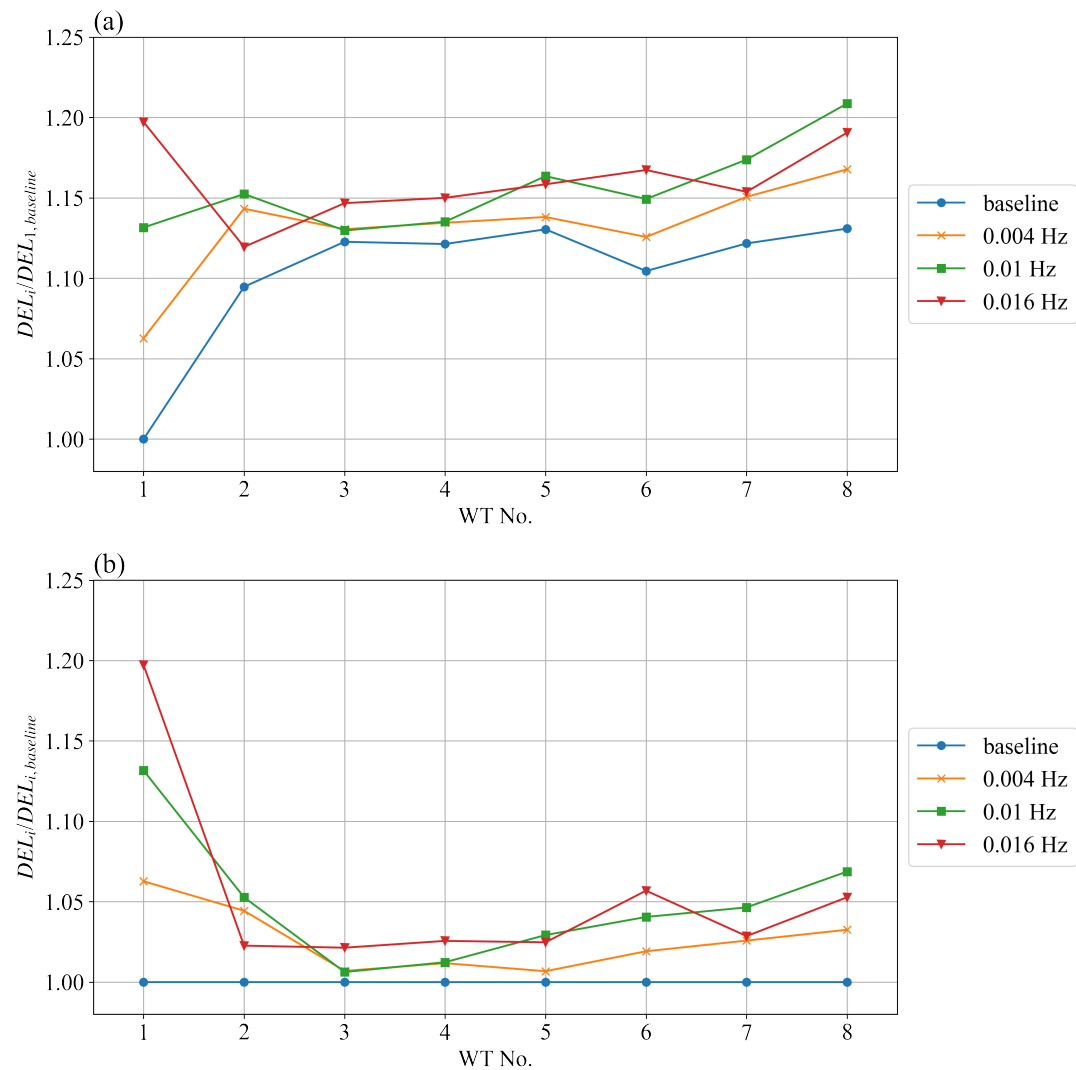


Figure 5.13: Normalised DELs of the blade-root flapwise bending moment for each turbine in the array: (a) normalised by the DEL of the first turbine in the baseline case; (b) normalised by the DEL of each turbine in the baseline case.

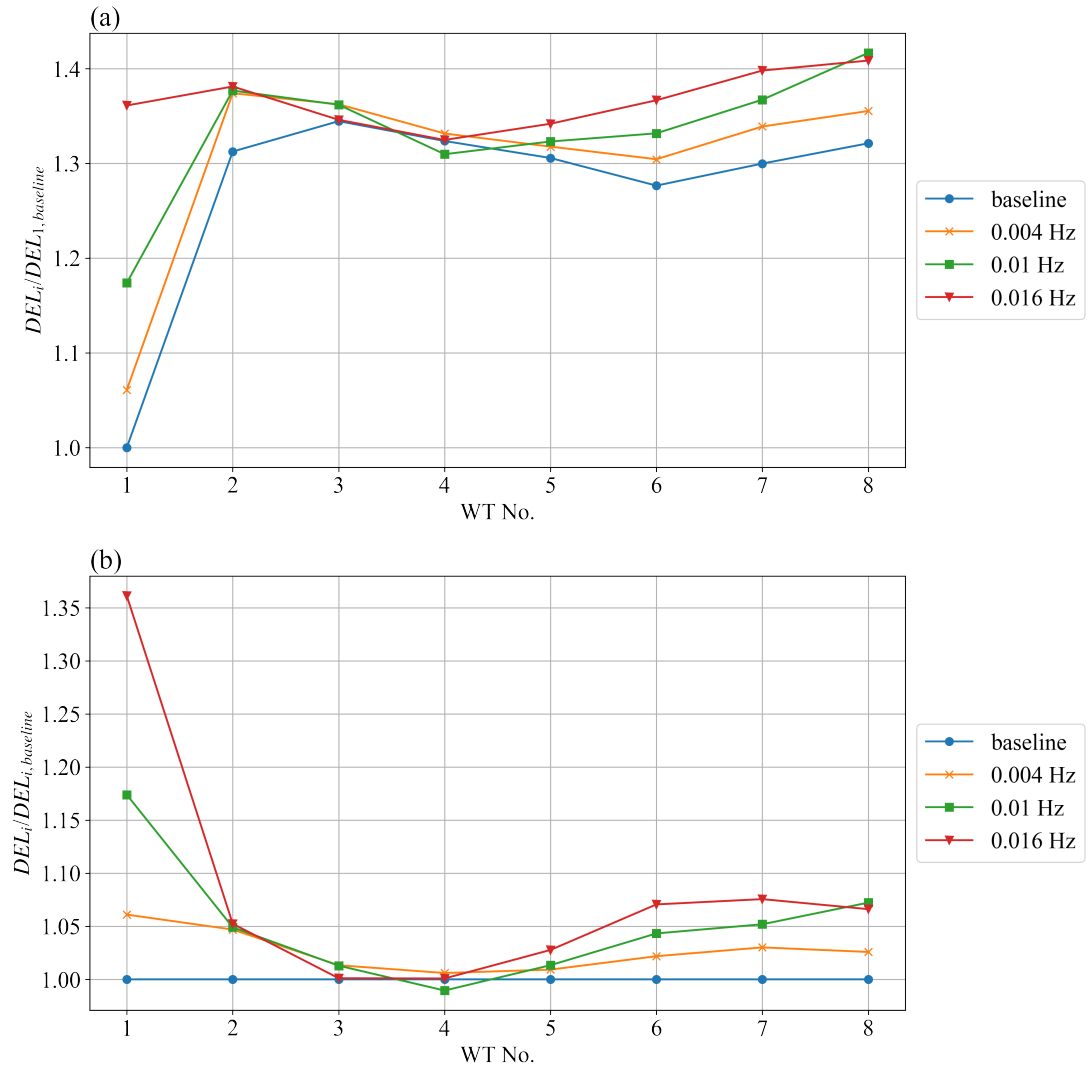


Figure 5.14: Normalised DELs of the nacelle yaw moment for each turbine in the array: (a) normalised by the DEL of the first turbine in the baseline case; (b) normalised by the DEL of each turbine in the baseline case.

## 5.5 Appendix

The algorithm (Schmid, 2010) of applying DMD to a high-dimensional dataset  $\mathbf{u}(\mathbf{x}, t)$  is summarised as follows:

- Reshape the original dataset into an  $m \times n$  matrix  $\mathbf{X}$ , where  $m$  is the total degree of freedom (DOF) of the data in space and  $n$  is the number of snapshots of the system in time (usually  $m \gg n$ ).
- Extract two smaller matrices  $\mathbf{X}'$  and  $\mathbf{X}''$  from  $\mathbf{X}$ , where  $\mathbf{X}'$  takes the first  $n - 1$  columns of  $\mathbf{X}$ , and  $\mathbf{X}''$  takes the last  $n - 1$  columns of  $\mathbf{X}$ .  $\mathbf{X}'$  and  $\mathbf{X}''$  represent two space-time states of the underlying dynamical system with a shift of a single time step.
- Approximate the evolution of the underlying dynamical system from the state  $\mathbf{X}'$  to  $\mathbf{X}''$  with a best-fit linear operator  $\mathbf{A}$ :

$$\mathbf{X}'' \approx \mathbf{A}\mathbf{X}'. \quad (5.7)$$

- Due to the large size of  $\mathbf{X}'$ , it is very expensive to directly compute the pseudo-inverse of  $\mathbf{X}'$ . To circumnavigate this issue, perform the singular value decomposition of  $\mathbf{X}'$ :

$$\mathbf{X}' = \mathbf{U}\Sigma\mathbf{V}^*, \quad (5.8)$$

in which  $\mathbf{U}$  and  $\mathbf{V}$  are both unitary matrices,  $\Sigma$  is a diagonal matrix, and the asterisk symbol  $*$  represents the conjugate transpose. This step is also known as the proper orthogonal decomposition (POD), and  $\mathbf{U}$  is the POD mode of  $\mathbf{X}'$ .

- Construct a new matrix  $\tilde{\mathbf{A}}$ , which is the projection of  $\mathbf{A}$  onto the POD modes  $\mathbf{U}$ :

$$\tilde{\mathbf{A}} = \mathbf{U}^* \mathbf{A} \mathbf{U} = \mathbf{U}^* \mathbf{X}'' \mathbf{V} \Sigma^{-1}. \quad (5.9)$$

The motivation for computing the projection of  $\mathbf{A}$  is that if we truncated the POD modes  $\mathbf{U}$ , the dimension of  $\tilde{\mathbf{A}}$  would also be reduced, and  $\mathbf{A}$  and  $\tilde{\mathbf{A}}$  share the same non-zero eigenvalues. Therefore, it is more efficient to study  $\tilde{\mathbf{A}}$  than study the original matrix  $\mathbf{A}$ .

- Perform the eigenvalue decomposition to the projected matrix  $\tilde{\mathbf{A}}$ :

$$\tilde{\mathbf{A}}\mathbf{W} = \mathbf{W}\Lambda. \quad (5.10)$$

The diagonal elements of the diagonal matrix  $\Lambda$  are the DMD eigenvalues. The DMD modes  $\Phi$  is then reconstructed by

$$\Phi = \mathbf{X}'' \mathbf{V} \Sigma^{-1} \mathbf{W}. \quad (5.11)$$

## 6 Overall summary and future research perspectives

### 6.1 Overall summary

This thesis presents numerical and theoretical studies on the wakes of wind turbines subjected to AYC and the effects of AYC on turbine power production and fatigue. The key elements and findings of these studies are summarised below:

- Study 1: we validate the ADM-BE in LES for a yawed wind turbine by comparing LES results with wind-tunnel measurements. We find that LES using the ADM-BE provides better predictions of the mean streamwise velocity deficit and the streamwise turbulence intensity than using the standard ADM. The ADM-BE also reproduces the interaction between the wake rotation and the CVP in yawed wind turbine wakes. The standard ADM fails to capture such an interaction due to the uniform force distribution and the lack of wake rotation. We also found that the ADM-BE improves the turbine power prediction compared to the standard ADM, which suffers from significant power overestimation compared to wind-tunnel measurements.
- Study 2: we validate an LES framework using three different wind turbine parametrisations (the ADM-std, ADM-BE and ALM) for simulating the flow through a three-turbine array in full-wake and partial-wake conditions. By comparing LES results to wind tunnel measurements, we find that the parametrisations capturing the local force distribution of the turbine (the ADM-BE and ALM) yield better predictions of wake flow statistics than the ADM-std, particularly in partial wake conditions. This is caused by the fact that the ADM-std fails to capture the non-uniform force distribution experienced by the rotor. We also found that the ADM-BE yields overall better power predictions than the ADM-std and the ALM in the cases considered in this study.
- Study 3: using a two-way coupled aeroelastic-LES framework, we investigate the power and blade fatigue of a turbine array. We find that, when the turbine array is in full-wake condition, the locally optimal AYC strategy for power with positive yaw angles endures less flapwise blade fatigue and more edgewise blade fatigue than the global optimal

strategy with negative yaw angles. In partial-wake conditions, when the inflow angle  $\alpha$  is positive, applying the power-optimal yaw strategy with positive yaw angles achieves power gains while reducing the flapwise blade fatigue. In contrast, when the inflow angle is negative, the power-optimal strategies with negative yaw angles lead to higher flapwise blade fatigue than the baseline case. Furthermore, for the front-row turbine, we reveal that the different flapwise blade fatigue between the positively and negatively yawed turbine is due to the difference in the azimuthal variations of the local relative velocity on blade sections, which is caused by vertical wind shear and blade rotation. For downwind turbines in the wake of the yawed turbine, differences in the flapwise blade fatigue are due to the different wake deficit and turbulence distributions in the wake of the positively and negatively yawed turbine.

- Study 4: we use a two-way coupled LES and aeroelastic solver to study the wake meandering within an array of eight NREL 5 MW turbines subjected to DYC and evaluate the effects on power and fatigue of the turbine array. Based on spectral and DMD analyses of flow fields, we find that, in the static non-yawed case, a dominant meandering frequency emerges in the wakes of the turbines, particularly near the rear of the array. In the DYC cases, the wake meandering is amplified when the yaw frequency of the first turbine is the same as the natural wake-meandering frequency of the zero-yaw case. The resonated wake meandering accelerates the wake recovery in the turbine array and helps the turbine array achieve the optimal total power output. On the other hand, the flapwise blade fatigue and nacelle yaw fatigue of the yawed turbine overall increase with the yaw frequency, which highlights the necessity of jointly considering the power gain and the increase of fatigue when DYC is applied.

## 6.2 Future perspectives

There are several potential extensions to the studies presented in this thesis:

- In this thesis, we have shown that the ADM-BE in LES can produce satisfactory force distribution and power production. A potential direction for future studies is to explore the application of the ADM-BE in the two-way coupled LES/aeroelastic simulation, potentially as a substitution of the ALM, which requires finer spatial and temporal resolution than the ADM.
- The findings in this thesis also shed light on further improvements in reduced-order wake models for yawed turbines. We have found that, with the presence of vertical wind shear in the inflow, the wake statistics of a positively and negatively yawed turbine are not symmetrical to each other, even if the magnitude of the yaw angle is the same. An interesting direction for future studies can be the incorporation of asymmetry of positive and negative yaw in reduced-order wake models, particularly for turbulence intensity, which demonstrates strong asymmetry.

- The LES-aeroelastic analysis of blades in this thesis uses a simplified 1D elastic actuator line model (EALM). In future investigations of AYC, we can carry out a coupled simulation of LES and complete finite-element analysis for the turbine. By doing so, we can further identify the stress hot spots in different turbine components and obtain a more comprehensive understanding of the potential impact of applying AYC on turbine fatigue loads. Such an analysis can help us develop a cost model quantifying the influences of AYC on the service lives of different turbine components.
- In Study 4, we have identified the resonance behaviour of the wake meandering in a long wind turbine array. An interesting extension to this data-driven study can be a theoretical analysis of the stability of the wake meandering and the optimal control using DYC. Compared to previous theoretical studies of the wake of a single turbine (Iungo et al., 2013; Z. Li et al., 2022) using linear stability theory, the main challenge for extending those analyses is the non-linearity of the wake meandering in the turbine array, as the wake deficits do not recover to the level such that the linearisation of the governing equation can be reasonably adopted. Therefore, the theoretical models proposed by previous studies, e.g., the complex Ginzburg–Landau (CGL) equations (Z. Li et al., 2022) or the linearised Navier-Stokes equations (Iungo et al., 2013), may not be suitable to study this phenomenon, and we need to explore new tools. One potential candidate is the SINDy (Sparse Identification of Nonlinear Dynamics) analysis, a data-driven technique to discover the underlying equations that govern a dynamic system (Brunton et al., 2016a). Such an analysis can be further extended with control (Brunton et al., 2016b), which is suitable for theoretically modelling the optimal DYC in a wind farm.





# Bibliography

- Abkar, M., & Porté-Agel, F. (2015). Influence of atmospheric stability on wind-turbine wakes: a large-eddy simulation study. *Phys. Fluids*, 27(3), 035104. <https://doi.org/10.1063/1.4913695>
- Allaerts, D., & Meyers, J. (2015). Large eddy simulation of a large wind-turbine array in a conventionally neutral atmospheric boundary layer. *Physics of Fluids*, 27(6), 065108. <https://doi.org/10.1063/1.4922339>
- Anderson, J. (2011). *Fundamentals of aerodynamics*. McGraw Hill.
- Archer, C. L., Vasel-Be-Hagh, A., Yan, C., Wu, S., Pan, Y., Brodie, J. F., & Maguire, A. E. (2018). Review and evaluation of wake loss models for wind energy applications. *Appl. Energ.*, 226, 1187. <https://doi.org/10.1016/j.apenergy.2018.05.085>
- Archer, C. L., & Vasel-Be-Hagh, A. (2019). Wake steering via yaw control in multi-turbine wind farms: recommendations based on large-eddy simulation. *Sustain. Energy Tech. and Assess.*, 33, 34. <https://doi.org/10.1016/j.seta.2019.03.002>
- Atkinson, G., & Wilson, D. (1986). Unsteadiness and structure in the wake of a wind turbine. *Wind Engineering*, 150–162.
- Baker, R. W., & Walker, S. N. (1984). Wake measurements behind a large horizontal axis wind turbine generator. *Solar Energy*, 33(1), 5–12.
- Barthelmie, R. J., & Jensen, L. E. (2010). Evaluation of wind farm efficiency and wind turbine wakes at the nysted offshore wind farm. wind energy. *Wind Energy*, 13(6), 573. <https://doi.org/10.1002/we.408>
- Bartl, J., & Sætran, L. (2016). Experimental testing of axial induction based control strategies for wake control and wind farm optimization. *Journal of Physics: Conference Series*, 753(3), 032035. <https://doi.org/10.1088/1742-6596/753/3/032035>
- Bastankhah, M., & Porté-Agel, F. (2014). A new analytical model for wind-turbine wakes. *Renew. Energ.*, 70, 116–123. <https://doi.org/10.1016/j.renene.2014.01.002>
- Bastankhah, M., & Porté-Agel, F. (2016). Experimental and theoretical study of wind-turbine wakes in yawed conditions. *J. Fluid Mech.*, 806, 506–541. <https://doi.org/10.1017/jfm.2016.595>
- Bastankhah, M., & Porté-Agel, F. (2017). A new miniature wind turbine for wind tunnel experiments. part i: design and performance. *Energies*, 10(7), 908. <https://doi.org/10.3390/en10070908>

## Bibliography

---

- Bastankhah, M., & Porté-Agel, F. (2019). Wind farm power optimization via yaw angle control: a wind tunnel study. *J. of Renew. Sustain. Ener.*, 11(2), 023301. <https://doi.org/10.1063/1.5077038>
- Bay, C. J., King, J., Fleming, P., Mudafort, R., & Martinez-Tossas, L. A. (2019). Unlocking the full potential of wake steering: implementation and assessment of a controls-oriented model. *Wind Energ. Sci. Discussions*, 1–20. <https://doi.org/10.5194/wes-2019-19>
- Boersma, S., Doekemeijer, B., Siniscalchi-Minna, S., & van Wingerden, J. (2018). A constrained wind farm controller providing secondary frequency regulation: an LES study. *Renew. Energ.*
- Boersma, S., Doekemeijer, B., Siniscalchi-Minna, S., & van Wingerden, J. (2019). A constrained wind farm controller providing secondary frequency regulation: an les study. *Renew. Energ.*, 134, 639–652. <https://doi.org/10.1016/j.renene.2018.11.031>
- Braunbehrens, R., & Segalini, A. (2019). A statistical model for wake meandering behind wind turbines. *J. Wind Eng. Ind. Aerodyn.*, 193, 103954. <https://doi.org/10.1016/j.jweia.2019.103954>
- Brugger, P., Markfort, C., & Porté-Agel, F. (2022). Field measurements of wake meandering at a utility-scale wind turbine with nacelle-mounted doppler lidars. *Wind Energ. Sci.*, 7(1), 185–199. <https://doi.org/10.5194/wes-7-185-2022>
- Brunton, S. L., Proctor, J. L., & Kutz, J. N. (2016a). Discovering governing equations from data by sparse identification of nonlinear dynamical systems. *Proc. Natl. Acad. Sci. U.S.A.*, 113(15), 3932–3937.
- Brunton, S. L., Proctor, J. L., & Kutz, J. N. (2016b). Sparse identification of nonlinear dynamics with control (sindyc). *IFAC-PapersOnLine*, 49(18), 710–715. <https://doi.org/10.1016/j.ifacol.2016.10.249>
- Burton, T., Jenkins, N., Sharpe, D., & Bossanyi, E. (2011). *Wind energy handbook*. John Wiley & Sons.
- Campagnolo, F., Castellani, F., Natili, F., Astolfi, D., & Mühle, F. (2022). Wind tunnel testing of yaw by individual pitch control applied to wake steering. *Front. Energy Res.*, 10. <https://doi.org/10.3389/fenrg.2022.883889>
- Chow, F. K., Street, R. L., Xue, M., & Ferziger, J. H. (2005). Explicit filtering and reconstruction turbulence modeling for large-eddy simulation of neutral boundary layer flow. *J. Atmos. Sci.*, 62(7), 2058–2077. <https://doi.org/10.1175/JAS3456.1>
- Chowdhury, S., Zhang, J., Messac, A., & Castillo, L. (2012). Unrestricted wind farm layout optimization (uwflo): investigating key factors influencing the maximum power generation. *Renew. Energ.*, 38(1), 16–30. <https://doi.org/10.1016/j.renene.2011.06.033>
- Churchfield, M. J., Lee, S., Michalakes, J., & Moriarty, P. J. (2012). A numerical study of the effects of atmospheric and wake turbulence on wind turbine dynamics. *J. Turbul.*, (13), N14. <https://doi.org/10.1080/14685248.2012.668191>
- Coleman, R. P., Feingold, A. M., & Stempin, C. W. (1945). *Evaluation of the induced-velocity field of an idealized helicopter rotor* (tech. rep.). National Aeronautics and Space Administration Hampton Va Langley Research Center.

- Damiani, R., Dana, S., Annoni, J., Fleming, P., Roadman, J., van Dam, J., & Dykes, K. (2018). Assessment of wind turbine component loads under yaw-offset conditions. *Wind Energ. Sci.*, 3(1), 173–189. <https://doi.org/10.5194/wes-3-173-2018>
- Draper, M., & Usera, G. (2015). Evaluation of the actuator line model with coarse resolutions. *Journal of Physics: Conference Series*, 625(1), 012021.
- Duan, G., & Porté-Agel, F. (2023). A wind tunnel study on cyclic yaw control: power performance and wake characteristics. [Manuscript submitted for publication].
- Dykes, K. (2013). *Wind power for the world: the rise of modern wind energy*. Pan Stanford Publishing Pte. Ltd.
- Espana, G., Aubrun, S., Loyer, S., & Devinant, P. (2012). Wind tunnel study of the wake meandering downstream of a modelled wind turbine as an effect of large scale turbulent eddies. *J. Wind Eng. Ind. Aerodyn.*, 101, 24–33. <https://doi.org/10.1016/j.jweia.2011.10.011>
- Fang, J., & Porté-Agel, F. (2015). Large-eddy simulation of very-large-scale motions in the neutrally stratified atmospheric boundary layer. *Bound.-Lay. Meteo.*, 155(3), 397. <https://doi.org/10.1007/s10546-015-0006-z>
- Fleming, P., Annoni, J., Churchfield, M., Martinez-Tossas, L. A., Gruchalla, K., Lawson, M., & Moriarty, P. (2018). A simulation study demonstrating the importance of large-scale trailing vortices in wake steering. *Wind Energ. Sci.*, 3(1), 243–255. <https://doi.org/10.5194/wes-3-243-2018>
- Fleming, P., Gebraad, P., Lee, S., van Wingerden, J.-W., Johnson, K., Churchfield, M., Michalakes, J., Spalart, P., & Moriarty, P. (2014). Evaluating techniques for redirecting turbine wakes using SOWFA. *Renew. Energ.*, 70, 211–218. <https://doi.org/10.1016/j.renene.2014.02.015>
- Fleming, P., Gebraad, P. M., Lee, S., van Wingerden, J.-W., Johnson, K., Churchfield, M., Michalakes, J., Spalart, P., & Moriarty, P. (2015). Simulation comparison of wake mitigation control strategies for a two-turbine case. *Wind Energy*, 18(12), 2135–2143. <https://doi.org/10.1002/we.1810>
- Fleming, P., Ning, A., Gebraad, P. M., & Dykes, K. (2016). Wind plant system engineering through optimization of layout and yaw control. *Wind Energy*, 19(2), 329. <https://doi.org/10.1002/we.1836>
- Frederik, J. A., Doekemeijer, B. M., Mulders, S. P., & van Wingerden, J.-W. (2020). The helix approach: Using dynamic individual pitch control to enhance wake mixing in wind farms. *Wind Energy*, 23(8), 1739–1751. <https://doi.org/10.1002/we.2513>
- Frederik, J. A., Weber, R., Cacciola, S., Campagnolo, F., Croce, A., Bottasso, C., & van Wingerden, J.-W. (2020). Periodic dynamic induction control of wind farms: proving the potential in simulations and wind tunnel experiments. *Wind Energ. Sci.*, 5(1), 245–257. <https://doi.org/10.5194/wes-5-245-2020>
- Frederik, J. A., & van Wingerden, J.-W. (2022). On the load impact of dynamic wind farm wake mixing strategies. *Renew. Energ.*, 194, 582–595. <https://doi.org/10.1016/j.renene.2022.05.110>
- Freebury, G., & Musial, W. (2000). Determining equivalent damage loading for full-scale wind turbine blade fatigue tests. *2000 ASME wind energy symposium*, 50.

## Bibliography

---

- Gebraad, P., Thomas, J. J., Ning, A., Fleming, P., & Dykes, K. (2017). Maximization of the annual energy production of wind power plants by optimization of layout and yaw-based wake control. *Wind Energy*, 20(1), 97–107. <https://doi.org/10.1002/we.1993>
- Gipe, P., & Möllerström, E. (2022). An overview of the history of wind turbine development: part i—the early wind turbines until the 1960s. *Wind Engineering*, 46(6), 1973–2004. <https://doi.org/10.1177/0309524X221117825>
- Glasson, J., Durning, B., Welch, K., & Olorundami, T. (2022). The local socio-economic impacts of offshore wind farms. *Environ. Impact Assess. Rev.*, 95, 106783. <https://doi.org/10.1016/j.eiar.2022.106783>
- Glauert, H. (1927). The theory of the autogyro. *The Aeronautical Journal*, 31(198), 483–508.
- Goit, J. P., & Meyers, J. (2015). Optimal control of energy extraction in wind-farm boundary layers. *J. Fluid Mech.*, 768, 5–50. <https://doi.org/10.1017/jfm.2015.70>
- Grant, I., & Parkin, P. (2000). A dpiv study of the trailing vortex elements from the blades of a horizontal axis wind turbine in yaw. *Exp. Fluids*, 28(4), 368. <https://doi.org/10.1007/s003480050396>
- Grant, I., Parkin, P., & Wang, X. (1997). Optical vortex tracking studies of a horizontal axis wind turbine in yaw using laser-sheet, flow visualisation. *Exp. Fluids*, 23(6), 513. <https://doi.org/10.1007/s003480050142>
- Gupta, V., & Wan, M. (2019). Low-order modelling of wake meandering behind turbines. *J. Fluid Mech.*, 877, 534–560. <https://doi.org/10.1017/jfm.2019.619>
- GWEC. (2022). Global wind report 2022.
- Hansen, M. O. (2015). *Aerodynamics of wind turbines*. Routledge.
- Houck, D., & Cowen, E. (2019). Can you accelerate wind turbine wake decay with unsteady operation? *AIAA Scitech 2019 Forum*. <https://doi.org/10.2514/6.2019-2084>
- Howland, M. F., Bossuyt, J., Martínez-Tossas, L. A., Meyers, J., & Meneveau, C. (2016). Wake structure in actuator disk models of wind turbines in yaw under uniform inflow conditions. *J. Renew. Sustain Ener.*, 8(4), 043301. <https://doi.org/10.1063/1.4955091>
- Howland, M. F., Lele, S. K., & Dabiri, J. O. (2019). Wind farm power optimization through wake steering. *Proc. Natl. Acad. Sci. U.S.A.*, 116(29), 14495–14500.
- IEC. (2019). *Iec 61400-1:2019, wind energy generation systems - part 1: design requirements* (3.). International Electrotechnical Commission.
- Iungo, G. V., Viola, F., Camarri, S., Porté-Agel, F., & Gallaire, F. (2013). Linear stability analysis of wind turbine wakes performed on wind tunnel measurements. *J. Fluid Mech.*, 737, 499–526. <https://doi.org/10.1017/jfm.2013.569>
- Jensen, N. (1983). *A note on wind generator interaction*. Risø National Laboratory.
- Jiménez, A., Crespo, A., Migoya, E., & Garcia, J. (2007). Advances in large-eddy simulation of a wind turbine wake. *Journal of Physics: Conference Series*, 75(1), 012041. <https://doi.org/10.1088/1742-6596/75/1/012041>
- Jiménez, A., Crespo, A., & Migoya, E. (2010). Application of a les technique to characterize the wake deflection of a wind turbine in yaw. *Wind Energy*, 13(6), 559–572. <https://doi.org/10.1002/we.380>

- Jonkman, J., Butterfield, S., Musial, W., & Scott, G. (2009). *Definition of a 5-mw reference wind turbine for offshore system development* (tech. rep.). National Renewable Energy Lab.(NREL), Golden, CO (United States). <https://doi.org/10.2172/947422>
- Kaldellis, J. K., & Zafirakis, D. (2011). The wind energy (r) evolution: a short review of a long history. *Renew. Energ.*, 36(7), 1887–1901. <https://doi.org/https://doi.org/10.1016/j.renene.2011.01.002>
- Kanev, S., Savenije, F., & Engels, W. (2018). Active wake control: an approach to optimize the lifetime operation of wind farms. *Wind Energy*, 21(7), 488–501.
- Kang, S., Yang, X., & Sotiropoulos, F. (2014). On the onset of wake meandering for an axial flow turbine in a turbulent open channel flow. *J. Fluid Mech.*, 744, 376–403. <https://doi.org/10.1017/jfm.2014.82>
- Kimura, K., Tanabe, Y., Matsuo, Y., & Iida, M. (2019). Forced wake meandering for rapid recovery of velocity deficits in a wind turbine wake. In *AIAA Scitech 2019 Forum* (p. 2083). American Institute of Aeronautics; Astronautics. <https://doi.org/10.2514/6.2019-2083>
- King, J., Fleming, P., King, R., Martinez-Tossas, L. A., Bay, C. J., Mudafort, R., & Simley, E. (2021). Control-oriented model for secondary effects of wake steering. *Wind Energ. Sci.*, 6(3), 701–714. <https://doi.org/10.5194/wes-6-701-2021>
- Kirchner-Bossi, N., & Porté-Agel, F. (2018). Realistic wind farm layout optimization through genetic algorithms using a gaussian wake model. *Energies*, 11(12). <https://doi.org/10.3390/en1123268>
- Kragh, K. A., & Hansen, M. H. (2014). Load alleviation of wind turbines by yaw misalignment. *Wind Energy*, 17(7), 971–982. <https://doi.org/doi.org/10.1002/we.1612>
- Kusiak, A., & Song, Z. (2010). Design of wind farm layout for maximum wind energy capture. *Renew. Energ.*, 35(3), 685–694. <https://doi.org/10.1016/j.renene.2009.08.019>
- Larsen, G. C., Madsen, H. A., Thomsen, K., & Larsen, T. J. (2008). Wake meandering: a pragmatic approach. *Wind Energy*, 11(4), 377–395. <https://doi.org/10.1002/we.267>
- Lavelly, A. W., Vijayakumar, G., Craven, B., Jayaraman, B., Paterson, E. G., Nandi, T. N., & Brasseur, J. (2014). Towards a blade-resolved hybrid URANS-LES of the NREL 5-MW wind turbine rotor within large eddy simulation of the atmospheric boundary layer. *32nd ASME Wind Energy Symposium*, 0869. <https://doi.org/10.2514/6.2014-0869>
- Li, B., He, J., Ge, M., Ma, H., Du, B., Yang, H., & Liu, Y. (2022). Study of three wake control strategies for power maximization of offshore wind farms with different layouts. *Energy Convers. Manag.*, 268, 116059. <https://doi.org/10.1016/j.enconman.2022.116059>
- Li, Z., Dong, G., & Yang, X. (2022). Onset of wake meandering for a floating offshore wind turbine under side-to-side motion. *J. Fluid Mech.*, 934.
- Lin, M., & Porté-Agel, F. (2022). Large-eddy simulation of a wind-turbine array subjected to active yaw control. *Wind Energ. Sci.*, 7(6), 2215–2230. <https://doi.org/10.5194/wes-7-2215-2022>
- Lin, M., & Porté-Agel, F. (2019). Large-eddy simulation of yawed wind-turbine wakes: comparisons with wind tunnel measurements and analytical wake models. *Energies*, 12(23), 4574. <https://doi.org/10.3390/en12234574>

## Bibliography

---

- Lin, M., & Porté-Agel, F. (2020). Power maximization and fatigue-load mitigation in a wind-turbine array by active yaw control: an LES study. *Journal of Physics: Conference Series*, 1618(4), 042036. <https://doi.org/10.1088/1742-6596/1618/4/042036>
- Lin, M., & Porté-Agel, F. (2023). Power production and blade fatigue of a wind turbine array subjected to active yaw control. *Energies*, 16(6), 2542. <https://doi.org/10.3390/en16062542>
- Lu, H., & Porté-Agel, F. (2010). A modulated gradient model for large-eddy simulation: application to a neutral atmospheric boundary layer. *Phys. Fluids*, 22(1), 015109. <https://doi.org/10.1063/1.3291073>
- Lu, H., & Porté-Agel, F. (2014). On the development of a dynamic non-linear closure for large-eddy simulation of the atmospheric boundary layer. *Bound.-Lay. Meteorol.*, 151(3), 429–451. <https://doi.org/10.1007/s10546-013-9906-y>
- Ma, H., Ge, M., Wu, G., Du, B., & Liu, Y. (2021). Formulas of the optimized yaw angles for cooperative control of wind farms with aligned turbines to maximize the power production. *Appl. Energy*, 303, 117691. <https://doi.org/https://doi.org/10.1016/j.apenergy.2021.117691>
- Martinez, L., Leonardi, S., Churchfield, M., & Moriarty, P. (2012). A comparison of actuator disk and actuator line wind turbine models and best practices for their use. *50th AIAA Aerospace Sciences Meeting including the New Horizons Forum and Aerospace Exposition*, 900. <https://doi.org/10.2514/6.2012-900>
- Martínez-Tossas, L. A., Annoni, J., Fleming, P. A., & Churchfield, M. J. (2019). The aerodynamics of the curled wake: a simplified model in view of flow control. *Wind Energ. Sci.*, 4(1), 127–138. <https://doi.org/10.5194/wes-4-127-2019>
- Martínez-Tossas, L. A., Churchfield, M. J., & Leonardi, S. (2015). Large eddy simulations of the flow past wind turbines: actuator line and disk modeling. *Wind Energy*, 18(6), 1047–1060. <https://doi.org/https://doi.org/10.1002/we.1747>
- Martinez-Tossas, L. A., Churchfield, M. J., & Meneveau, C. (2017). Optimal smoothing length scale for actuator line models of wind turbine blades based on gaussian body force distribution. *Wind Energy*, 20(6), 1083. <https://doi.org/10.1002/we.2081>
- Medici, D., & Alfredsson, P. (2006). Measurements on a wind turbine wake: 3D effects and bluff body vortex shedding. *Wind Energy*, 9(3), 219–236. <https://doi.org/https://doi.org/10.1002/we.156>
- Meng, H., Lien, F.-S., & Li, L. (2018). Elastic actuator line modelling for wake-induced fatigue analysis of horizontal axis wind turbine blade. *Renew. Energ.*, 116, 423–437. <https://doi.org/10.1016/j.renene.2017.08.074>
- Meyers, J., Bottasso, C., Dykes, K., Fleming, P., Gebraad, P., Giebel, G., Göçmen, T., & Van Wingerden, J.-W. (2022). Wind farm flow control: prospects and challenges. *Wind Energ. Sci.*, 7(6), 2271–2306.
- Mikkelsen, R. (2003). *Actuator disc methods applied to wind turbines* (Doctoral dissertation). Technical University of Denmark.

- Moeng, C.-H. (1984). A large-eddy-simulation model for the study of planetary boundary-layer turbulence. *J. Atmos. Sci.*, 41(13), 2052–2062. [https://doi.org/10.1175/1520-0469\(1984\)041<2052:ALESMP>2.0.CO;2](https://doi.org/10.1175/1520-0469(1984)041<2052:ALESMP>2.0.CO;2)
- Moin, P., & Kim, J. (1982). Numerical investigation of turbulent channel flow. *J. Fluid Mech.*, 118, 341–377. <https://doi.org/10.1017/S0022112082001116>
- Muller, Y.-A., Aubrun, S., & Masson, C. (2015). Determination of real-time predictors of the wind turbine wake meandering. *Exp. Fluids*, 56(3), 1–11. <https://doi.org/10.1007/s00348-015-1923-9>
- Munters, W., & Meyers, J. (2018a). Dynamic strategies for yaw and induction control of wind farms based on large-eddy simulation and optimization. *Energies*, 11(1), 177. <https://doi.org/10.3390/en11010177>
- Munters, W., Meneveau, C., & Meyers, J. (2016). Shifted periodic boundary conditions for simulations of wall-bounded turbulent flows. *Phys. Fluids*, 28(2), 025112. <https://doi.org/10.1063/1.4941912>
- Munters, W., & Meyers, J. (2017). An optimal control framework for dynamic induction control of wind farms and their interaction with the atmospheric boundary layer. *Phil. Trans. R. Soc. A*, 375(2091), 20160100.
- Munters, W., & Meyers, J. (2018b). Towards practical dynamic induction control of wind farms: analysis of optimally controlled wind-farm boundary layers and sinusoidal induction control of first-row turbines. *Wind Energ. Sci.*, 3(1), 409–425. <https://doi.org/10.5194/wes-3-409-2018>
- Munters, W., & Meyers, J. (2018c). Dynamic Strategies for Yaw and Induction Control of Wind Farms Based on Large-Eddy Simulation and Optimization. *Energies*, 11(1), 177. <https://doi.org/10.3390/en11010177>
- Øys, S. (1992). Induced velocity for rotors in yaw. *Proceedings of the 6th IEA Symposium on the Aerodynamics of Wind Turbines*.
- Parkin, P., Holm, R., & Medici, D. (2001). The application of piv to the wake of a wind turbine in yaw. *Particle Image Velocimetry; Gottingen; 17 September 2001 through 19 September 2001*, 155–162.
- Porté-Agel, F., Meneveau, C., & Parlange, M. B. (2000). A scale-dependent dynamic model for large-eddy simulation: application to a neutral atmospheric boundary layer. *J. Fluid Mech.*, 415, 261–284. <https://doi.org/10.1017/S0022112000008776>
- Porté-Agel, F., Wu, Y. T., & Chen, C. H. (2013). A numerical study of the effects of wind direction on turbine wakes and power losses in a large wind farm. *Energies*, 6(10), 5297. <https://doi.org/10.3390/en6105297>
- Porté-Agel, F., Bastankhah, M., & Shamsoddin, S. (2019). Wind-turbine and wind-farm flows: a review. *Bound.-Layer Meteorol.*, 1–59. <https://doi.org/10.1007/s10546-019-00473-0>
- Porté-Agel, F., Bastankhah, M., & Shamsoddin, S. (2020). Wind-turbine and wind-farm flows: a review. *Bound.-Lay. Meteorol.*, 174(1), 1–59. <https://doi.org/10.1007/s10546-019-00473-0>

- Porté-Agel, F., Wu, Y.-T., Lu, H., & Conzemius, R. J. (2011a). Large-eddy simulation of atmospheric boundary layer flow through wind turbines and wind farms. *J. Wind Eng. Ind. Aerod.*, 99(4), 154–168. <https://doi.org/10.1016/j.jweia.2011.01.011>
- Porté-Agel, F., Wu, Y.-T., Lu, H., & Conzemius, R. J. (2011b). Large-eddy simulation of atmospheric boundary layer flow through wind turbines and wind farms. *J. Wind Eng. Ind. Aerod.*, 99(4), 154–168. <https://doi.org/10.1016/j.jweia.2011.01.011>
- Qian, G.-W., & Ishihara, T. (2021). Wind farm power maximization through wake steering with a new multiple wake model for prediction of turbulence intensity. *Energy*, 220, 119680. <https://doi.org/10.1016/j.energy.2020.119680>
- Qian, G.-W., & Ishihara, T. (2018). A new analytical wake model for yawed wind turbines. *Energies*, 11(3), 665. <https://doi.org/10.3390/en11030665>
- Revaz, T., Lin, M., & Porté-Agel, F. (2020). Numerical framework for aerodynamic characterization of wind turbine airfoils: application to miniature wind turbine wire-01. *Energies*, 13(21), 5612. <https://doi.org/10.3390/en13215612>
- Reyes, H. M., Kanev, S., Doekemeijer, B., & van Wingerden, J.-W. (2019). Validation of a look-up-table approach to modeling turbine fatigue loads in wind farms under active wake control. *Wind Energ. Sci.*, 4(4), 549–561. <https://doi.org/10.5194/wes-4-549-2019>
- Şahin, A. D. (2004). Progress and recent trends in wind energy. *Prog. Energy Combust. Sci.*, 30(5), 501–543. <https://doi.org/10.1016/j.pecs.2004.04.001>
- Samorani, M. (2013). The wind farm layout optimization problem. *Handbook of wind power systems*, 21–38.
- Schmid, P. J. (2010). Dynamic mode decomposition of numerical and experimental data. *J. Fluid Mech.*, 656, 5–28.
- Shapiro, C. R., Gayme, D. F., & Meneveau, C. (2018). Modelling yawed wind turbine wakes: a lifting line approach. *J. Fluid Mech.*, 841, R1. <https://doi.org/10.1017/jfm.2018.75>
- Shen, W., Chen, X., Qiu, J., Hayward, J. A., Sayeef, S., Osman, P., Meng, K., & Dong, Z. Y. (2020). A comprehensive review of variable renewable energy levelized cost of electricity. *Renewable Sustainable Energy Rev.*, 133, 110301. <https://doi.org/10.1016/j.rser.2020.110301>
- Shepherd, D. G. (1990). *Historical development of the windmill* (tech. rep.). Cornell Univ., Ithaca, NY (USA). Dept. of Mechanical and Aerospace Engineering.
- Smith, R. A., Moon, W. T., & Kao, T. (1972). Experiments on flow about a yawed circular cylinder. *J. Basic Eng.*, 94(4), 771–776. <https://doi.org/10.1115/1.3425551>
- Sørensen, J. N., Mikkelsen, R. F., Henningson, D. S., Ivanell, S., Sarmast, S., & Andersen, S. J. (2015). Simulation of wind turbine wakes using the actuator line technique. *Phil. Trans. R. Soc. A*, 373(2035), 20140071. <https://doi.org/10.1098/rsta.2014.0071>
- Sørensen, J. N., Shen, W. Z., & Munduate, X. (1998). Analysis of wake states by a full-field actuator disc model. *Wind Energy*, 1(2), 73–88. [https://doi.org/10.1002/\(SICI\)1099-1824\(199812\)1:2<73::AID-WE12>3.0.CO;2-L](https://doi.org/10.1002/(SICI)1099-1824(199812)1:2<73::AID-WE12>3.0.CO;2-L)
- Sørensen, J. N., & Shen, W. Z. (2002). Numerical modeling of wind turbine wakes. *J. Fluids Eng.*, 124(2), 393–399. <https://doi.org/10.1115/1.1471361>



- Stevens, R. J., Martinez-Tossas, L. A., & Meneveau, C. (2018). Comparison of wind farm large eddy simulations using actuator disk and actuator line models with wind tunnel experiments. *Renew. Energ.*, 116, 470. <https://doi.org/10.1016/j.renene.2017.08.072>
- Stevens, R. J., & Meneveau, C. (2017). Flow structure and turbulence in wind farms. *Annu. Rev. Fluid Mech.*, 49. <https://doi.org/10.1146/annurev-fluid-010816-060206>
- Stoll, R., & Porté-Agel, F. (2006). Dynamic subgrid-scale models for momentum and scalar fluxes in large-eddy simulations of neutrally stratified atmospheric boundary layers over heterogeneous terrain. *Water Resour. Res.*, 42(1). <https://doi.org/10.1029/2005WR003989>
- Taylor, G., Milborrow, D., McIntosh, D., & Swift-Hook, D. (1985). Wake measurements on the nibe windmills. *Proceedings of Seventh BWEA Wind Energy Conference, Oxford*, 67–73.
- Van Dijk, M. T., Van Wingerden, J., Ashuri, T., & Li, Y. (2017). Wind farm multi-objective wake redirection for optimizing power production and loads. *Energy*, 121, 561–569. <https://doi.org/10.1016/j.energy.2017.01.051>
- Wang, J., Foley, S., Nanos, E. M., Yu, T., Campagnolo, F., Bottasso, C. L., Zanotti, A., & Croce, A. (2017). Numerical and experimental study of wake redirection techniques in a boundary layer wind tunnel. *Journal of Physics: Conference Series*, 854(1), 012048. <https://doi.org/10.1088/1742-6596/854/1/012048>
- Willmarth, W. W., & Wei, T. (2021). Static pressure distribution on long cylinders as a function of the yaw angle and reynolds number. *Fluids*, 6(5). <https://doi.org/10.3390/fluids6050169>
- Wu, Y.-T., & Porté-Agel, F. (2011). Large-eddy simulation of wind-turbine wakes: evaluation of turbine parametrisations. *Bound.-Layer Meteorol.*, 138(3), 345. <https://doi.org/10.1007/s10546-010-9569-x>
- Wu, Y.-T., & Porté-Agel, F. (2012). Atmospheric turbulence effects on wind-turbine wakes: an LES study. *Energies*, 5(12), 5340–5362. <https://doi.org/10.3390/en5125340>
- Wu, Y.-T., & Porté-Agel, F. (2013). Simulation of turbulent flow inside and above wind farms: model validation and layout effects. *Bound.-Layer Meteorol.*, 146(2), 181–205. <https://doi.org/10.1007/s10546-012-9757-y>
- Wu, Y.-T., & Porté-Agel, F. (2015). Modeling turbine wakes and power losses within a wind farm using les: an application to the horns rev offshore wind farm. *Renew. Energ.*, 75, 945–955. <https://doi.org/10.1016/j.renene.2014.06.019>
- Yang, X., & Sotiropoulos, F. (2019). Wake characteristics of a utility-scale wind turbine under coherent inflow structures and different operating conditions. *Phys. Rev. Fluids*, 4(2), 024604. <https://doi.org/PhysRevFluids.4.024604>
- Yuan, J. (2016). Wind energy in china: estimating the potential. *Nature Energy*, 1(7), 1–2. <https://doi.org/10.1038/nenergy.2016.95>
- Zalkind, D. S., & Pao, L. Y. (2016). The fatigue loading effects of yaw control for wind plants. *2016 American Control Conference (ACC)*, 537–542.
- Zhang, B. (2009). Ancient chinese windmills. *International Symposium on History of Machines and Mechanisms: Proceedings of HMM 2008*, 203–214. [https://doi.org/10.1007/978-1-4020-9485-9\\_15](https://doi.org/10.1007/978-1-4020-9485-9_15)

## Bibliography

---

- Zong, H., & Porté-Agel, F. (2020a). A momentum-conserving wake superposition method for wind farm power prediction. *J. Fluid Mech.*, 889, A8. <https://doi.org/10.1017/jfm.2020.77>
- Zong, H., & Porté-Agel, F. (2020b). A point vortex transportation model for yawed wind turbine wakes. *J. Fluid Mech.*, 890, A8. <https://doi.org/10.1017/jfm.2020.123>
- Zong, H., & Porté-Agel, F. (2021). Experimental investigation and analytical modelling of active yaw control for wind farm power optimization. *Renew. Energ.*, 170, 1228–1244. <https://doi.org/10.1016/j.renene.2021.02.059>

## SKILLS

Fortran

C++

Linux Bash

Python

CUDA

## LANGUAGES

Chinese

*Native or Bilingual Proficiency*

English

*Full Professional Proficiency*

French

*Elementary Proficiency*

## EDUCATION

### PhD in Mechanics

École polytechnique fédérale de Lausanne

09/2017 - 06/2023

Lausanne, Switzerland

*Thesis*

- Wind turbines wakes in active yaw control: numerical and theoretical studies

### MSc in Wind Energy

Technical University of Denmark

09/2014 - 06/2016

Lyngby, Denmark

*Thesis*

- Implementation and validation of a steady-state Euler solver in C++

### BEng. in Naval Architecture and Ocean Engineering

Harbin Engineering University

09/2010 - 06/2014

Harbin, China

*Thesis*

- Design and dynamic analysis of the floating platform for a hybrid ocean renewable power generation system

## PUBLICATIONS

*Journal paper*

**Wake meandering of wind turbines under dynamic yaw control and impacts on power and fatigue.**

*Author(s)*

Lin, M, and F. Porté-Agel.

2023

Renewable Energy (under submission)

*Journal paper*

**Power production and blade fatigue of a wind turbine array subjected to active yaw control**

*Author(s)*

Lin, M, and Porté-Agel, F.

2023

Energies, 16 (6), p.2542.

*Journal paper*

**Large-eddy simulation of a wind-turbine array subjected to active yaw control.**

*Author(s)*

Lin, M, and Porté-Agel, F.

2022

Wind Energy Science, 7 (6), pp.2215-2230.

*Conference papers*

**Power maximization and fatigue-load mitigation in a wind-turbine array by active yaw control: an LES study**

*Author(s)*

Lin, M, and Porté-Agel, F.

2020

Journal of Physics: Conference Series (Vol. 1618, No. 4, p. 042036). IOP Publishing.

*Journal paper*

**Numerical framework for aerodynamic characterization of wind turbine airfoils: Application to miniature wind turbine WiRE-01**

*Author(s)*

Revaz, T., Lin, M. and Porté-Agel, F.

2020

Energies, 13(21), p.5612.

*Journal paper*

**Large-eddy simulation of yawed wind-turbine wakes: comparisons with wind tunnel measurements and analytical wake models**

*Author(s)*

Lin, M, and Porté-Agel, F.

2019

Energies, 12(23), p.4574.